Microstructure-Enabled Plasticity in Nano-to-Microscale Materials

Thesis by
Haolu (Jane) Zhang

In Partial Fulfillment of the Requirements for the
Degree of
Doctor of Philosophy

CALIFORNIA INSTITUTE OF TECHNOLOGY
Pasadena, California

2021
Defended December 10th, 2020

Haolu (Jane) Zhang
ORCID: 0000-0002-2871-5169

ACKNOWLEDGEMENTS

My journey at Caltech has been and will always be one of the most treasured memories of my life. I genuinly enjoyed the academic atmosphere, and it was my honor to learn from some of the kindest and most talented minds on this planet, who helped me grow from the student with little confidence to the proud researcher that I am today. While I acknowlege some of those people here, the list is really endless.

To Dr. Ellen Arruda and Dr. Michael Thouless, you jump-started my enthusiasm for research, and I would not be where I am today without you. Dr. Julia R. Greer, you are both an amazing advisor and an inspiring person. I have learned so much from you, and I truly appreciate the patience and the opportunities that you have provided. You have taught me to be confident, courageous, and strong-minded, and I cannot ever thank you enough for that. To Dr. Richard D. James and Dr. Eckhard Quandt, you have been great collaborators and encouraging mentors. To Dr. Xiaoyue Ni, your mentorship made my transition to PhD less nerve-wrecking.

I would like to give thanks to my amazing collaborators. Justin and Hanlin, you have made my first project, first presentation, and first publishing experience enjoyable and exciting. Mengsha, you opened my eyes to a new discipline. Israel, your patience helped me carry through some of the most challenging times of my career. To Dr. Matthew S. Hunt, Dr. Channing Ahn, and Dr. Chi Ma, thank you for providing so much help in my research. To Dr. Mikhail Zhernenkov and Dr. Guillaume Freychet at NSLS-II, Dr. Peter Hosemann and Hi Vo from UCBerkeley, thank you for experimental assistance.

I want to acknowledge everyone in our group, who made going into lab a treat. Ottman, you are one of the most inspiring scientists I know. Daryl, Bryce, and Carlos, even in some of the hardest times, you always made me laugh. Luiza, Kai, Kewei, and Anthony, boardgame Sundays with you have been great getaways from work. Rebecca, Amy, and Ryan, thank you for all the support and always being willing to chat. Mike and Andrey, thank you for the career tips. To all my friends, my MCE cohort, everyone on the Housing team, and all my students at Page, you are both amazing and inspiring. You have carried me through the ups and downs of an eventful four years and brought me to where I am today.

To Dr. Hong Lu and Dr. Xinbao Zhang, you are the reason that I get to experience this world. Thank you.

ABSTRACT

Microstructure-governed damage resistance in materials enables a variety of functional applications, such as durable biomedical implants and robust product packaging. For example, the refined phase compatibility qualifies NiTi for artery stents, while carbon fiber reinforced polymers improve structural strength in aerospace engineering. As the overall size of industrial applications continue to decrease, it has become increasingly apparent that when a material's external structural size and internal microstructural size become comparable, its mechanical behavior starts to deviate from that of bulk, such as the smaller-is-stronger size-effect in metals. This elucidation necessitates the characterization of materials at lengthscales relevant to their internal microstructure to guarantee accuracy in the design of real-world applications.

This thesis aims at deciphering the microstructure-mechanics relationship for materials at lengthscales bridging the gap between $1nm$ and $1\mu m$, with shape memory ceramics, scorpion shells, and jellyfish biogel as sample systems. We use electron and x-ray diffraction to characterize microstructures such as twinning, defects, and fiber organization, while revealing strength, toughness, and other deformation mechanisms through *in-situ* nanomechanical experiments. We show improved shape recovery in an otherwise brittle ceramic by tuning its phase compatibility at the nanoscale and reveal unprecedented smaller-is-stronger size-dependence for its twinning-induced plasticity. We then unveil competing fiber orientations in Scorpion shells that follow fiber-mechanics principles and demonstrate a combined poroelasticity/viscoelasticity constitutive relation in jellyfish that explains their self-healing behavior. The correlation between microstructure and mechanical behavior unveils unique damage mitigation and energy dissipation techniques in both brittle ceramics and natural biomaterials at each order of lengthscale, paving the road to designing macroscopic materials with hierarchical mechanical behavior and improved plasticity.

PUBLISHED CONTENT AND CONTRIBUTIONS

Zhang, Haolu, Israel Kellersztein, Rebecca A. Gallivan, H. Daniel Wagner, and Julia R. Greer (n.d.). "Microstructure enabled fracture resistance in Scorpio Maurus Palmatus cuticles." In: *In Preparation* ().
H.Z. participated in the sample preparation and the microstructure characterization, designed and performed the mechanical experiments, and corresponding data analyses, and spearheaded the writing of the manuscript.

Zhang, Haolu, Justin Jetter, Hanlin Gu, Richard D. James, Eckhard Quandt, and Julia R. Greer (2021). "Size-dependence of zirconia-based ceramics via deformaton twinning." In: *Extreme Mechanics Letters* 42, p. 101124. DOI: 10.1016/j.eml.2020.101124.
H.Z. participated in the sample preparation, designed and performed the crystallographic characterization, mechanical experiments, and corresponding data analyses, and spearheaded the writing of the manuscript.

Jetter*, Justin, Hanlin Gu*, Haolu Zhang*, Manfred Wuttig, Xian Chen, Julia R. Greer, Richard D. James, and Eckhard Quandt (2019). "Tuning crystallographic compatibility to enhance shape memory in ceramics." In: *Physical Review Materials* 3, p. 093603. DOI: 10.1103/PhysRevMaterials.3.093603.
H.Z is a co-first-author of this work. H.Z. participated in the sample preparation, performed the crystallographic characterization, mechanical experiments, and corresponding data analyses, and participated in the writing of the manuscript.

Ni, Xiaoyue, Haolu Zhang, Danilo B. Liarte, Louis W. McFaul, Karin A. Dahmen, James P. Sethna, and Julia R. Greer (2019). "Yield precursor dislocations avalanches in small crystals: The irreversibility transition." In: *Physical Review Letters* 123, p. 035501. DOI: 10.1103/PhysRevLett.123.035501.
H.Z. participated in the sample preparation, experiments, data analysis, and the writing of the manuscript.

TABLE OF CONTENTS

LIST OF ILLUSTRATIONS

LIST OF TABLES

Chapter 1

INTRODUCTION

As the effective size of engineering applications continues to shrink in important industries such as consumer electronics, biomedical devices, energy storage, etc., the need for systematic design and improvements in the mechanical behavior of materials at the micro- and even nanoscale becomes increasingly important. Improved understanding of the stress distribution under nanoindentation for different materials [1, 2] and its more recent adaptations [3, 4] have enabled systematic *in-situ* studies of microstructure-governed post-elastic deformation (plasticity [5], fracture [6, 7], buckling [8], densification [9], etc.) at scales as small as a few nanometers [10] in a plethora of materials such as porous metals [11], amorphous-crystal composites [12], biomaterials [13], lattices [14], and functional metamaterials [8]. A variety of miniaturized testing configurations have been developed, such as compression [15], tensile testing [16], and bending [7, 17] under varied environmental control, for example cryogenic temperatures [18]. With the abundance of covered topics, nanomechanical experimentation has quickly transitioned from a scientifically intriguing research direction to a handy tool for the investigations of more complex systems such as hierarchical arhitected materials [19], textured shape memory alloys [20], and biocomposites [21].

1.1 Mechanics at Different Lengthscales

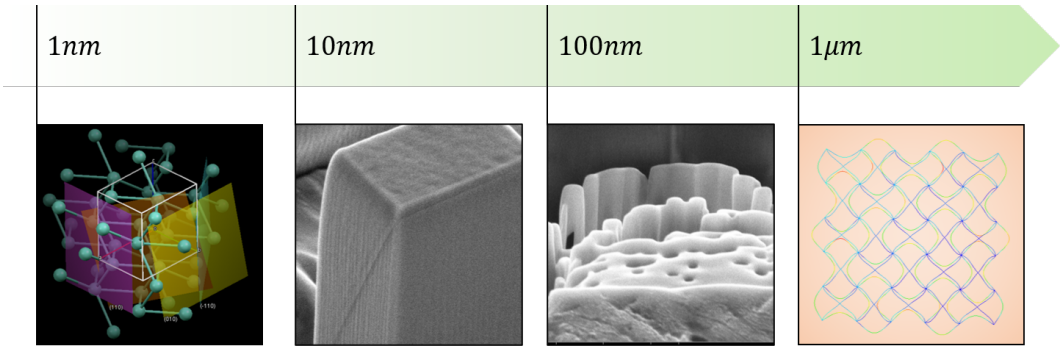

Figure 1.1: Microstructure at different relevant lengthscales presented in this work, with (left to right) crystal lattice transformation [22], dislocation-governed plasticity, fiber-reinforced composite [23], and lattice-based mechanics.

While conventional engineering often treats materials to be homogeneous, studies have repeatedly shown that as application size decreases to approach that of its material microstructure lengthscale, its mechanical properties change dramatically, whether through brittle-to-ductile transitions [24–26], size-effect due to dislocation networks [27], or homogenized random buckling [19, 28, 29]. It is therefore necessary to probe the physical origin of material mechanical behavior at each relevant lengthscale to both explain and predict phenomenon such as material failure [15], increased toughness [30], microscopic noise [31], energy dissipation [32], etc.

1.1.1 Coherent crystal lattice deformation: Phase transformation

At the smallest scale that current mechanical instruments can probe, just above the atomic level, comes the crystal lattice deformations. One such example is the Martensitic Transformation, which is the backbone of shape memory alloys (SMA) [33] and entails a lattice distortion through a first-order, diffusionless, solid-to-solid phase transformation between a stable high-temperature phase (Austenite) and a stable low-temperature phase (Martensite) that can be triggered either through temperature change or external stress. In some materials such as NiTi, the strictly higher symmetry of the Austenite crystal structure than that of the Martensite creates a lattice distortion with reversible strain that is significantly higher than what can be achieved in conventional metals [34].

The shape memory effect of the aforementioned material systems is often quantified through two rubriks: pseudo-plasticity and pseudo-elasticity. Pseudo-plasticity is the plastic strain that can be achieved through stress-induced twinning (Martensite reorientation between different variants to comply with the applied stress); when the external boundary conditions return to its original state, the deformation remains. Upon heating to Austenite, the reoriented crystal recovers its starting shape (which is deterministic due to the unchanged boundary conditions), therefore giving it the prefix 'pseudo.' Pseudo-elasticity is the reversible A$\rightarrow$M transfromation through applied stress at just above the phase transformation temperature. While in-depth understanding for the functional performance of shape memory in metallic alloys has matured [20, 35, 36], its application to ceramics remains preliminary [37, 38], with many studies simply miniaturizing the macroscopic phenomenon of transformation toughening [39] and limited quantitative improvements on either their pseudoplastic strain or reversibility [40]. We will later tackle this problem in Chapter 2 of this work.

1.1.2 Dislocation-goverened plasticity

The external size-effect on dislocation governed yield strength without strain gradient has been studied in depth since its first systematic introduction through single crystal Ni pillar compression by Ref [41]. Since then, efforts have been made to build an all-emcompassing model that describes this behavior across the entire single-crystal empire, starting from the simplest fcc metals to low-symmetry, high internal friction ceramics [41–44]. Initially, the scaling of strength as a function of sample dimension was characterized by a power-law with exponents inversely related to the crystal's Peierls stress [27], and the phenomenon was qualitatively explained through the lack of existing dislocations in the sample to initiate plastic events. Later findings through 3D dislocation dynamics (3DDD) simulations confirmed that with finite number of dislocations in the sample (contrary to a near-continous dislocation network observed at the macroscale) it is the lack of mobile dislocations that drives up the yield strength [45]. In addition, the stoichastic and intermittent nature of dislocation avalanches, which manifests as strain bursts at the submicron level, triggered a whole area of statistical physics [5, 46–48], treating the elastic-to-plastic transition as a critical point that resembles a reversible-to-irreversible transition similar to many other drastically different systems such as seismic events, colloidal solutions, and granular materials [49–51]. This is not to say that plasticity does not exist before this transition — there is evidence to show that microplasticity, which is nondetectable at larger scales, can be prevalent at smaller scales, which challenges the idea of perfect elasticity altogether [52, 53].

Despite the abundance of material systems studied for the size effect, its physical origin remains a mystery. Phenomenolocal models have been suggested to explain the scaling exponent based on hardening mechanisms and a break-down of the mean-field approach [45] as well as incorporating the much older idea of geometrically necessary dislocations (GNDs) when a strain gradient is present [54, 55]. The failure in these models to pinpoint an intrinsic lengthscale that comes with fitting later prompted re-examination of the fits using the Matthew's critical thickness theory (CTT) [43, 56]. A detailed analysis was presented in Ref [57], which concludes that the CTT, originally developed for clean pristine semiconductor epitaxial layers, can be used to describe the origin of the size-effect (up to strain hardening) for any dislocation-governed plasticity, encompassing the more specific models such as GNDs. Statistically, there is not enough data to distinguish between a clear cut CTT fit from that of a powerlaw with arbitrary exponent, therefore the question now

comes down to whether it is possible to directly probe the CTT via cleverly designed experiments or restricted deformation mechanism, such as deformation twinning, which we will discuss in Chapter 3.

1.1.3 Fiber reinforced composites

Moving up the lengthscales ladder to tens of nanometers, we encounter bio-fibers such as chitin, keratin, and collagen, providing biological materials with integral mechanical properties while serving functional purposes [58, 59]. While the nature of biomineralization and self-assembly is still largely unsolved, the structure-mechanics relationship of these fiber architectures have been explored in depth [60–62]. Fibers, often considered anisotropic stiff elements, provide directional elasticity that can be arranged to produce different stiffness and strength profiles such as in wood, bone, and insect shells [13, 63], without the need of heavy strong engineering materials . These principles have been applied to many artificial fiber-reinforced composites to produce materials with superior stiffness, strength, ductility, energy dissipation, and toughness [64, 65]. While site-specific nanomechanical experiments have been proven to yield reliable results for complex bio-composites [13, 17], nature still holds immense opportunities and inspiring lessons for the mechanics community to learn from, such as the intricate fiber structure in Arthropods and the viscoelastic recovery in jellyfish, discussed in Chapter 4 and 5, respectively.

1.1.4 Cellular solids

The mechanical behavior of cellular solids such as foams straddles between continuum and structural mechanics. Among their interesting properties, two of the most well-known are the scaling of stiffness and strength with relative density. Controlled fabrication of ordered cellular materials with nanometer-thick features was made possible by breakthroughs in the additive manufacturing field [19, 66]. Interestingly, in cellular metals with high relative density (80% dense), the size effect from the hundred-nanometer thick microstructure is still prevalent, reinforcing the importance of incroporating microstructure-governed deformation even in larger scale mechanics [11]. While extended research shows that the scaling of strength and stiffness with relative density in periodic lattices is highly dependent on node geometry [28, 32], there is still debate on how to approach the fracture mechanics of such discrete-continuum-hybrid materials [67]. In addition to strength and toughness, efforts have been made to recreate the crystal phase transformation induced shape

memory using metamaterials [68], albeit limited to 2D and theoretical cases, with potential to extend into 3D lattices.

1.2 Progression of *In-situ* Nanomechanical Experiments for Plasticity

Since the developement of nanoindentation in the 1980s [69], experimental nanomechanics has come a long way. Initially designed for engineering materials and thin films, gradual instrumental refinement over the past 40 years have enabled complex testing configurations (quasistatic loading, dynamic loading with precise control, etc.) under extreme conditions (high or low temperatures, hydration, *in-situ* TEM, etc.) using custom set-ups (MEMS devices, push-to-pull tensile tests, etc.). With the decreasing feature size in additive manufacturing and constantly increasing material selection suitable for nanoscale testing, this opens doors to unveiling many deformation mechanisms that we were not previously able to probe.

1.2.1 Experiments on conventional fully-dense materials

Based on the Vickers hardness tests, which have been around for almost a century, nanoindentation was first introduced in the 1980s to characterize material behavior of thin films and to precisely map the modulus and hardness of the material with submicron-level microstructure [1, 2, 69]. At the transition of the bicentennial, studies on the external size effect with plastic strain gradients revived the interest in the understanding of plasticity in miniaturized materials [55, 70]. In 2004, Ref [41] developed a method to use Focused Ion Beam (FIB) etching for uniaxial pillar compression experiments that can be used to readily extract the yield stress of micrometer-size Ni samples, which was then extended to submicron samples in Ref [3]. Since then, this method has been adopted to measure the size-effect of many other material systems [27], and was confirmed via mirrored tensile experiments [42].

The success of the etched pillars were challenged due to the beam damage during fabrication [71]. In 2011, electroplated pillars were shown to exhibit the same scaling behavior, despite never being exposed to the FIB [4], debunking the notion of a damaged layer preventing dislocations from escaping at lower stresses. It is worth noting that despite evidence that ion-implantation and amorphorization from beam etching have negligible effects on monolithic metals and ceramics, one needs to be careful when using it for complex or soft materials, expecially those that are

highly porous, where the amount of material redeposition can greatly affect the results [72].

In addition to tension, increasingly complex testing geometries have been developed for the measurement of properties such as fracture toughness [7, 21], which lacks standard testing procedures at the submicron level. This effort generated cantilever deflecting, adapted 3-pt bending, and center-notch tensile geometries [7, 67]. Recently, experiments on bone have produced repeatable and reliable results for the fracture toughness and energy absorption rates in complex biological materials [21].

1.2.2 Experiments with environmental constraints

The quantification of many material properties require testing with environmental control, such as for biomedical applications under physiological conditions and for crystals on extraterrestrial planets. Here we briefly outline the set-up and developements for different temperature conditions.

Nanomechanical experiments at high temperatures are known to suffer from thermal drift. While many instrument providers state stable testing in their equipments up to $800°C$, there are very limited records of peer-reviewed work with nanomechanical testing up to that temperature. This can be due and not limited to a few different reasons: (1) the temperature measurement in some instruments are not accurate and relies on the temperature control of the heating unit, which generates large errors at high temperatures; (2) the rapid cooling system, which runs on a liquid circuit, can become dangerously unstable in vacuum; (3) for stablized temperature, the tip and sample needs to be in contact for an extended period of time to avoid temperature gradients, during which drift and instabilities can easily crush the sample if it is small and/or fragile. In fact, this was our experience with the Hysitron PI88 system, which we will discuss in more detail in Chapter 2. Despite these challenges, there exist in-air nanoindentation results for creep at high temperatures [73] and *in-situ* high temperature TEM pillar compression capabilities with special types of materials [74]. Generally speaking, one needs to be wary of testing miniature-sized samples at elevated temperatures before reliable instrumentation is developed.

Compared to high-temperature experiments, testing at low- or cryogenic temperatures have proven to be much simpler [15, 18], often only requiring doses of liquid nitrogen. At these lowered temperatures, all noise quiets down and material behavior becomes more stable. Mechanisms such as diffusion, dislocation climb, or alloying become muted, making way for cleaner measurements of its mechanical behavior.

1.2.3 Potential in custom nanomechanical capabilities

Progression in additive manufacturing have opened the door to complex testing geometries for experimental nanomechanics. For example, while recent studies have succeeded in measuring fracture toughness using center-notch tensile tests [67], 3pt-bending geometries [21], and adapted cantilever deflection [7], less restrictive testing protocals are necessary for materials that can not be directly printed, do not respond well to the FIB, or have complex energy absorption mechanisms. Possible geometries for this type of tests include ASTM methods using compression [75]. On the other hand, improvements on Digital Image Correlation using electron images provide an alternative route to directly measuring the stress distribution and concentration for plasticity and fracture analysis at the nanoscale [76], which provides immense opportunities for the quantification of microstructure evolution in crystal phase transformation, plastic deformation via twinning or slip, fiber-induced local buckling, and stress distribution in nanolattices under nonuniform loading.

1.3 Objectives and Outline

In this work, we focus on the post-elastic deformation mechanisms of a wide range of materials at lengthscales relevant to their intrinsic microstructure. We tap into the general principles discussed in Section 1.1 and use methods described in Section 1.2. The results shed light on the usage of nanomechanical instruments and accumulated knowlege to decipher material behavior and their function in larger-scale systems, providing guidelines to designing novel artificial materials with superior properties.

The thesis is outlined as follows: Chapter 1 provides an overview of the developement and current state of experimental nanomechanics with a focus on the external size-effect. Chapter 2-5 describe four projects that focus on the mechanical behavior of materials with microstructure at gradually increasing lengthscales, each aimed at tackling a different question from Section 1.1. Chapter 2 presents the quantified one-way shape memory effect of a brittle ceramic via phase transformation. Chapter 3 extends on that notion and delves more deeply into the twinning mechanism and its size effect in said ceramics. Chapter 4 shifts from a monolinic material to a bio-composite, focusing on the fiber-governed structure-mechanics relationship of Scorpion shells. Chapter 5 looks at a different biomaterial at a close-to-bulk lengthscale, using indentation to characterize the time-dependent behavior of jellyfish. Chapter 6 summarizes the work and provides insights and outlook for potential future studies.

Chapter 2

$(ZrHfO_4)_x(YTaO_4)_{1-x}$ SHAPE MEMORY CERAMICS

Jetter*, Justin, Hanlin Gu*, Haolu Zhang*, Manfred Wuttig, Xian Chen, Julia R. Greer, Richard D. James, and Eckhard Quandt (2019). "Tuning crystallographic compatibility to enhance shape memory in ceramics." In: *Physical Review Materials* 3, p. 093603. DOI: 10.1103/PhysRevMaterials.3.093603.

The extraordinary ability of shape memory alloys to recover after large imposed deformation motivates efforts to transpose these properties onto ceramics, which would enable practical shape memory properties at high temperatures and in harsh environments. The theory of mechanical compatibility was utilized to predict promising ceramic candidates in the system $(YTaO_4)_{1-x}(ZrHfO_4)_x$, $0.6 < x < 0.9$. When these compatibility conditions are met, a reduction in thermal hysteresis by a factor 2.5, a tripling of deformability, and a 75% enhancement in strain recovery within the shape memory effect was found. These findings reveal that predicting and optimizing chemical composition of ceramics to attain improved crystallographic compatibility is a powerful tool for enabling and enhancing their deformability that could ultimately lead to a highly reversible oxide ceramic shape memory material.

2.1 Introduction: From Shape Memory Alloys to Ceramics

The shape memory (SM) and the related effect of superelasticity occur in all classes of materials: metals [77], ceramics [78], and polymers [79]. Some crystalline solids display these effects with almost perfect shape recovery through a reversible first order phase transformation between a low-crystallographic-symmetry low temperature phase (Martensite) and a higher-symmetry high temperature phase (Austenite). Extensive investigations of such phase transformations have deepened fundamental understanding of shape memory effect in metallic SM alloys and facilitated a variety of emerging applications, for example NiTi-based SM alloys are now used as brain stents [80] and devices for minimally invasive surgery [81].

Properties of SM alloys depend significantly on the reversibility of the underlying phase transformation. Cyclic degradation, which manifests as the gradual decrease in one-way work (energy dissipated in one shape memory cycle) over repeated

activation, is common among metallic SMs [82] as a result of dislocation pile up in the region of phase transformation [83]. It has been shown in metals that the transformation hysteresis ΔT decreases [84] and fatigue properties improve [36] dramatically with greater kinematic compatibility between the lattice parameters of the transforming phases. Tuning lattice parameters by changing composition allows for optimizing macroscopic properties, i.e. hysteresis and functional fatigue. The strongest known conditions of compatibility are the so-called cofactor conditions [85]. These developments have significantly improved our understanding of metallic shape memory alloys (SMAs). For example, $Zn_{45}Cu_{25}Au_{30}$ exhibits extremely small thermal hysteresis of $0.2K$ and nearly full repeatability after 100,000 full transformation cycles at 7% strain and 700 MPa compression stress cycles [20].

Two-phase ceramic shape memory materials were actively investigated until the nineties, which led to the discovery of now well-known transformation toughened Zirconia-based ceramics [86]. This line of research stagnated as the materials approached their technological limits, with very limited efforts dedicated to developing shape memory ceramics that display metal-like shape memory properties [87]. Various approaches have been used to change the transformation temperatures of matrix and particles, e.g., solid solutions formed with CeO_2 [88] or stabilization by Y_2O_3 [89]. The superelastic and shape memory behavior was demonstrated in freestanding $CeO_2 - ZrO_2$ pillars of approximately 1μm diameter [78]. Due to the high transformation temperatures and low compatility, the extent of SM effect in ceramics stops at a few cycles of superelasticit (reversible mechanically-induced phase transformation) and limited one-way SM effect through phase transformation from retained metastable Austenite. Here, we show that the success in improving the repeatability and lowering of the superelastic hysteresis and shape memory effects in metallic SMAs by satisfying conditions of compatibility can be translated to oxide ceramics.

Ceramics in the system $(YTaO4)_{1-x}(ZrHfO4)_x$, with $0.6 < x < 0.9$ were fabricated, where transformation between Tetragonal (Austenite) and Monoclinic (Martensite) had been identified previously [87]. The minimum hysteresis ΔT was found to be around $x = 0.735$, where the theorized highest compatibility is met [90]. We use crystallographic characterization combined with nanomechanical experiments to demonstrate the highest SM effect in $x = 0735$ samples compared to other compositions and ceramic SM materials in general.

2.2 Material Characterization and Crystallographic Analysis

Disks with 5mm diameter and 2mm thickness where ball-milled, pressed, and sintered by our collaborators in the Quandt group at University of Kiel, following steps illustrated in [90]. We expect different behavior in samples with different composition governed hysteresis; this difference was immediately evident as samples with high hysteresis disintegrate after a couple of heat cycles as a result of transformation-induced cracking at grain boundaries. To fully understand the microstructure-enabled deformation and recovery, we use a series of imaging and diffraction methods to visualize, identify, and characterize the crystallography, phases, and microstructure within samples of various compositions. The revealed microstructure serves as a basis for the design and understanding of mechanical experiments that then enable the full-circle analysis of the shape memory effect at the microscale.

2.2.1 X-ray diffraction (XRD)

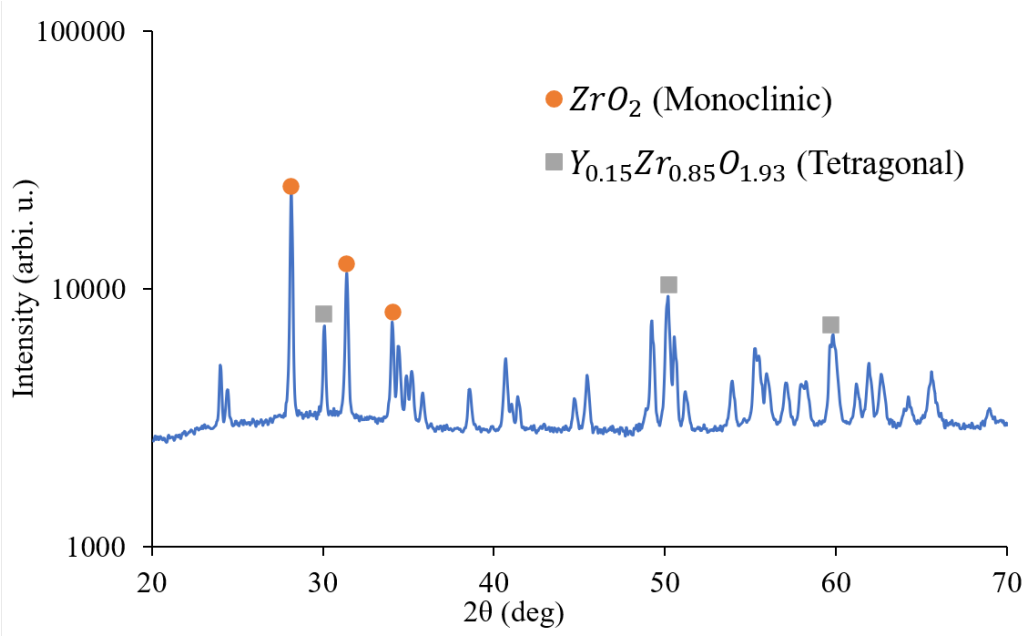

Figure 2.1: X-ray diffraction data for $x = 0.75$ sample showing diffraction peaks that closely match that of Monoclinic Zirconia and Tetragonal Yttrium-doped Zirconia.

Preliminary XRD scans at room temperature using PANalytical X'Pert Pro in the Faber group at Caltech on samples of different compositions. A representative diffraction curve is shown in Fig.2.1, where clear peaks that match the close-packed

planes of both Tetragonal and Monoclinic $ZrYO_4$ (Yttrium-doped Zirconia) were identified. This reveals the co-existence of the two phases at room temperature, as is often observed in ZrO_2 based ceramics [91–95].

Accurate temperature dependent lattice parameters of each sample were obtained through high-temperature XRD at our collaborator's site [90], which enabled us to analyze data from more complicated diffraction tests such as EBSD and TEM.

2.2.2 Electron Backscattering Diffraction (EBSD)

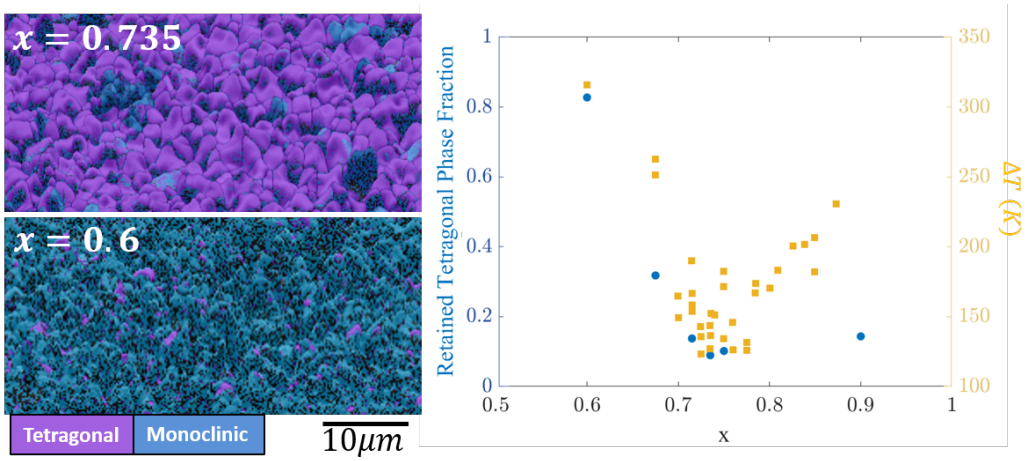

Figure 2.2: Phase mapping obtained from EBSD on the surface of polycrystalline samples of two distinct compositions. A clear V-shaped correlation is seen between the Tetragonal phase fraction and the compositional make-up of the material with a minimum at $x = 0.735$.

EBSD scans on surfaces of 6 samples with various compositions between $x = 0.6$ and $x = 0.9$ were conducted using a ZEISS 1550 VP Field Emission SM in the Caltech GPS Division Analytical Facility. Representative maps of two samples with $x = 0.6$ ($\Delta T = 315K$) and with $x = 0.735$ (minimum $\Delta T = 120K$) are shown in Fig. 2.2. We reveal dual-phase polycrystals with Tetragonal and Monoclinic grains randomly distributed, while there are significantly higher fractions of the metastable Tetragonal grains in the $x = 0.735$ sample, which has the lowest measured hysteresis ΔT and therefore the highest compatibility. We evaluated the phase fraction by integrating the area in each phase for 6 different compositions and revealed a minimum in the retrained Tetragonal phase fraction at $x = 0.735$ with the same V-shape as the measured hysteresis. To further analyze the relationship between phase fraction and compatibility, we plot them against the normalized hysteresis (A_s

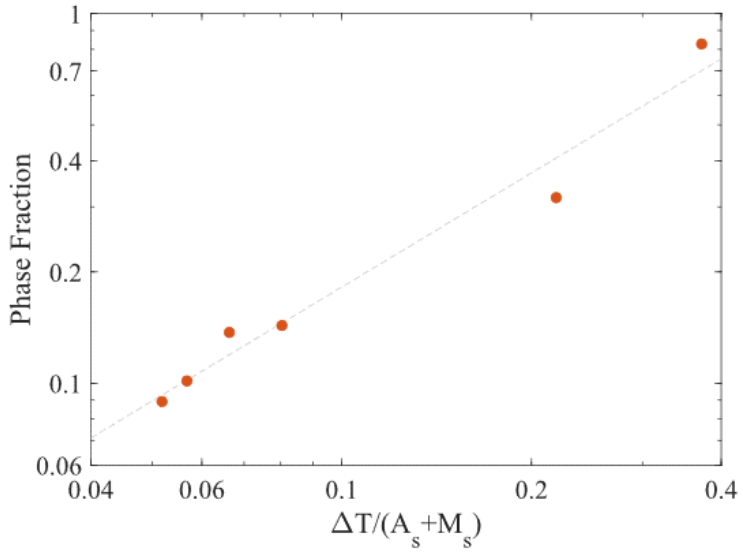

Figure 2.3: Tetragonal phase fraction linearly increasing with normalized hysteresis.

is the starting transformation temperature for A→M during cooling and M_s is the starting transformation temperature for M→A during heating), shown in Fig. 2.3, where a linear relationship was uncovered.This correlation is hypothesized to be due to, at least partially, the high compatibility at $x = 0.735$ that allow for easier stabilization of the metastable Tetragonal phase at room temperature.

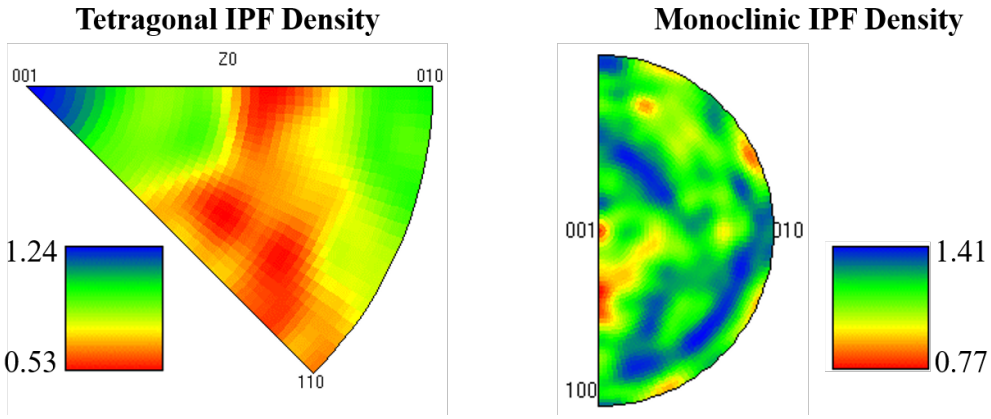

Figure 2.4: IPF contours for the two phases in a $300\mu m$ by $100\mu m$ scan on a $x = 0.675$ sample, revealing preferred orientations for the metastable Tetragonal grains and random distribution in the Monoclinic grains.

Because of the phase transformation mechanism, there is a small strain in the Tetragonal [001] direction to the Monoclinic [010] direction. Therefore, on the surface of the sample where there is little constraint in the surface normal direction,

grains with their [001] axis in the Tetragonal phase at high temperature are more likely to remain unchanged during cooling. This is confirmed by the integrated Inverted Pole Figure (IPF) at room temperature for the two phases for a $x = 0.675$ sample, as is shown in Fig. 2.4, where the Tetragonal grains have a much higher probability to be oriented with the least strain on the surface (highest density for [001] along the surface normal), while the Monoclinic grains are more uniformly distributed.

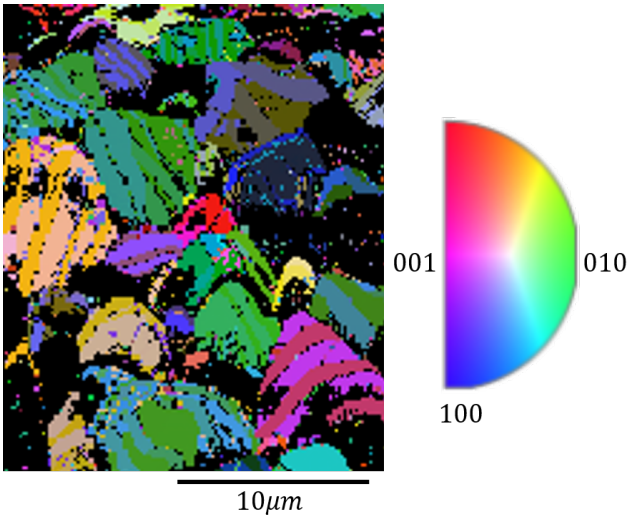

Figure 2.5: Clear twin domains within Monoclinic grains in a $x = 0.75$ sample with the corresponding IPF.

For Martensitic shape memory effect and pseudoplasticity, we focus on the Monoclinic grains (Martensitic, lower temperature stable phase). EBSD maps show clear twin domains within individual Monoclinic grains, as those seen in Fig. 2.5. Here the white borders represent the grain boundaries, whereas the different colors represent crystal orientation with the legend shown on the right hand side IPF.

2.2.3 Energy Dispersive Spectroscopy (EDS)

Apart from orientation dependence, heterogeneities in the elemental contribution can also influence the phase transformation process. EDS mapping reveals aggregation of Yttrium in Tetragonal grains (Fig. 2.6), with 70% increase in Yttrium content in Tetragonal grains (Table 2.1), while other elements are uniformly distributed. Since Yttria content contributes to stabilization of the Tetragonal phase and less prominent aging effects [39, 91], the heterogeneity during sample fabrication and sintering likely prevented these Yttrium-contrentrated regions from transform-

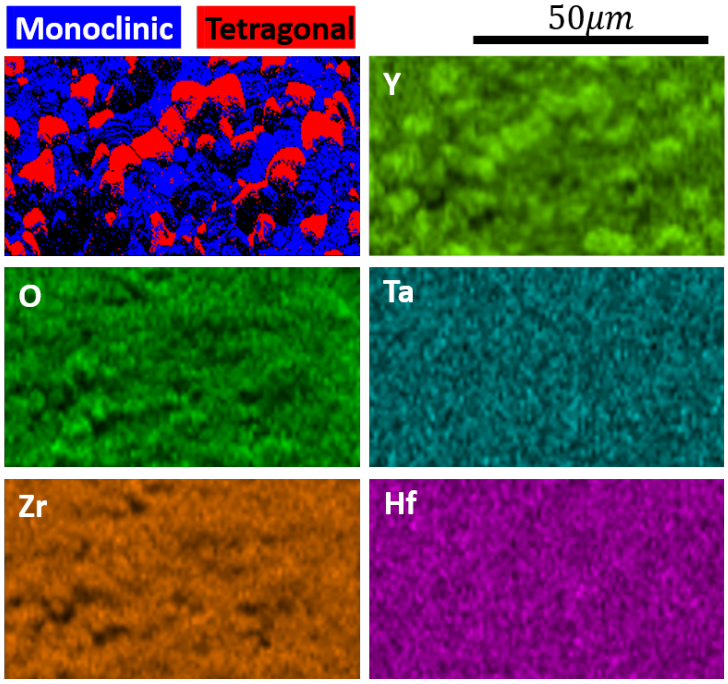

Figure 2.6: EDS analysis showing aggregation of Yttrium in Tetragonal grains.

Element	Tetragonal	Monoclinic
O	19.9 ± 0.2	17.8 ± 0.2
Y	12.2 ± 0.3	7.3 ± 0.3
Zr	25.5 ± 0.3	28.5 ± 0.3
Ta	13.9 ± 0.2	14.1 ± 0.2
Hf	28.5 ± 0.3	32.3 ± 0.3

Table 2.1: Weight percentage of different elements in the two phases in a $x = 0.715$ sample, with significantly higher Yttrium concentration in Tetragonal grains.

ing to the more stable Monoclinic phase due to low energy difference and high energy barrier.

2.2.4 Transmission Electron Microscope (TEM)

Further investigations of the Monoclinic twin systems were conducted under the TEM using the Tecnai TF30 in the Caltech Kavli Nanoscience Institute (KNI). Samples were prepared with the FEI Versa Dual beam with an EZlift nano-manipulator and deposited Pt for protection. Fig. 2.7a contains a TEM image of a Martensite grain in a low hysteresis sample ($x = 0.735$, $\Delta T = 120K$) and reveals a twinning microstructure with laminates ranging from 40 to 500 nm in thickness. Fig. 2.7b shows its bright field (BF) image with a [001] zone axis (za) in the Martensite

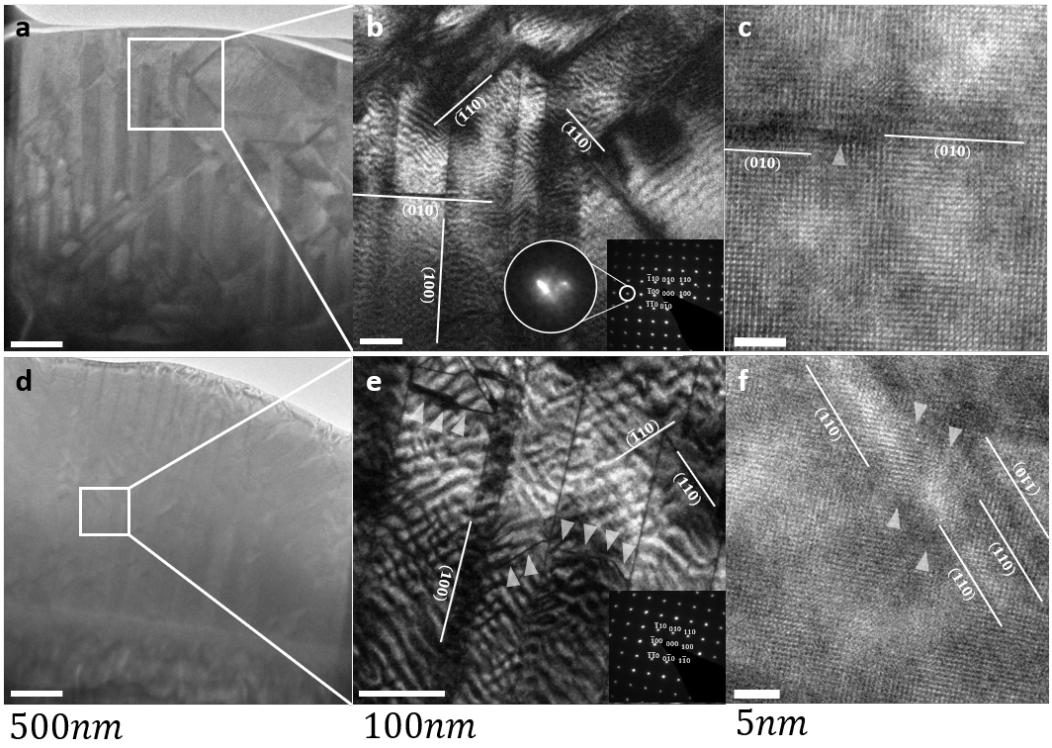

Figure 2.7: TEM imaging of samples with (a-c) $x = 0.735$ and (d-e) $x = 0.6$, where clear twin domains and mirror planes were observed. (a,d) TEM images of entire twin-populated grains. (b,e) Close-up BF images containing mirror planes and defects, with the corresponding indexed DP. (c,f) HRes images of twin boundaries.

basis, where the corresponding indexed diffraction pattern (DP, inset) for the grain contains no twinning patterns, which suggests that all variants share the common two-fold axis [001]. The blown up $(\bar{3}00)$ spot which demonstrates a triplet-like feature is a clear evidence for preexisting twins. No visible defects were observed within any variant, which indicates that the crystal is in a low-energy state with minimal internal stresses. The majority of twinning planes are found to be along (100), (010), and (110) type planes, which supports the theoretical prediction that for $x = 0.735$, the sample contains the maximum number of Austenite/Martensite interfaces. High resolution (HRes) TEM images reveal that the mirror planes are mostly coherent, with an occasional incoherency, for example the partial dislocation cutting through a (010) plane highlighted by an arrow in the high-resolution image in Fig. 2.7c. TEM images of a high-hysteresis sample ($x = 0.6$, $\Delta T = 315K$) reveal similar twinning microstructures at the near-micron scale shown in Fig. 2.7d. Further investigation with BF at a higher resolution (Fig. 2.7) shows that although the twinning direction and mirror planes are identical to those in the low-hysteresis sys-

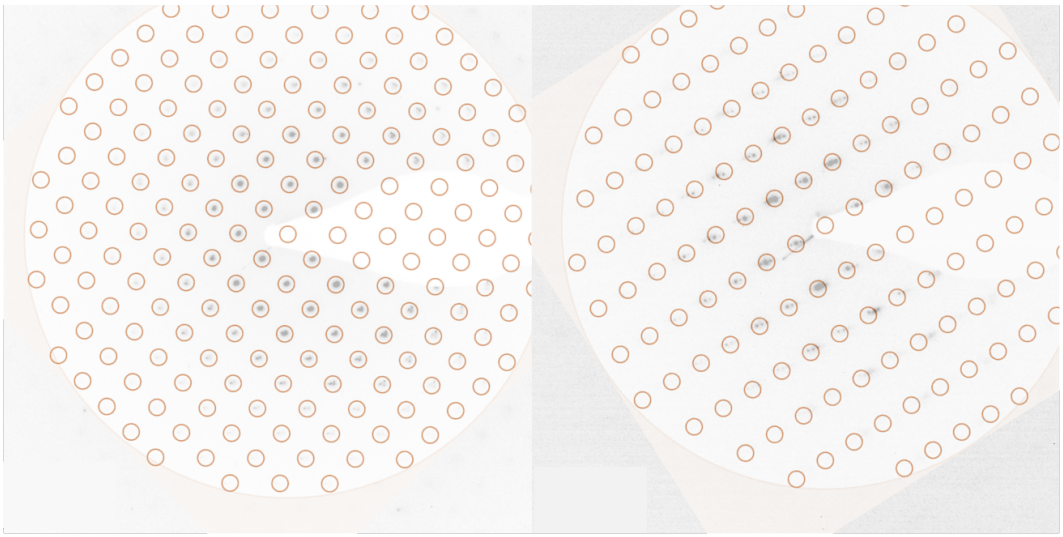

Figure 2.8: Examples of theoretical DPs overlayed on experimentally generated ones. (left) $za = [001]$. (right) $za = [1\bar{1}0]$.

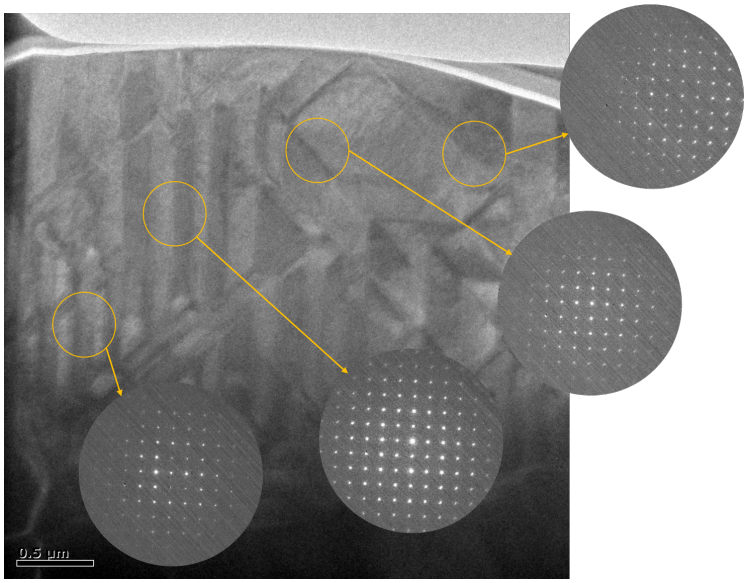

Figure 2.9: SAD patterns generated from different locations using a $10\mu m$ aperture, showing the same closed packed planes.

tem, the crystal is much more distorted and is populated with dislocations, which cut through individual variants (indicated by the small arrows). The high-resolution image of the high-hysteresis sample in Fig. 2.7 displays a complicated twin-boundary structure with multiple dislocations. This microstructural analysis supports that the high-hysteresis sample contains greater internal stress during phase transformation compared with the low-hysteresis system, as a result of its low compatibility.

Due to the almost cubic-like Monoclinic crystal structure, the diffraction patterns were almost indiscernible at miller indices with lower symmetry than $\langle 111 \rangle$. We used a custom Matlab script to generate theoretical diffraction patterns and identify the highest match for each measured diffraction pattern. Examples of matched DPs are shown in Fig. 2.8. Selected Area Diffraction (SAD) using the smallest aperture size ($10\mu m$) was used to confirm that the different variants in the sample indeed diffract similarly, which is shown in Fig. 2.9.

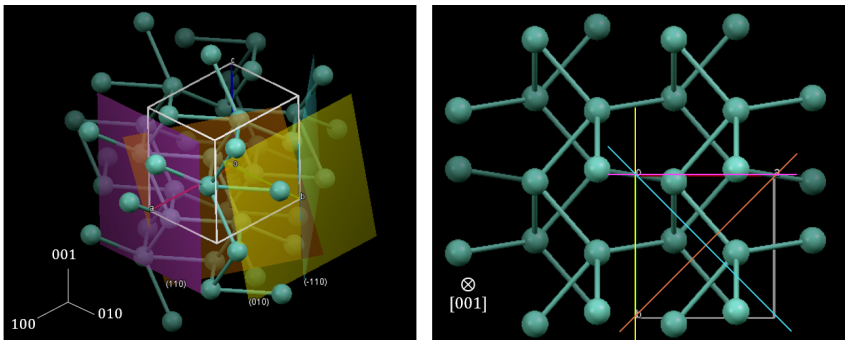

Figure 2.10: Crystallographic diagram showing the twin planes in (left) 3d view and (right) same view as in Fig. 2.9.

The observed DP and microstructure predict twin systems of $\{100\}\langle 001 \rangle$, $\{010\}\langle 001 \rangle$, and $\{110\}\langle 001 \rangle$, which is consistent with that reported for Zirconia after Tetragonal to Monoclinic phase transformation under a TEM [92]. The corresponding mirror planes in a pure Monoclinic ZrO2 crystal structure is demonstrated in 3D in Figure 2.10c and in 2D in Figure 2.10d with the same viewing zone axis as the TEM image in Fig. 2.9. The coherent mirror planes of $\{100\}$, $\{010\}$, and $\{110\}$ provide easily accessible glide planes for twinning dislocations and are therefore predicted to be the location for onset of plasticity.

Dark Field (DF) imaging was used to distinguish dislocations from other types of defects, as is shown in Fig. 2.11(left). In a defect populated $x = 0.6$ Monoclinic grain, a dislocation was observed to dissappear in DF with $\boldsymbol{g} = (010)$, implying Burger's vector of $[100]$ if it is a screw or $[001]$ if it is an edge. Twinned DPs were obtained with samples with different zas, an example of which is shown in Fig. 2.12, where a twin boundary cuts across the image diagonally, with the DF diffraction spot shown on the lower-left corner. The twinned DPs for the two sides are shown on the corresponding corners, with the lowest-order spots indexed. As per the index, a common variant with $za = [\bar{1}01]$ (marked in orange) extends through the figure, while two variants of $za = [01\bar{1}]$ (blue) and $za = [011]$ (green) sits on

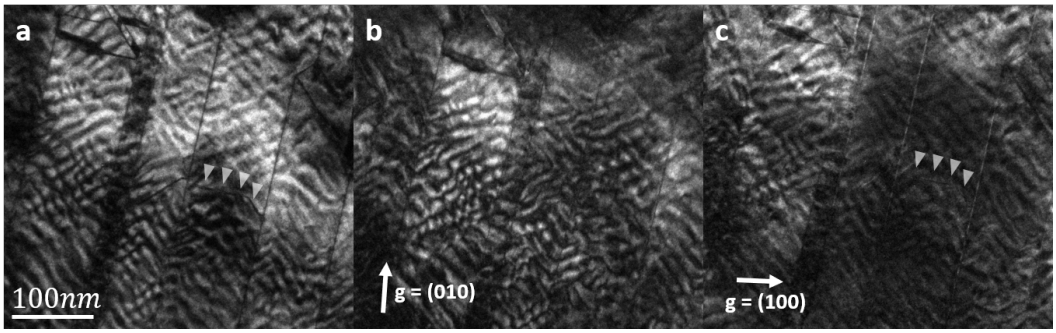

Figure 2.11: Close-up BF image as in Fig. 2.7 and corresponding DF images for a $x = 0.6$ Monoclinic grain (high $\Delta T = 315K$), where the marked dislocation disappears under the $\boldsymbol{g} = (010)$ condition.

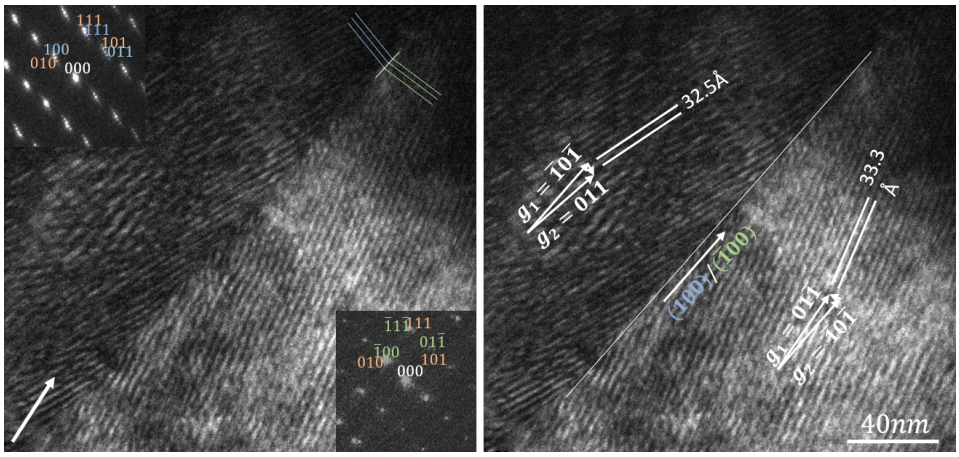

Figure 2.12: DF image from a different *za* between two twin variants with (left) corresponding DPs and (right) Moiré fringes.

top on either side of the observed twin boundary. A diagram of the twin junction between the $[01\bar{1}]$ and $[011]$ variants is shown on the upper-right corner. Fig. 2.12 (right) repeats the same DF image with the twin boundary crystallographic plane marked. The measured Moiré fringes and their originating diffraction spots are also shown, with the direction and spacing matching what is theoretically predicted.

With the low-symmetry nature of the Monoclinic crystal structure, it was hard to discern defects in atomic planes using original HRes TEM images. We used a custom filtered Fast Fourier Transform (FFT) and inverse FFT (iFFT) script in Matlab to visualize the heterogeneities in the atomic planes cutting orthogonal to the shown twin boundary in Fig. 2.13. Despite other heterogeneities in the generated plot due to other defects such as dislocations and diffraction quality, the twin boundary clearly appears as a non-uniform line of discontinuity in the middle of the lines of

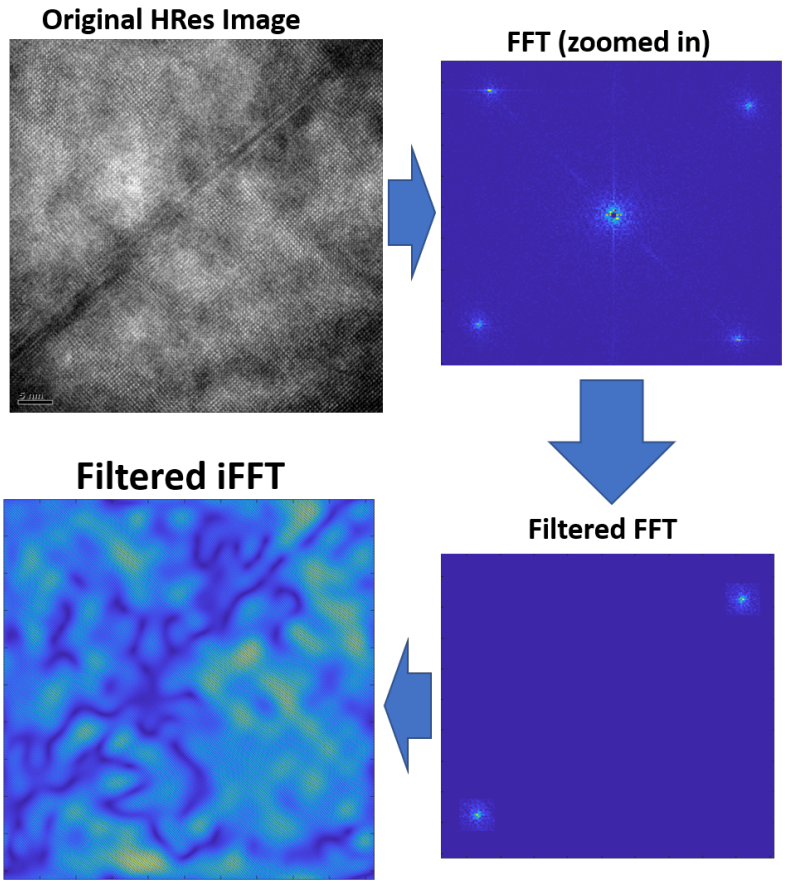

Figure 2.13: Filtered FFT showing the twin boundary as a discontinuity in the coherent lattice planes.

atomic planes.

2.3 Nanomechanical Experimental Methods

2.3.1 Sample preparation

Samples were sintered at $1400^{\circ}C$ for 48 hours to grow grains to $\sim 10\mu m$, which allows for singlecrystalline pillars of up to $2\mu m$ in diameter, fully contained within a grain. Monoclinic grains with suitable orientations (close to [100], [010], [101], [110], or [001] along the surface normal / loading direction) were chosen from the EBSD maps due to their easily accessible glide systems, by filtering orientations that are orthogonal to the [010] direction (Fig. 2.14). Samples were naturally electron-isolating, therefore carbon coatings of ~15nm were deposited prior to sample fabrication using a Turbo Carbon Evaporator in the Caltech GPS Division Analytical Facility. For uniaxial compression experiments, cylindrical pillars with

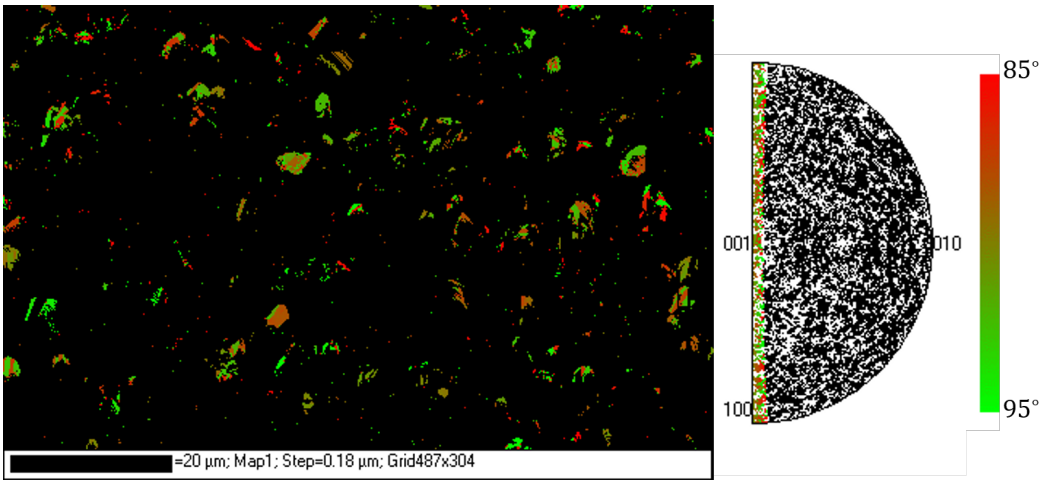

Figure 2.14: Grains with suitable orientations for uniaxial compression experiments.

1 : 3 aspect ratio and of diameters ranging from $200nm$ to $2\mu m$ were fabricated using a top-down concentric focused-ion beam etching method from the bulk samples using the FEI Versa Dual Beam SEM. Attempts to characterize grain boundary effects were made, with no conclusive results except for their overall brittleness, which is common among oxides; therefore only pillars contained within a single grain (no grain boundaries or cracks) were brought to further experimentation.

In addition to uniaxial pillar compressions in the bulk samples, we also carried out particle compression experiments *in-situ*. The particles were entire single-grains broken away from originally in-tack samples through repeated heating cycles (no mechanical force was used). The particles were compressed on a silicon chip without any physical or chemical binding techniques.

2.3.2 Compression experiments

In-situ mechanical experiments were carried out using a Hysitron PI-85 nanoindenter inside the Versa SEM to visualize deformation during the tests. Due to large drift, machine compliance, and substrate effects in the *in-situ* system, a custom Matlab script was used to track the displacement of the pillar during the tests (Fig. 2.15). For data collection, *ex-situ* experiments were carried out on larger quantities of pillars using the Hysitron triboindenter. For *ex-situ* tests, we calibrate the machine compliance beforehand, use drift monitor before the tests, and correct for the substrate effect by subtracting the Sneddon contribution [96], where the substrate modulus was measured using nanoindentation and found to be $34.5 \pm 7.5GPa$.

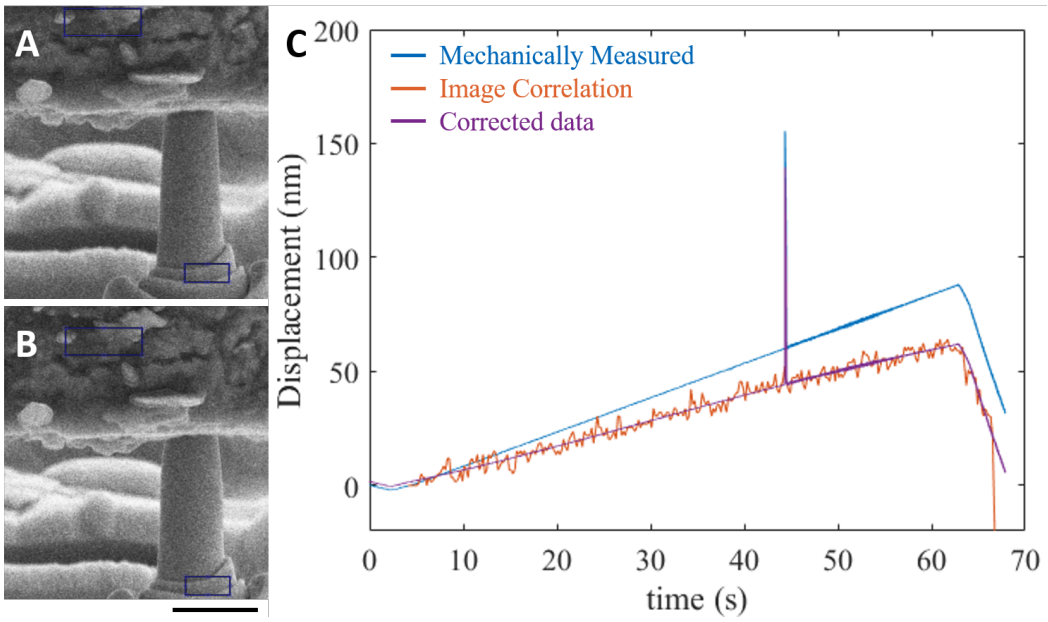

Figure 2.15: Displacement correction using recorded images during the mechanical experiments.

Further *in-situ* pillar compression at elevated temperatures were conducted using a Hysitron PI88 equiped inside an FEI versa SEM in the UC Berkeley Hosemann group, where both the tip and the sample (after coming in contact) were heated up to $400°C$ and held there for 15 minutes before carrying out each test.

2.3.3 Thermal treatment

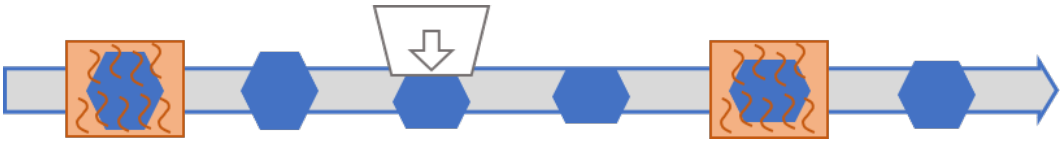

Figure 2.16: Demonstration of the thermal cycle used to characterize the shape memory effect.

The thermal process used to characterize the one-way shape memory effect is demonstrated in Fig. 2.16, with the following 6 steps:

1. Particles are heated to $100K$ above their transformation temperatures and cooled back down to reset their boundary conditions.

2. Particles are imaged for original shape.

3. Particles are compressed for deformation.
4. Post-compression particles are imaged for deformed shape.
5. Post-compression particles are heated to $100K$ above their transformation temperatures and cooled back down to trigger phase transformation and the one-way shape memory cycle.
6. Post-heated particles are imaged for recovered shape.

The original shape, deformed shape, and recovered shapes are then used to quantify the amount of recovery for two compositions with $x = 0.735$/low hysteresis/high compatibility and with $x = 0.6$/high hysteresis/low compatibility.

2.4 Shape Memory Recovery

With transformation temperatures above $600°C$, it is unrealistic to probe the pseudoelasticity of these ceramic samples, which required repeated cycling of austenitic samples at just above their transformation temperatures. We therefore probe the pseudoplasticity and characterize performance as the amount of shape recovery from heat treating a deformed particle. Pseudoplastic strain was first measured through pillar compression experiments, while the overall shape recovery was measured through particle compression and heat treatments. The heat cycle is described in section 2.3.

2.4.1 Significant pseudoplasticity as seen in pillar compression experiments

Example of an *in-situ* pillar compression experiment is demonstrated in Fig. 2.17, with the engineering stress-strain data and its corresponding pre and post compression SEM images. With Young's Modulus of $E = 160GPa$ and yield stress of $5.5GPa$, the pillar is both strong and ductile, attaining up to 6.2% pseudoplastic strain without failure. The surrated plastic flow represents twin plane propagation, where each newly nucleated twin overcomes a higher barrier and then takes slightly lower stress to propagate until it hits a barrier such as a pre-existing twin boundary, defect, or surface. The zig-zag-like prisms on the post-compression pillar are clear signs of twinned deformation.

Fig. 2.18 compares the compression response of two pillars with similar size ($\sim 900nm$ diameter) and original orientations (Fig. 2.18(left), inset) from two samples of different composition. Both pillars favor the $(100)[00\bar{1}]$ twin system: in

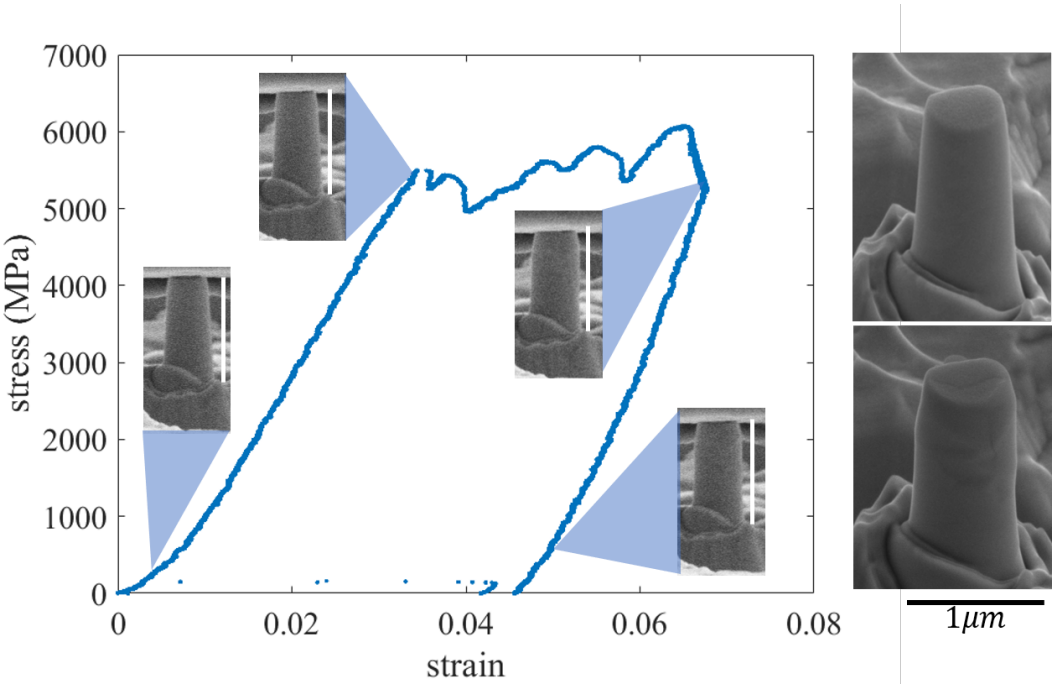

Figure 2.17: A $x = 0.735$ 900nm diameter pillar undergoing deformation twinning under compression.

the low-hysteresis sample, the onset of detwinning at about 800MPa is followed by a steady serrated flow at a constant applied stress, similar to the serrated detwinning stress plateau seen in the deformation of macroscopic metallic SMAs [97]. Unlike these previously studied systems, where the detwinning plateau is followed by a uniform nonlinear deformation due to incomplete reorientation [98, 99], the detwinning process in this pillar ends with a rapid strain burst at the same stress, which suggests that the reorientation is completed at 5.9% strain. This strain burst and the subsequent stress drop at 6.3% are clear signatures of dislocation-mediated slip in small-scale plasticity [46, 100], followed by steep plastic hardening starting at 6.6% strain. The high-hysteresis sample undergoes a similar process after the first detwinning event at about 800 MPa and has a significantly less recoverable strain from detwinning – it quickly transitions into the burst-governed plasticity at 1.3% strain, and begins to harden at 2.2% strain. After subtracting the elastic contribution, the retained pseudoplastic strain coming from detwinning (which is reversible upon heating) are found to be 5% for the low hysteresis sample (much higher than the 0.8% previously reported for Zirconia-based ceramics [78]) and 0.7% for the high hysteresis sample. This suggests that as the compatibility conditions become better satisfied, the post-elastic deformation mechanism transitions from a detwinning

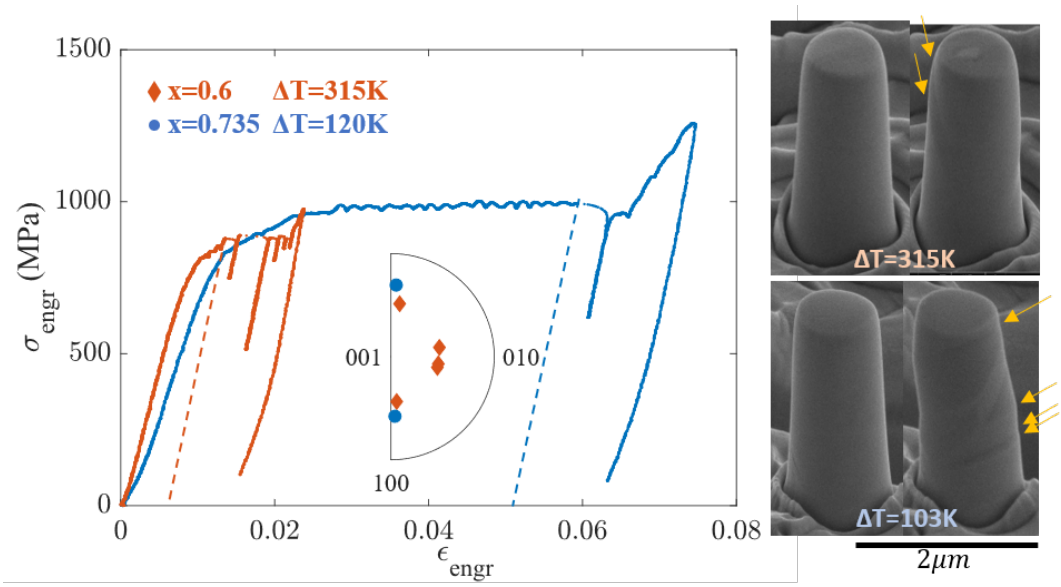

Figure 2.18: Comparison of plasticity in two pillars of similar orientation and size in different composition/hysteresis samples.

process to dislocation-slip. This could be related to the pre-existence of defects in the high-hysteresis system as shown in Fig. 2.11. The twin bands (indicated by the yellow arrows in Fig. 2.18) are clear visual evidence of detwinning in the pillars.

2.4.2 Temperature dependence of plastic deformation in both phases

As the most straighforward way to determine shape memory performance, the pseudoelastic one-way work (stress-strain hysteresis) needs to be measured at just above the tranformation temperature ($\sim 700^{\circ}C$). Attempts at compressing Tetragonal (Austenite) pillars were made, where pillars were fabricated out of metastable Tetragonal grains at room temperature and compressed at elevated temperatures *in-situ*. However, performing nanomechanical experiments at temperatures as high as $700^{\circ}C$ in vacuum proves to be difficult; apart from thermal drift and diffusion, which takes over at high temperatures in miniature samples, the cooling system becomes unstable and is subject to leakage and plasmonic effects that are damaging to the instrument. Despite many manufacturers advertising their instruments to be functional up to $800^{\circ}C$, very few credible published works achieve that target, with a few in the $400^{\circ}C$ range [101–103] and some going above $1000^{\circ}C$ with complex instrumental setup, data manipulation, or specific functional materials [104, 105]. We attempted at probing pseudoelasticity at high temperatures nevertheless, with limited success.

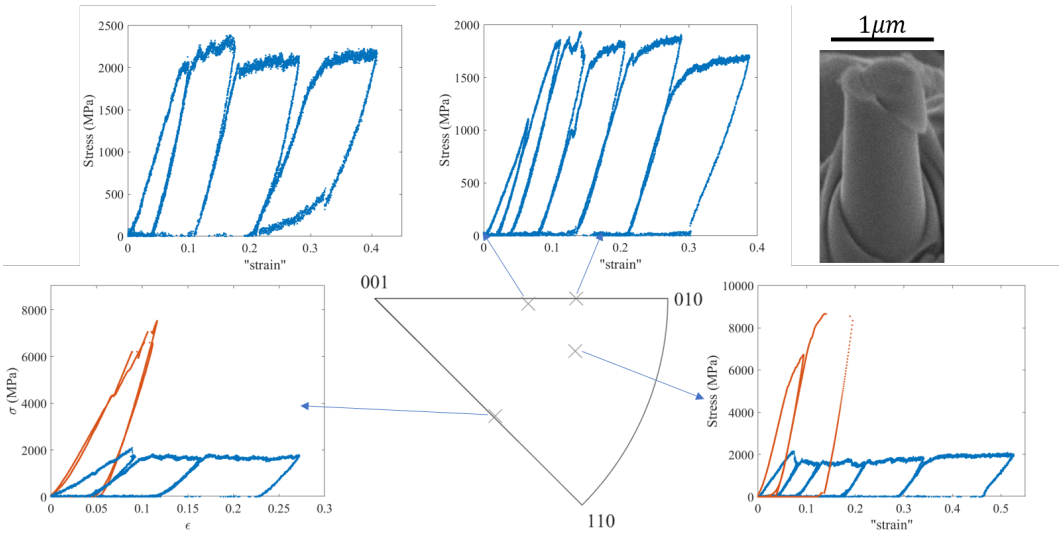

Figure 2.19: Tetragonal pillars of a $x = 0.715$ sample with different orientations undergoing single-slip plastic deformation at nominally $700°C$ (blue) compared to at room temperature (orange).

Fig. 2.19 shows the mechanical response of four Tetragonal pillars of different orientation at nominally $700°C$ in blue (the machine prevents exact measurement of the real sample temperature, and the nominal $700°C$ is simply the prescribed temperature) and at room temperature in orange. All six pillars undergo single-slip plastic deformation at constant flow stress. No phase tranformation was observed at either temperature, likely because these are pillars in the metastable Tetragonal phase at room temperature, where the high compatibility and elevated dislocation mobility gave preference to dislocation activity instead of lattice distortion. It is worth noting that due to high and unmeasurable drift at high temperatures, the "strain" of these compression tests remain questionable. Despite discrepancies between the measured strain, the evident decrease in yield stress and disappearance of hardening at elevated temperatures confirm the increase of dislocation mobilities.

The temperature dependence of detwinning stress / pseudoplastic response of Monoclinic pillars was studies through compression of three pillars at different temperatures, the results of which are shown in Fig. 2.20. The existence of grain boundaries prevent any conclusive results, yet it is already clear that at $400°C$, it takes at most half the stress to initiate deformation twinning than at room temperature. It is also evident that the grain boudaries remain rigid and brittle at $300°C$.

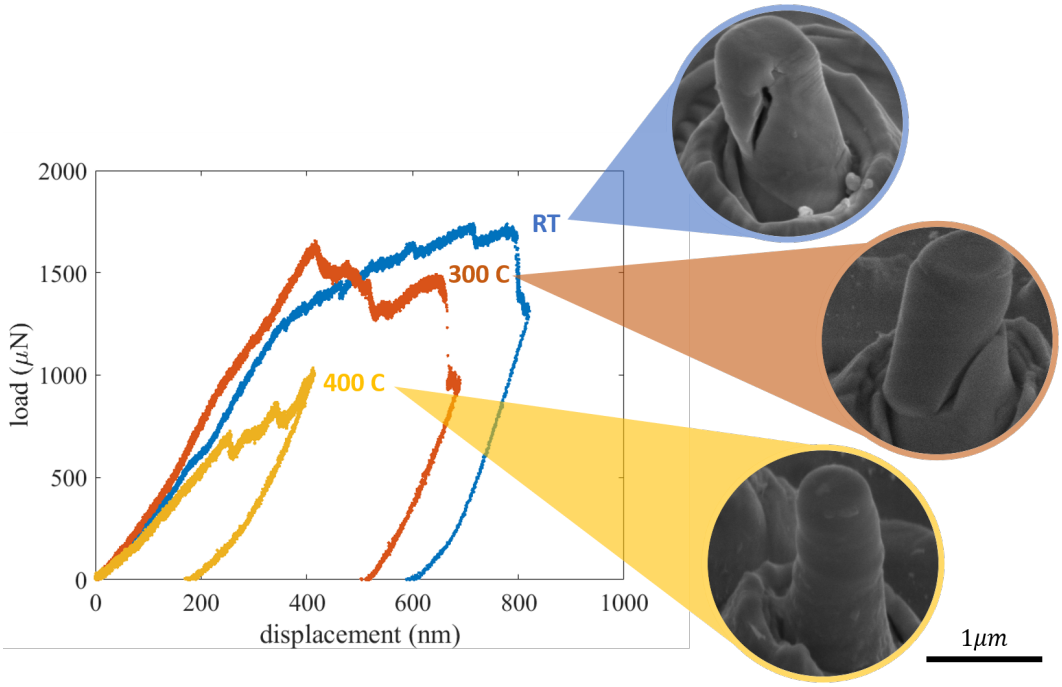

Figure 2.20: $x = 0.715$ Monoclinic pillars deforming via twinning at different temperatures.

2.4.3 Caveats of the pillar geometry

Fibbing, as a fabrication technique, changes the boundary conditions of the remaining material of the pillar. As a result, when the fibbed pillars are heated to above their transformation temperatures (without mechanical deformation at any point), it changes shape because of the newly created surface being on the same lengthscale as the twinning microstructure, as is demonstrated by Fig. 2.21. This is reminiscent of the wrinkling effect from polished Martensite surfaces being heated to transformation in earlier studies of SMAs and recent work of thin films [106]. The irregular shape change as seen in Fig. 2.21 is, unfortunately, inevitable, preventing quantitative measurements of the strain and shape recovery, which undermines the sole advantage of pillar experiments.

2.4.4 3D particle shape reconstruction and strain mapping

Example of a particle compression experiment and the corresponding measured mechanical data are shown in Fig. 2.22. The particle undergoes step-wise plastic flow, where each step represents the propagation of a twin plane until it is depleted, at which point a higher stress is needed to propagate the next twin. From the *in-situ*

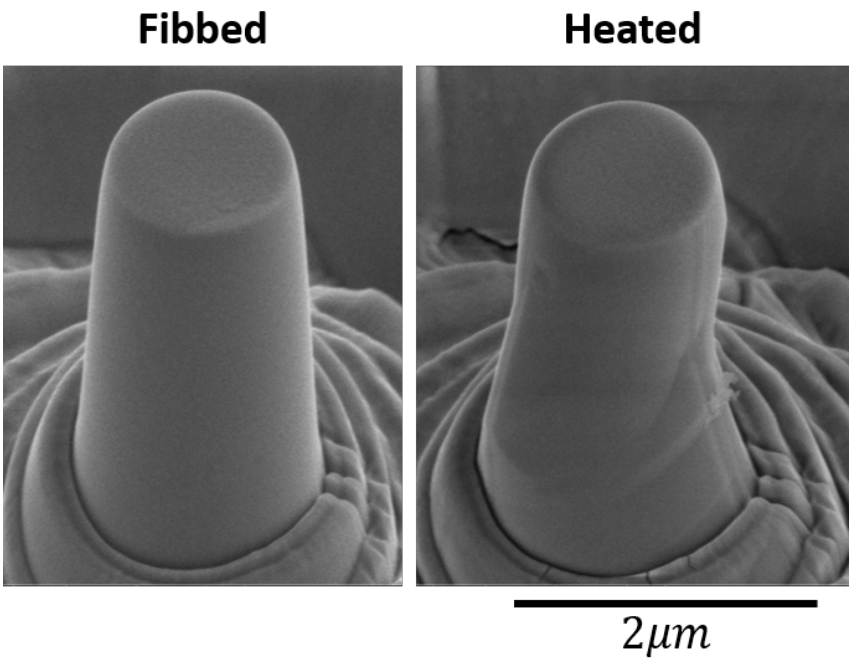

Figure 2.21: Undeformed pillar changing shape from thermally-induced phase transformation.

SEM images, it is evident that upon yielding, the top half of the particle shears to the left, then during the later part of detwinning, the mid-section of the paricle shears to the right, with significant amount of height shrinkage.

Fig. 2.23(A-C) provides SEM images of an irregularly-shaped low hysteresis $x = 0.735$ particle at room temperature before compression by approximately 15% of the particle height, after compression, and after heating to 850 °C. To better visualize the shape recovery, the original shape of the particle is traced in black and overlaid on all three images, along with partial outlines of the particle after compression (red) and after heating (blue). These images reveal that the low hysteresis particle exhibits near complete recovery (Fig. 2.23(A-C)), while the high hysteresis particle does not (Fig. 2.23(D-F)).

As is described in Section 2.3, the particles at the three different stages are imaged at 5 different angles to reconstruct their shape in 3D. Fig. 2.24 provides the 5 viewing angle diagrams and examples of a $x = 0.735$ (minimum ΔT) particle viewed in the corresponding views at the three different stages (original, deformed, and recovered). It is evident that the particle became shorter and flatter after deformation, but regained its height after heating, yet the amount of shape change

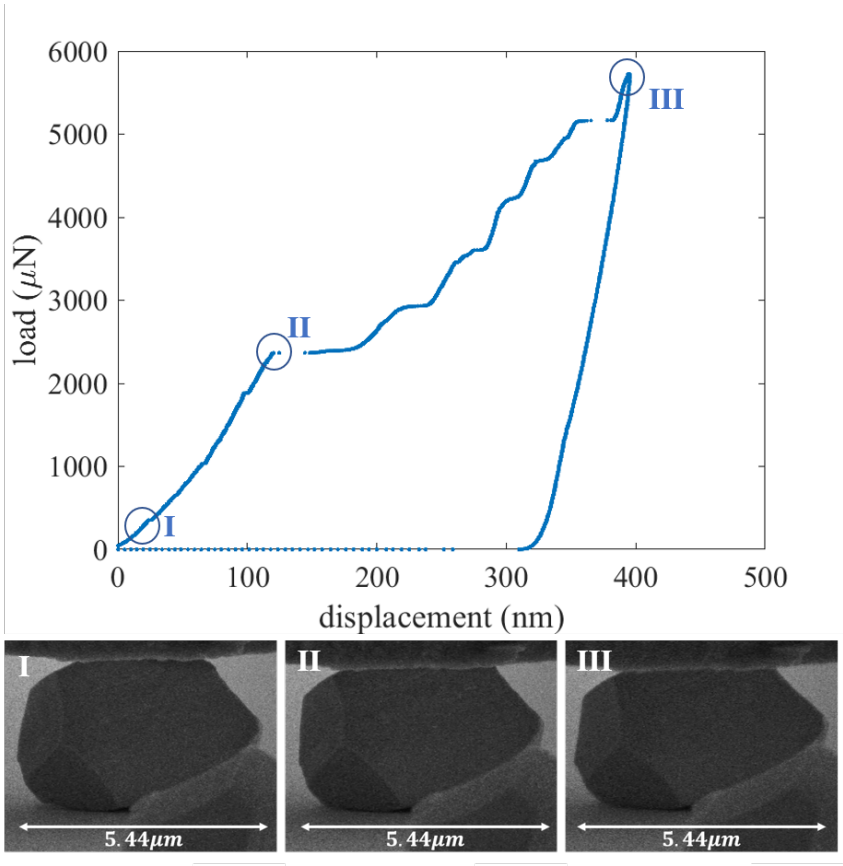

Figure 2.22: Example of *in-situ* particle deformation throught detwinning.

appears different in each view, necessitating the need to reconstruct its shape in 3D, which accounts for the full shape change.

Using images taken of the same particle from different angles, shown in Fig. 2.25(left), points on the particle were mapped to their actual position in 3d-space using simple image correlation. For each point in 3D, its coordinate in the 2D projected planes from 2 angles are taken from the corresponding images, then its coordinate in 3D can be uniquely determined given that the two viewing angles are sufficiently different (in this case 90°, see Appendix C for more details). The resulting 3D-reconstructed particle (consisting of identified sharp corners as correlated points in space) is shown in Fig. 2.25(right).

This reconstruction process is carried out for both low hysteresis and high hysteresis particles in their original, deformed / post-compression, and recovered / post-heating states. Fig. 2.26(left) shows the reconstructed low hysteresis particle post-compression (dark grey) compared to its original shape (transparent), where

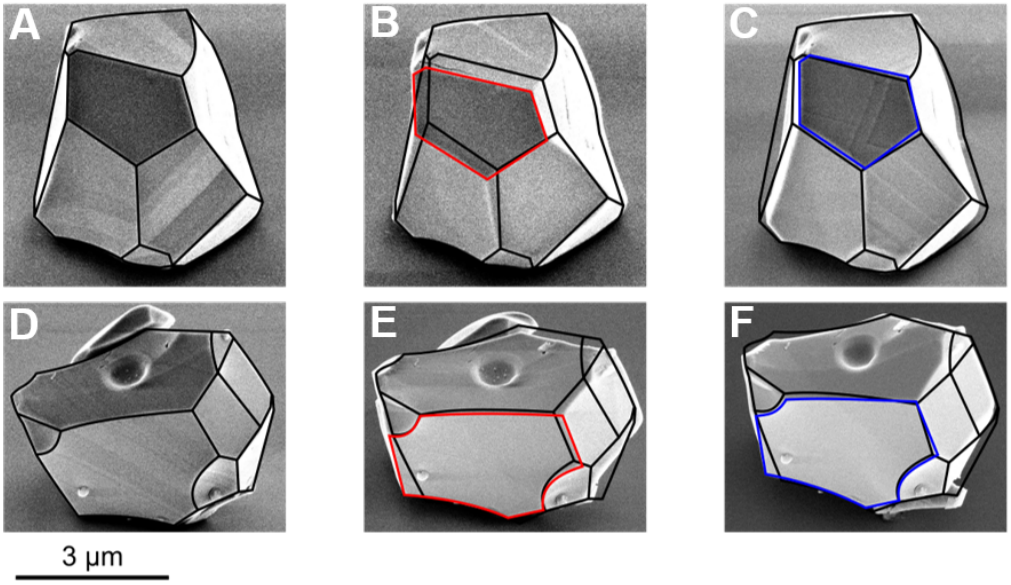

Figure 2.23: Visualization of the three states of two particles with (A-C) $x = 0.735$ (minimum ΔT) and (D-F) $x = 0.6$ (high ΔT, with the original shape mapped as the black outlines.

the particle has become shorter due to compression and expanded horizontally. Fig.2.26(right) then shows the particle after heated (dark grey) compared to its compressed state, where the particle clearly regains its height and shrinks in the lateral direction. Similarly, the high hysteresis particle becomes shorter after compression (Fig. 2.27), but does not recover to its original height after it was heated (Fig. 2.27).

We map an average deformation gradient F for each deformed state using the original particle configuration as the reference, and calculate the corresponding stretch tensor through $U = \left(F\left(F^T F\right)^{-\frac{1}{2}}\right)^T F$ [107]. We defined the recovery of a particle as

$$r = \frac{|U_{comp} - U_{heat}|}{|U_{comp} - I|} \tag{2.1}$$

and found it to be 94.5±5.9% (N = 5) for low-hysteresis particles and 62.3±13.3% (N = 3) for the high-hysteresis particles, proving that the low-hysteresis system exhibits a nearly complete shape recovery through the shape-memory effect.

2.5 Summary

We demonstrated that the theory of crystallographic compatibility provides an effective strategy to guide compositional changes for the discovery of reversible shape memory in ceramics. Crystallographic characterization through diffraction methods

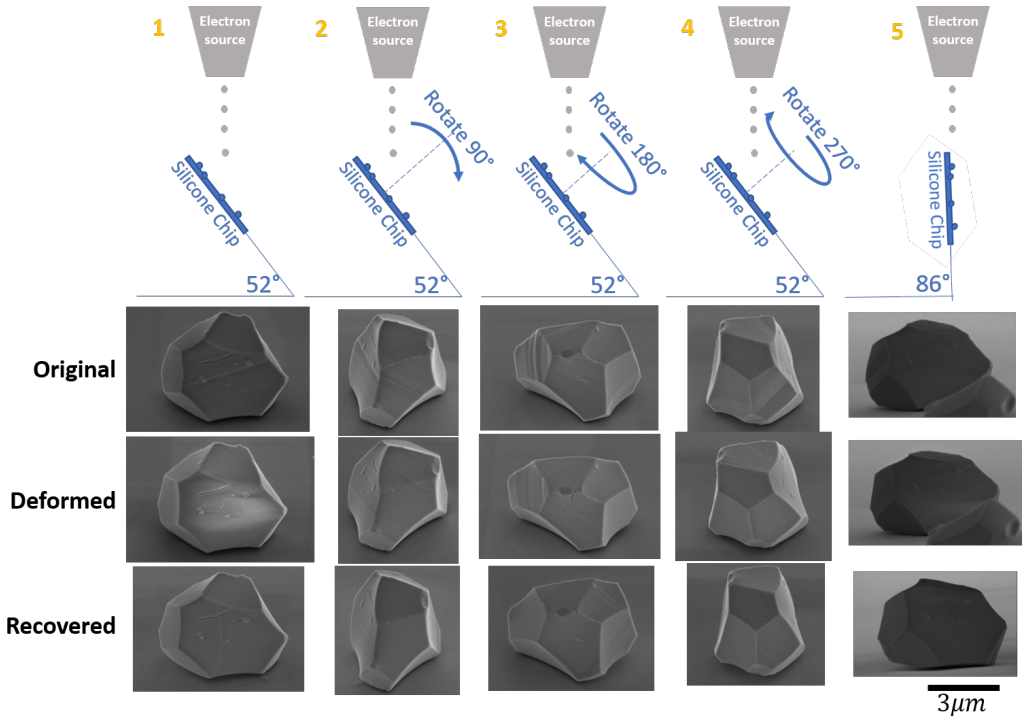

Figure 2.24: Diagrams and examples of a particle imaged from the 5 different views used for 3D shape reconstruction.

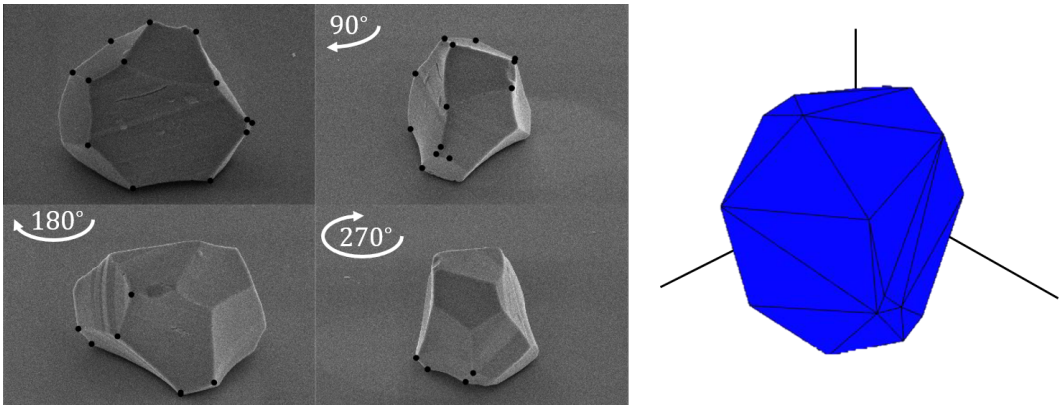

Figure 2.25: 3D shape reconstruction using points from 2D images of the same particle at different angles.

reveal orientation and compositional dependence of phase separation in Zirconia-based polycrystalline ceramics, with a predicted highest compatibility in $x = 0.735$ samples. We performed nanomechanical experiments on site-specific, small-scale ceramic samples with predicted optimal composition to reveal the shape memory effect. This comprehensive suite of theory, synthesis, in-situ nanomechanical experiments, and microstructure analysis uncovered a new, unique class of potential

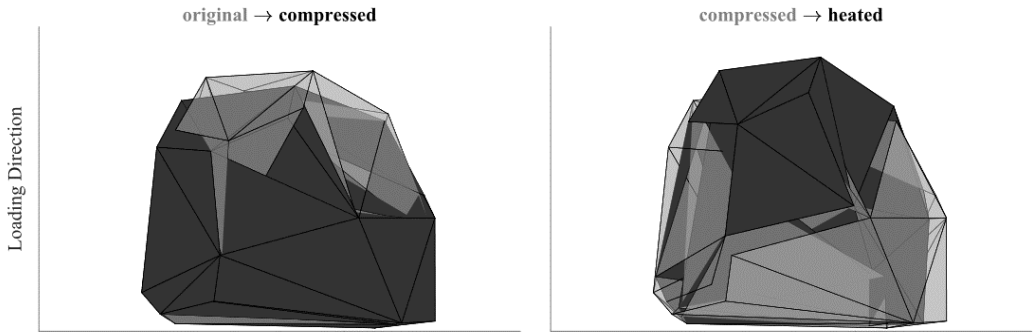

Figure 2.26: Shape memory recovery of a $x = 0.735$ (low ΔT/high hysteresis) particle.

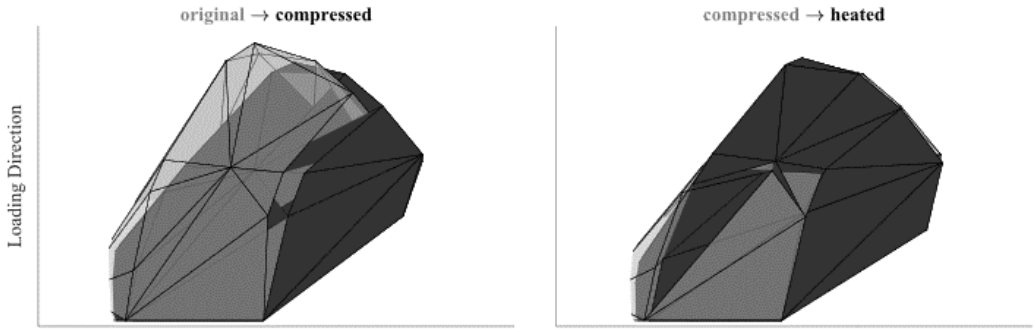

Figure 2.27: Shape memory recovery of a $x = 0.6$ (high ΔT/low hysteresis) particle.

shape-memory oxides. These new materials could provide major breakthroughs in vibration isolation and mitigation, deployable structures, and structural materials subjected to extreme thermomechanical environments. With rigid and brittle grain boundaries, potential extensions that could scale the size of these materials would include single-crystal synthesis and grain boundary engineering.

Chapter 3

SIZE EFFECT OF DEFORMATION TWINNING IN BRITTLE SOLIDS

Zhang, Haolu, Justin Jetter, Hanlin Gu, Richard D. James, Eckhard Quandt, and Julia R. Greer (2021). "Size-dependence of zirconia-based ceramics via deformaton twinning." In: *Extreme Mechanics Letters* 42, p. 101124. DOI: 10.1016/j.eml.2020.101124.

Chapter 2 demonstrates the deformation twinning enabled pseudoplastic strain of >5% in $(ZrHfO_4)_x(YTaO_4)_{1-x}$ SM ceramics. Contrary to the dislocation-driven 'smaller-is-stronger' size-effect in nanocrystals, the size-dependence of strength in deformation twinning, another carrier of plasticity, remains unknown. We use diffraction methods, microstructure analysis, and in-situ nanomechanical experiments to uncover contributing factors to the competition between twinning and slip in these submicron-sized ionic crystals, revealing power-law scaling of strength with size for both mechanisms. The slip power-law exponent of -0.57 is comparable to that of face-centered cubic (fcc) metals; the twinning size-dependence is more significant and follows a superimposed power-law with an exponent of -1. These findings unveil the universality of the superimposed power-law size-effect for twinning in single-crystals and provide new insights on deformability of ceramics and microstructure-driven nano-plasticity.

3.1 Introduction: Size-Effect of Dislocation-Governed Plasticity

Permanent deformation of single-crystalline materials, like metals and ceramics, can occur via two distinct plasticity carriers at room temperature: dislocation slip and deformation twinning. Over the past decade, the well-established power-law scaling of yield point with crystal size, with a universal exponent of -0.6 in fcc metals [3, 41, 108], was extended to metals with lower symmetry and/or higher internal friction [42, 109], as well as to hard-brittle materials such as ionic [43] or covalent crystals [44], where the power-law coefficient was suppressed to under -0.3. An inverse correlation between power-law exponent and internal lattice friction in bcc metals at room temperature has been reported in [27, 110], prompting a new superimposed power-law function for the yield-point size-dependence, $\tau_c = a^{-1} + \tau_0$, where τ_c

is the critical shear stress, a is the normalized sample size, and τ_0 is the size-independent bulk yield strength that depends purely on internal lattice friction and initial dislocation density [43]. Unlike the varying exponents in numerous reported power-law scaling for different single-crystals, the proposed inverse relation with a fixed exponent of -1 allows for a concrete physical interpretation under, for example, the Matthews-Blakeslee critical thickness model [111]. Such models break down at larger sample sizes, where plasticity shifts into a dislocation-interaction-dominated regime, giving rise to strengthening mechanisms, i.e., Taylor hardening [45, 71, 112]. The limited size range in which these models can be probed has become a pervasive roadblock to an unambiguous observation of the -1 exponent in single-crystalline plasticity [56].

The superimposed power-law with the exponent of -1 was first experimentally observed in the size-dependent critical stress for deformation twinning in single-crystalline Ti nanopillars [113], where it was attributed to a different physical origin – the probability of finding a dislocation orthogonal to the primary twin plane inversely scaling with its area. Deformation twinning, as was theorized and observed [114, 115], is nucleated by a leading partial dislocation and a trailing one on a separate atomic plane, creating an extended stacking fault that becomes the initial stage of a twin band. As a result, twinning is commonly found in metals with low stacking fault energies [10, 116, 117] and in crystals with low symmetry [118, 119], caused by the lack of accessible crystallographic planes for dislocation slip. With the twinning partials' glide restricted to parallel planes, the common mechanisms for Taylor hardening, i.e. dislocation entanglements, pinning, and multiplication [45], do not easily affect deformation twinning, making it an ideal mechanism for studying the fundamental origins of the mysterious "smaller-is-stronger" phenomenon. To probe the universality of the -1 power-law exponent, it is necessary to study deformation twinning in hard brittle crystals, for example Monoclinic zirconia, a common ionic ceramic that produces coherent twin domains upon phase-transformation [91, 92] and can be adapted in composition to undergo stress-induced twinning at room temperature [90].

In this chapter, we focus on the plastic deformation of Monoclinic $(ZrHfO_4)_x(YTaO_4)_{1-x}$ with $x = 0.735$, which was theoretically and experimentally found to produce the largest twinning-induced plastic strain and the smallest thermal transformation hysteresis [35, 90]. We uncover the twinning mechanism via site-specific systematic nanomechanical experiments and microstructural analysis, identify the conditions

under which twinning is preferred over ordinary dislocation slip, and probe the overall size-dependence of the stress required for the nucleation of twinning. We discuss these findings in the framework of nano-plasticity in single-crystals to identify the physical origin of the extrinsic size-effect in deformation twinning.

3.2 Plastic Deformation in $(ZrHfO_4)_x(YTaO_4)_{1-x}$

Oxide ceramics are known for their brittleness at room temperature, often not withstanding 0.2% strain before fracturing and failing. As was demonstrated in section 2.4, the unique microstructure in our zirconia-based ceramics enables deformation to unprecedented plastic strain at room temperature at the microscale. Here, we dive down deeper into the mechanisms contributing to plastic deformation and its implications for dislocation-based plasticity in crystalline materials in general. The experimental process is the same as in section 2.3. Composition is $x = 0.735$ unless stated otherwise.

3.2.1 Deformation mechanism

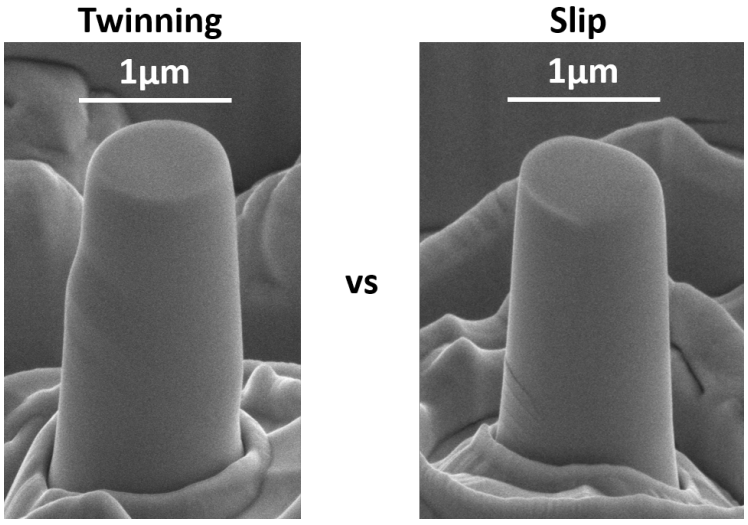

Figure 3.1: Twinning vs. slip as seen in post-compression pillar images.

As was described in section 2.2, the coherent mirror planes seen in the Monoclinic phase (stable phase at room temperature) in these ceramics provide easily accessible deformation twinning systems of $\{100\}\langle001\rangle$, $\{010\}\langle001\rangle$, and $\{110\}\langle001\rangle$. However, twinning was not the only deformation mechanism at submicron scales. As the size of the crystals decreases, the total amount of stored elastic energy decreases,

making way for dislocation slip governed plasticity before there is enough energy to create new surfaces, which initiates brittle failure. Under certain conditions that will be described below, pillars deform via twinning or slip, while fracture happens exclusively in pillars above $2\mu m$ in diameter after deformed to $> 3\%$ strain (pertaining some level of plastic deformation first). Post-compression images were used to identify twinning agains slip, examples of which are shown in Fig. 3.1 for two pillars of silimar size. As made evident by the images, twinning manifests as shearing of entire regions of the pillar in prism-like segments, while slip is identified through parallel surface offsets that fall along the glide planes [3].

3.2.2 Microstructure analysis for deformation twinning

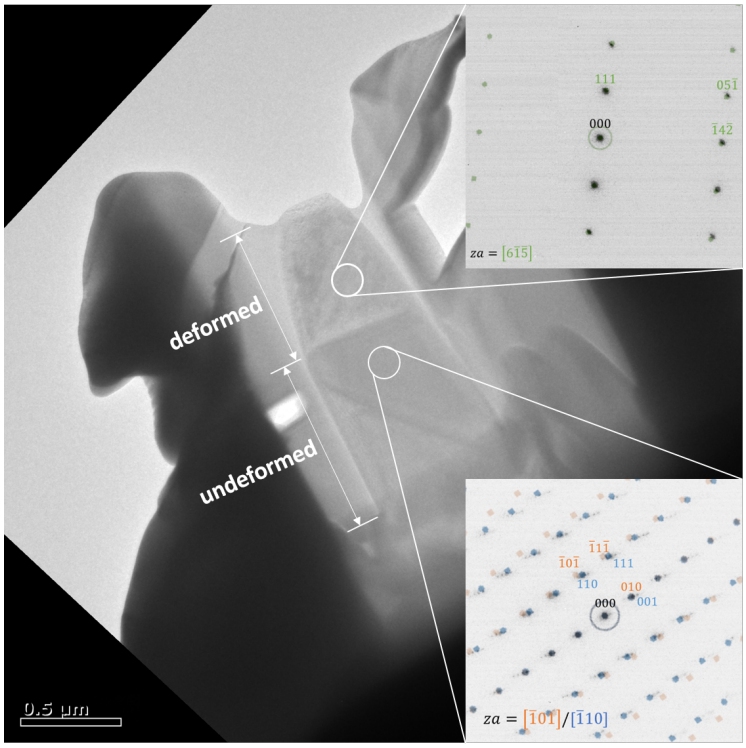

Figure 3.2: TEM image of a sliced pillar post twinning-induced plastic deformation.

Deformation twinning was visualized through TEM imaging. A deformed pillar was thinned to ~80nm thick using FIB and visualized under TEM (Fig 3.2). The pillar originally contained orientations with [101]/[110] along the loading axis. The lower part of the pillar remains undeformed, where a twin boundary cuts through diagonally. The upper half of the pillar deforms via twinning, shearing out of plane (which is why it appears to grow narrower at the top — result of the top-down

FIBbing process). The corresponding DP shows the indexed theoretical pattern overlaid on top. The theoretical angle between the zone axis $[6\bar{1}\bar{5}]$ and $[\bar{1}01]$, 8.1°, matches that was measured post-compression.

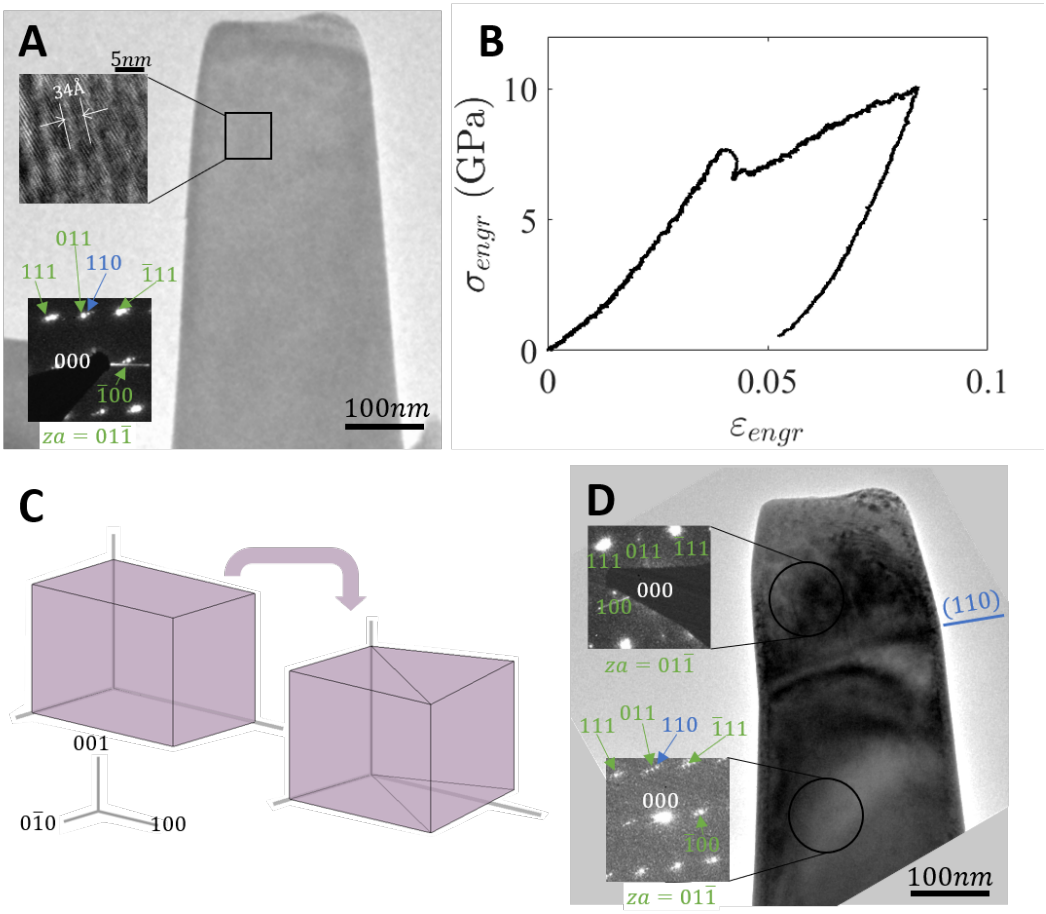

Figure 3.3: TEM images of the pillar before and after compression with its measured mechanical response and twinning mechanism.

To better characterize the microstructural change after twinning, a FIB-milled 200nm-wide, 100nm-thick nanopillar was imaged through TEM both before and after in-situ SEM uniaxial compression. Fig. 3.3A conveys the TEM image of the single-crystalline pillar as fabricated, along with a high-resolution image (upper-left inset) that contains 34-spaced Moiré fringes which arise from stacking of two orientations identified in the diffraction pattern (DP, lower-left inset): one orientation along the $[01\bar{1}]$ zone axis (green) and the other oriented favorably only for diffraction from (110) planes, resulting in the additional (110) dot (blue). The (110) planes on top of the existing $[01\bar{1}]$ pattern produce satellite peaks whose intensity is sufficiently visible only in the vicinity of the diffraction spots [120], resulting in the

triplet-like DP. The theoretical diffraction difference between the green (111) and blue (110) spots matches the predicted 0.029^{-1} from the measured Moiré spacing. The pillar was then uniaxially compressed in the SEM, with the engineering stress-strain data shown in Fig. 3.3B, revealing elastic loading up to 3.5% strain, followed by a sudden 10% stress drop after onset of deformation twinning at $\sigma_c = 8GPa$. The pillar then steadily hardens with a $\sim 75GPa$ slope while the twin plane migrates downwards at increasing cross-sectional area to 8% engineering strain with 5% plastic strain. A crystallographic diagram of the twinning system is presented in Fig. 3.3, where the Monoclinic unit cell shears along the (110) plane in the [001] direction. Fig. 3.3D shows the post-compression TEM image, where the top portion of the pillar has undergone coherent shearing, a signature of deformation twinning [10, 113]. This twinning-induced reorientation eliminates the Moiré pattern, leaving solely the $[01\bar{1}]$ DP (upper-left inset), while the lower undeformed section contains the original crystal orientations with the Moiré character. The disappearance of (110) spots and the observed (110) twin plane confirms the $(110)[001]$ twinning system.

3.2.3 Competition between slip and twinning

Main factors contributing to the competition between slip and twinning are sample size, crystal orientation, and composition.

Size: Cylindrical pillars with diameters ranging from 200nm to 2μm of different orientations as identified from EBSD were compressed. Fig. 3.4A shows representative uniaxial compression stress-strain data for pillars with roughly $[101]/[\bar{1}01]/[011]$ orientations along the loading direction, corrected for substrate effects using image correlation as described in section 2.4. The exact loading orientations for each pillar are presented in the IPF (Fig. 3.4A, inset). Twinning was found to be the preferred deformation mechanism in this orientation, with five out of seven 200nm diameter pillars and all eleven larger pillars deforming via twinning and only two 200nm pillars deforming via slip. The response of four typical pillars of different sizes that deformed via twinning is plotted in purple in Figure 2A. After the initial linear-elastic region, plasticity is triggered at a critical stress σ_c that decreases with size, followed by steady serrated plastic flow, which is a typical trait of deformation twinning [100, 121]. While the flow stress stays stable for the two larger pillars, the two smaller pillars exhibit strain hardening as a result of the fabrication induced tapering (more details in section 3.3). All sub-micron pillars deformed to >4%

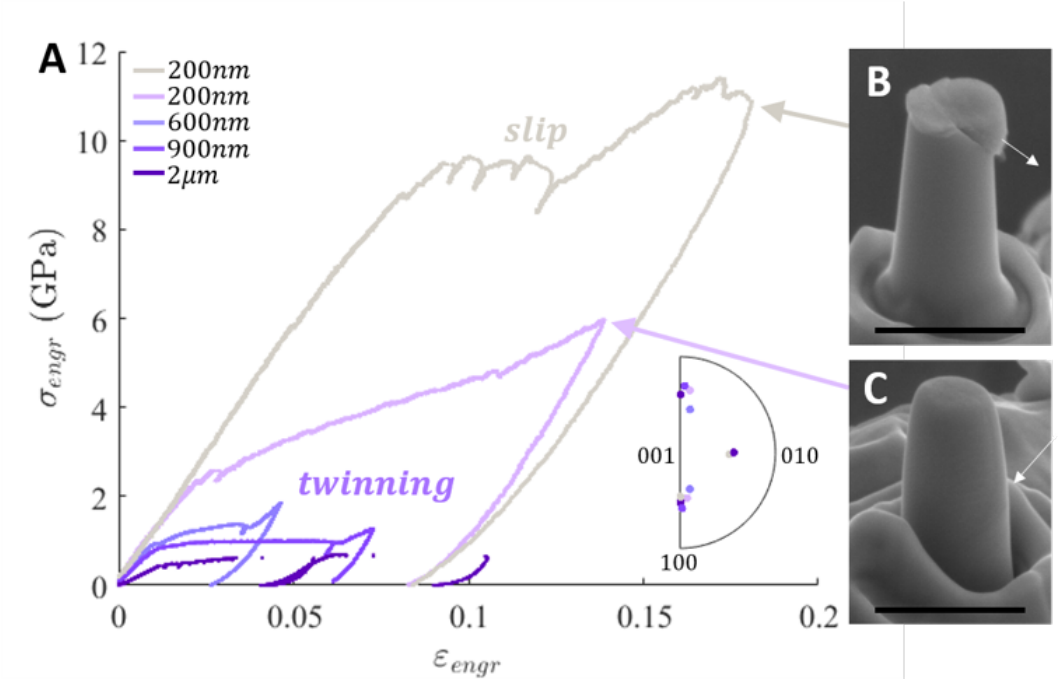

Figure 3.4: Mechanical response of different size pillars with $x = 0.735$ and similar orientation.

engineering strain without catastrophic failure, with the 200nm pillar compressing to 13% and retaining 8% plastic strain post-unloading, which is on par with that seen in ductile metals [113, 114, 121]. Twinning without fracture was also found in samples up to $\sim 5\mu$ m in size of non-standard shape (see Section 2.4). The mechanical response of a 200nm pillar that deformed via dislocation slip (grey) yields at a strain of 8% and a 4x higher stress, with subsequent stochastic strain bursts that are a signature of slip dislocation avalanches [41, 100]. As the pillar size decreases to the average twin width of 200nm, the probability of it not containing a suitable orientation for twinning increases, in which case the pillar yields only when it reaches the much higher required stress for slip. Post-compression images of the 200nm pillars that deformed via slip (Fig. 3.4B) exhibit shear offsets that are characteristic of dislocation slip at the nanoscale [3] with the slip direction marked by the white arrow. Samples that twinned (Fig. 3.4C) undergo a reorientation-induced shear, with the white arrow marking the twin direction.

Orientation: Despite twinning being the preferred plasticity carrier in (ZrHfO4)0.735, it is possible to trigger the $\{111\}\langle 011\rangle$ dislocation glide system in large pillars by aligning the loading direction to the twinning direction [001], which results in negligible resolved shear stress on all three twin planes. Mechanical response of three

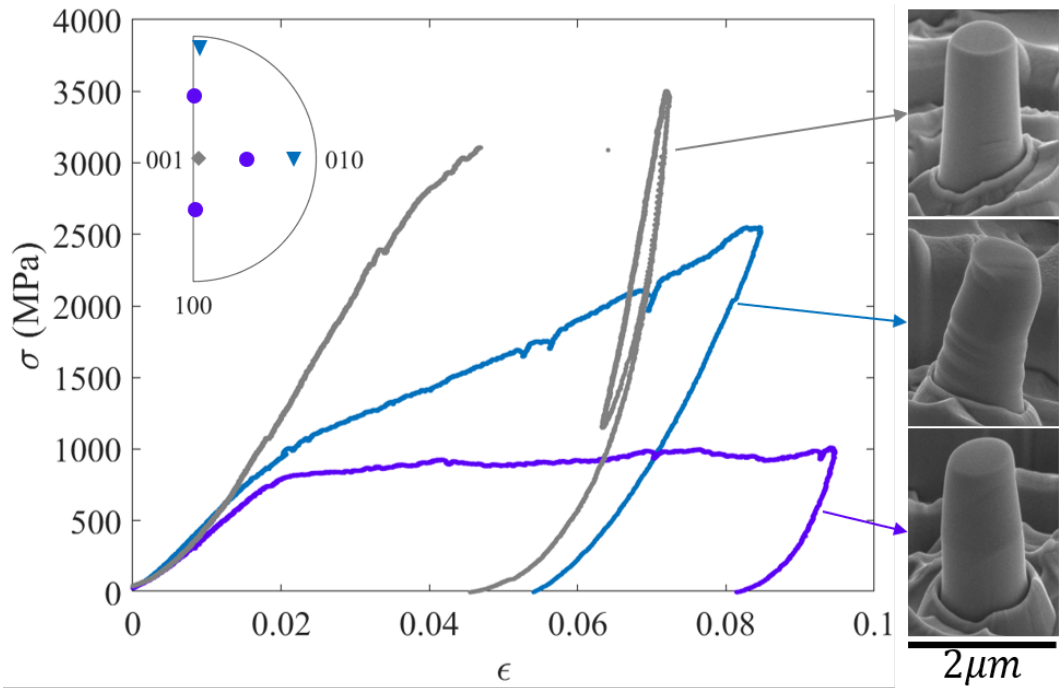

Figure 3.5: Slip triggered by aligning the [001] axis to the loading direction while other orientations deform via deformation twinning.

900nm pillars of different orientations are shown in Fig. 3.5. While both puple and blue yield at $\sim 900MPa$ due to twinning (as is evident through the post compression images, the blue orientation undergoes hardening that is almost negligible in the purple orientation as a result of the more refined twin domain microstructure, where the propagating twin encounters obstacles continuously throughout the deformation process. On the contrary, plasticity in the grey orientation is triggered through ordinary dislocation slip (slip lines on the post-compression image and the sudden strain burst in the stress-strain data).

Composition: Comparing the stress-strain response of the same set of pillar sizes for $x = 0.735$ and $x = 0.6$ with similar orientations ($[101]/[\bar{1}01]/[011]$), evidently the stress range and hardening behavior are very similar. While there is not much difference between the two 200nm pillars, the larger pillars demonstrate slip-governed plasticity at a much smaller strain in $x = 0.6$ samples than in $x = 0.735$ samples, as a result of their higher pre-existing defect density.

Apart from the drift and the Sneddon effect (elastic indentation into the substrate), another factor that skews measured displacement is the irreversible plastic deformation in the substrate below the pillar. This cannot be accounted for unless image

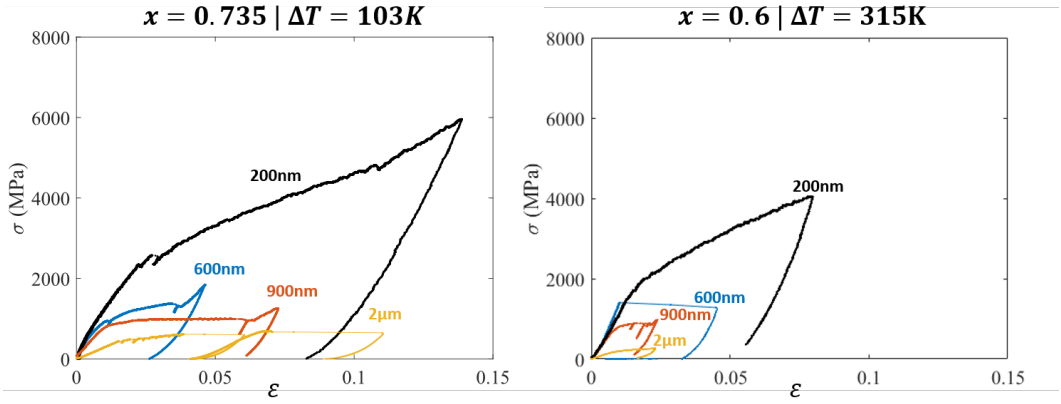

Figure 3.6: Similar mechanical response in different compositions.

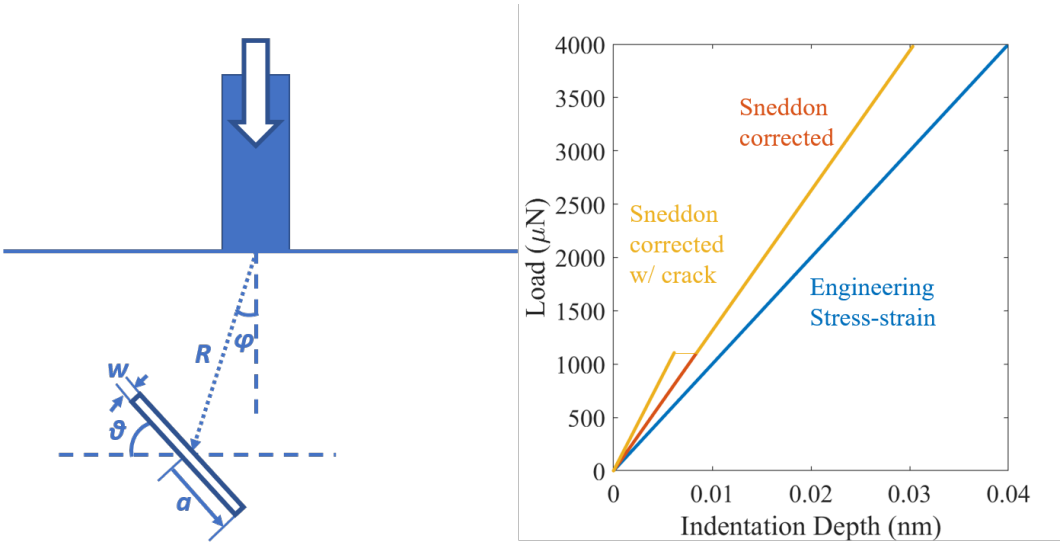

Figure 3.7: Similar mechanical response in different compositions.

correlation is done using videos containing the top and bottom of the pillars, which is often inaccessible, leading to different elastic slopes in the loading regime for different tests. To verify that this hypothesis is valid, we evaluated a theoretical model where a crack is located in the substrate below a pillar that is being compressed (Fig. 3.7(left)). Assuming a Boussinesq stress distribition in the substrate [122], the elastic loading of the pillar — both before and after the crack closes — is calculated and compared to that on a rigid substrate (engineering) and simple dense substrate (Sneddon corrected), which is shown in Fig. 3.7(right). The load is calculated by integrating the Boussinesq stress field on the sphere surface containing the crack, where the crack area is excluded (before the crack is closed) and then included (after the crack closes, which collapses onto the Sneddon corrected solution). The

criterion for crack closing is based on the displacement of the crack center in the direction orthogonal to the crack plane reaching the width w of the crack. It is clear that before the crack closes, the elastic strain coming from a 400nm diamater crack can result in a larger than two-fold difference from the nominal engineering stress-strain, therefore explaining the large discrepancies between the different pillars in Fig. 3.4 - 3.6.

3.3 Yield Point Size Dependence

As was seen qualitatively in section 3.2, sample size (pillar diameter) significant influences material behavior during plastic deformation, including yield point for slip / twinning and subsequent hardening behavior.

3.3.1 Orientation dependent size-effect

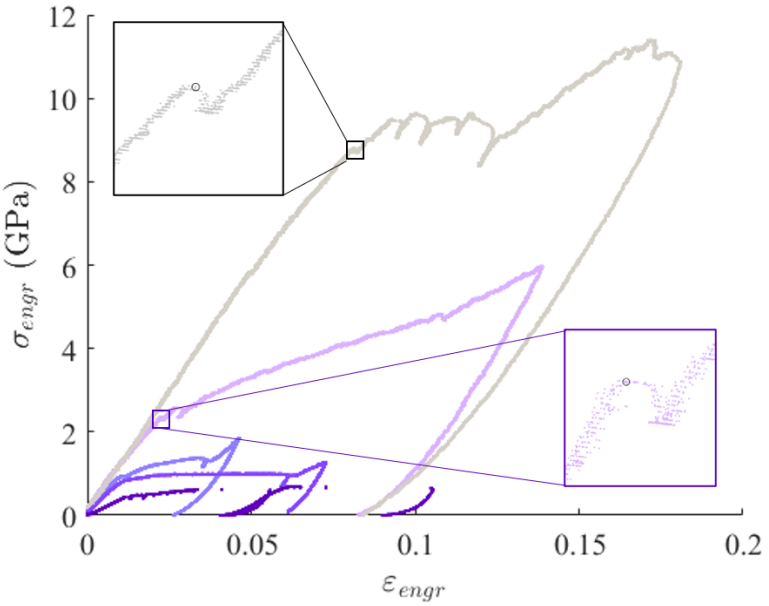

Figure 3.8: Yield stress (slip) and critical stress (twinning) defined as the maximum before the first stress drop.

Quantitative analysis on the critical stress for yielding reveals the yield point for each orientation decreasing with increasing pillar diameter (Fig. 3.9(left), the lines are there to guide the eye — detailed discussions are in Section 3.4). We defined the yield point — for slip or twinning — as the local maximum before the first stress drop as a result of the nanomechanical setup, as is demonstrated in Fig. 3.8 [3, 5,

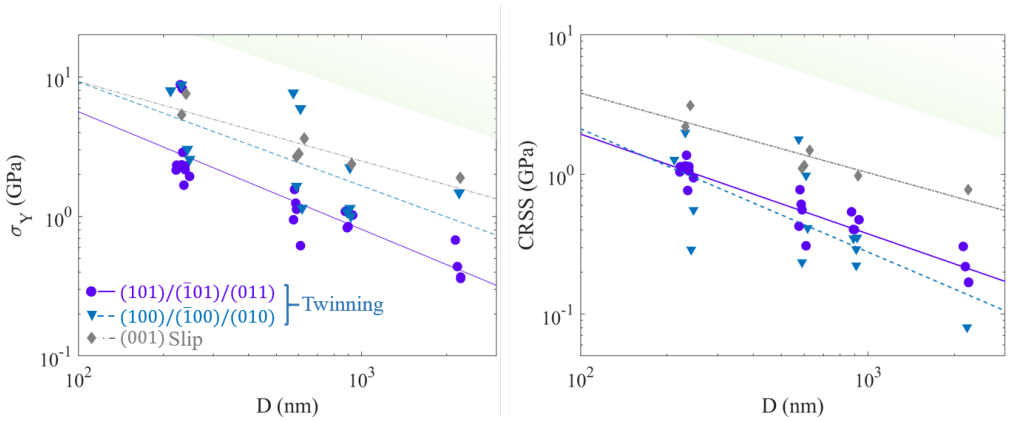

Figure 3.9: Yield point size dependence for three sets of orientations.

27, 41]. It is immediately evident that the slip size-effect follows that of fcc metals (green gradient at the upper-right corners), while the size effect for twinning in both orientations are much more significant. Between the two twinning orientations, the purple/circle set of pillars' yield points are more repeatable - with the blue/triangle set of pillars' glide planes almost perpendicular to the loading direction, any small misalignment in the loading axis results in a large discrepancy in the measured yield stress. On average, the blue/triangle orientations have significantly higher yield points than the purple/circle set of pillars as a result of their less ideal loading orientation.

$$CRSS = \sigma_c s = \sigma_c(\boldsymbol{n}_{load} \cdot \hat{\boldsymbol{n}}_{twin})(\boldsymbol{n}_{load} \cdot \boldsymbol{\lambda}_{twin}) \tag{3.1}$$

We investigated the critical resolved shear stress (CRSS) for critical dislocation activity, calculated using Eq. 3.1, as a function of the effective pillar diameter. Here, s is the maximum Schmid factor among combinations of pillar orientations and accessible twin/slip systems; $\boldsymbol{n}_{load}$ is the loading direction, $\hat{\boldsymbol{n}}_{twin}$ is the twin/slip plane normal, and $\boldsymbol{\lambda}_{twin}$ is the twin/slip direction. The two twinning orientations collapse onto the same scale once we account for the different Schmid factors, further confirming the twin systems, while the slip yield stress remains higher and less size-dependent. Further discussion can be found in section 3.4.

3.3.2 Composition indifference

Since composition is found to affect pseudoplastic strain rather than initiation of deformation twinning, the initially twinning critical (yield) stress follows the same

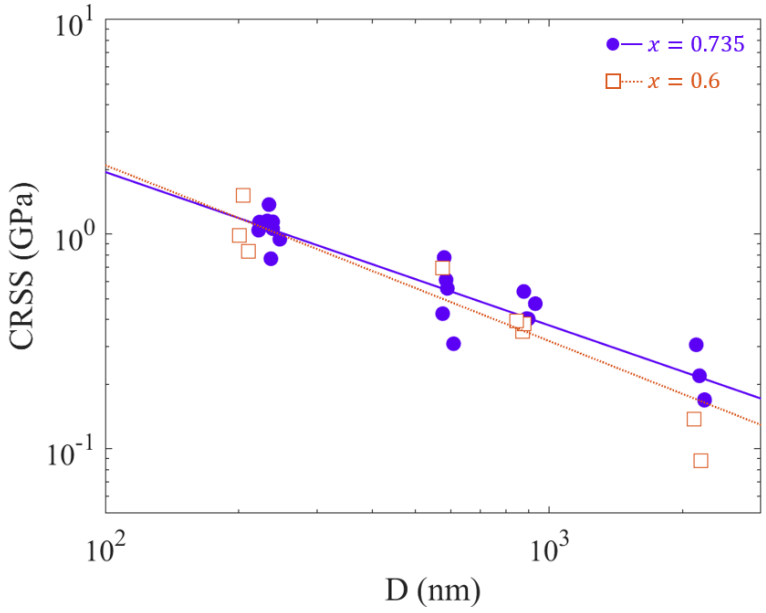

Figure 3.10: Size effect of twinning critical stress is independent of material composition or compatibility.

size dependence scaling in $x = 0.735$ and $x = 0.6$ samples with the same orientations $[101]/[\bar{1}01]/[011]$ (Fig. 3.10). Since the two compositions contain the same crystal structure and twin microstructure but with different defect density, this confirms the hypothesis that the initiation of twinning-induced plasticity is not dependent on the type of density in existing ordinary dislocations.

3.3.3 Hardening

As was briefly mentioned in section 3.2, hardening becomes prevalent in the twinning process of smaller pillars. Close examination reveals power-law-like size effect on the hardening slop (fitted to the post-yield region of loading), shown in Fig. 3.11. At smaller scales, the lack of mobile dislocations give rise to increased stress to initiate glide after each source is depleted, which partially explains the size effect of hardening in both slip and twinning. Another source of hardening, which affects twinning more than slip, is that as the diameter decreases, the ratio of pillar side tapering to diameter increases, hence as a twin plane propagates down the pillar, the amount of force needed increases at higher rates for smaller pillars.

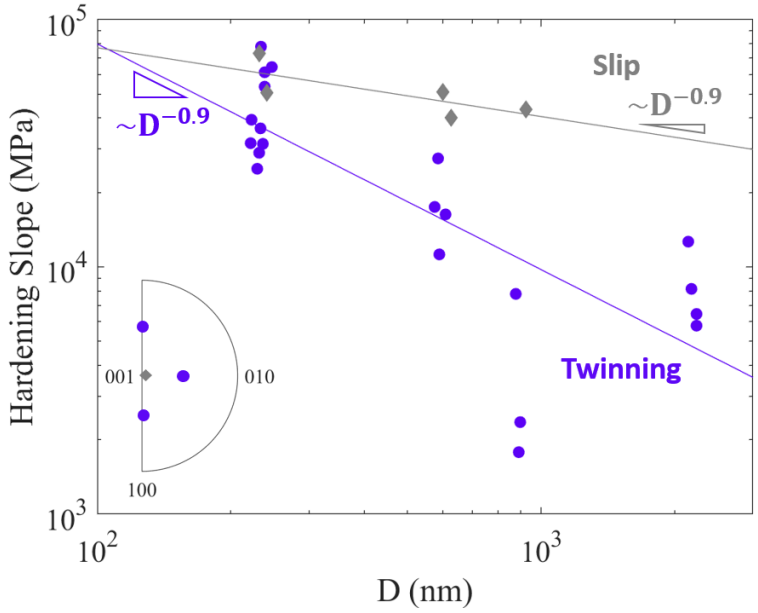

Figure 3.11: Hardening slope increases with decreasing pillar size.

3.4 Universality of the 'Smaller-is-Stronger' Size Effect for Twinning and Slip

Fig. 3.12 plots normalized $CRSS$ vs. D for both twinning (purple) and slip (gray) orientations. The shear modulus, $G = 61.5GPa$, was estimated from the linear unloading segments in 200nm pillars, consistent with previous reports on Yttrium-stabilized Zirconia [38, 123]. For pillars of similar size, CRSS for twinning is significantly lower than that for slip, consistent with twinning being the preferred deformation mode for pillars with access to both. Adopting the well-established pure power-law of

$$CRSS \propto D^{-\alpha}, \tag{3.2}$$

the twinning size-effect, found to be universal among different orientations and compositions (Fig. 3.9 and Fig. 3.10), has a higher exponent $\alpha_{twin} = 0.74$ than $\alpha_{slip} = 0.57$. Fig. 3.12(A) also contains power-law scaling reported for other brittle materials (dashed lines), most of which exhibit a suppressed exponent of < 0.3, commonly attributed to their high intrinsic lattice resistance [24, 25, 124, 125]. All dashed lines in Fig. 3.12(A) correspond to slip or fracture; this work presents the first known systematic size-effect for twinning in a non-metallic material. A ceramic whose size-effect comes closest to that for slip in $(ZrHfO_4)_{0.735}$ is MgO with activated $\{110\}\langle 110\rangle$ slip and exponent $\alpha = 0.6$ [43], similar to that in fcc metals [27]. The scaling for twinning in this work is significantly more prominent.

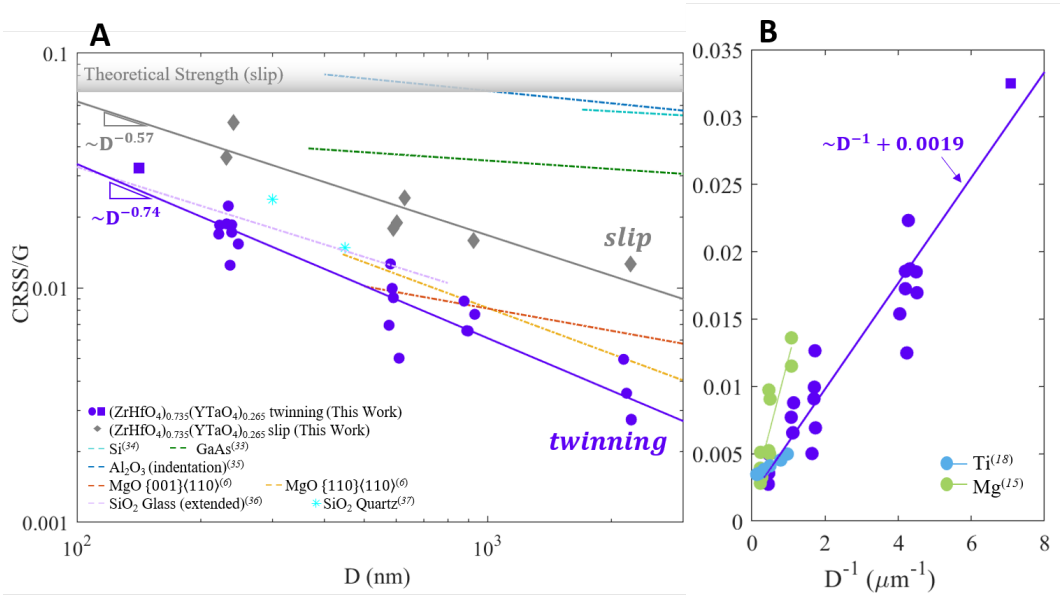

Figure 3.12: Universality of size-effect on normalized CRSS through deformation twinning.

This large increase of size-dependence from slip to twinning finds its equivalence in metals, where a similar exponent of $\alpha = 0.7$ was discovered for twinning in Mg [121], and an unprecedented $\alpha = 1$ was found for Ti [113]. Fig. 3.12(A) also plots two experimental data points for deformation twinning in quartz [126] (teal stars), where a similar size-effect begins to emerge, although no conclusion was drawn due to the small span in size.

The physical basis for the extrinsic size-effect on strength remains unclear – the pure power-law fitting brings to question its validity in brittle solids [43, 56], whose high lattice resistance persists as a dominating factor on yield stress in the commonly probed size-range for nano- and micro-pillar work. Another way to represent size-effect for materials with high background stress is

$$CRSS = \xi D^{-\alpha} + \tau_0, \tag{3.3}$$

where ξ is a length-scale constant that scales with the Burgers' vector and τ_0 is the resolved macroscale yield strength. Fitting Eq. 3.3 to the twinning data for $(ZrHfO_4)_{0.735}$ gives $\alpha = 1.00 \pm 0.22$ and $\tau_0/G = 0.0019 \pm 0.0018$ (Fig. 3.12(B)), with the average α identical to that predicted by the Matthews-Blakeslee critical thickness model, which emerges as equilibrium is reached between the plastic strain and the curvature of geometrically-necessary (misfit) dislocations [112]. The fitting

process was done in Matlab using the $fit()$ function with nonlinear least squares option.

We now seek to understand the form of Eq. 3.3 and its universality for twinning in both metals and non-metals, and potentially extending to dislocation slip. The size-dependence of twinning in Ti [113] exhibits the identical form as Eq. 3.3 with -1 exponent, but was theorized as a Hall-Petch type relationship with the critical dislocation density for twinning scaling as D^2, while it defines τ_0 as having contributions from internal friction and solute strengthening, which approaches the corresponding bulk strength at the macro-limit [43, 56]. We fit previously reported Mg CRSS [121] to Eq. 3.3, only including data between $1\mu m$ and $5\mu m$ since smaller pillars plateau at theoretical strength, resulting in $\alpha = 1.00 \pm 0.38$ and bulk strength $\tau_0/G = 0.0017 \pm 0.0034$; this estimated τ_0 is close to that reported for mm-size Mg samples [127]. The uncanny similarities among the drastically different systems in Fig. 3.12(B) suggest universality of Eq. 3.3 with $\alpha = 1$ for a larger selection of materials.

For dislocation slip, the immediate caveat of the widely-accepted power-law in Eq. 3.2 – that it breaks down at the macro-limit with nonnegligible bulk strength – prompted the additional τ_0 term in Eq. 3.3 [43, 56], yet the lack of data below 100nm prevents a conclusive fit for the scaling exponent α. As was extensively discussed in [56], there exist physical models for Eq. 3.3 with $\alpha = 1$ [111], which collapses onto the same form as in Fig. 3.12(B). An example of such models is the Matthews-Blakeslee critical thickness model [112], which applies to both ordinary and twinning dislocations. In the case of ordinary dislocation slip, these idealized models begin to break down at μm-scale, where dislocation interactions come into play. Such limitations do not affect deformation twinning, making it the ideal mechanism for studying this phenomenon. We do not have enough evidence in this work to pinpoint its exact explanation, but the universality of the $\alpha = 1$ exponent suggests that deformation twinning can serve as an alternative route to investigating the fundamental origin of the mysterious 'smaller-is-stronger' crystal behavior.

3.5 Summary

Deformation twinning in single-crystals and its dependence on extrinsic dimensions has not been fully understood at the nanoscale. In this work we uncover twinning as the preferred plasticity carrier for small volume $(ZrHfO_4)_x(YTaO_4)_{1-x}$ ceramics, while dislocation slip can be activated only when no accessible orientation for twin-

ning exists. In the sub-micron range, these single-crystal oxides plastically deform up to a 10% strain through twinning without failure. While the power-law exponent for the yield-stress size-effect of slip, $\alpha_{slip} = 0.57$, is close to that in fcc metals, we reveal the first systematic strength-to-size dependence for twinning in ceramics. This significant size-effect was found to follow the inverse-like relationship with exponent $\alpha = 1$ when considering a superimposed bulk strength, identical to the twinning size-effect in soft metallic materials. The large similarities between a brittle oxide and ductile metals shed light on the universality of the superimposed scaling for the yield-point size-effect in single-crystal plasticity, suggesting deformation twinning as an alternative controllable way of probing its exact physical origin.

Chapter 4

MICROSTRUCTURE-MECHANICS RELATIONSHIP OF SCORPION PINCER CUTICLES

Zhang, Haolu, Israel Kellersztein, Rebecca A. Gallivan, H. Daniel Wagner, and Julia R. Greer (n.d.). "Microstructure enabled fracture resistance in Scorpio Maurus Palmatus cuticles." In: *In Preparation* ().

The complex hierarchical microstructure in biomaterials prevent a universal understanding of their mechanical behavior. Previous studies reveal a unique fiber organization in scorpions that is not found in their close relatives in the Arthropod family. While the uncovered Bouligand and Unidirectional structures are hypothesized to dominate the stiffness and toughness of the organ, there is still a lack of accurate constitutive depictions of the constituents or of intact microstructural characterization. We use Synchrotron X-ray diffraction to reconstruct fiber architecture and *in-situ* microscopic tension and compression with FEA to identify isolated stiffness, strength, and fracture behavior of the two different regions. The unveiled microstructure-mechanics relationship — orientation-dependent stiffness, compression-tension asymmetry, fiber-protein detachment — shed light on the optimized structural functionalities for the two regions in the scorpion cuticles.

4.1 Introduction: Damage Mitigation in Hard Biomaterials

Hard biomaterials such as bone, diatoms, nacre, etc. constitute a mechanical behavior superior to man-made materials, such as increased toughness and crack deflection [17, 21, 30, 61, 63, 128, 129], despite using simple building blocks such as chitin [130], silica [17], collagen [131], etc. With strengthening mechanisms at continuous hierarchical lengthscales, the unique behavior of these materials stems from their optimized microstructure. For example, collagen fiber bridging provides energy dissipation in fractured bones [21, 132]; the brick-and-mortar structure in nacre incorporates friction and interplate bridging [30]; unique nano-patterns on diatoms strategically deflect crack paths [17]. These evolution optimized microstructures inspire artificial composites with combined material properties significantly improved from a simple mixtures of their corresponding constituents [133–135].

One material of particular interest to the biomechanics community is chitin, a long-chain biopolymer that is a major component to arthropod exoskeletons [136]. Chitin, specifically α-chitin fibrils, combines with proteins to make nanometer-thick chitin-protein fibers that become the basic building blocks providing the structural integrity for many organisms. The unique Bouligand twist/plywood structure of chitin-protein fibers in the cuticles of crustaceans and insects have inspired a plethora of mechanical investigations on the macroscopic stiffness, strength, and toughness of the cuticles of lobsters [61, 130, 137–140], crabs [138, 141], spiders [139, 142], insects [143–145], and other arthropods [58, 146–149]. Theoretical and simulation frameworks have been developed to quantify the crack deflection and energy absorption in the twisted laminates of chitin fibers [150, 151], and bio-inspired artifical materials show improved impact resistance and shear strength [65, 152, 153]. Depite the abundance of dissected lobsters, directly measuring the mechanical properties of α-chitin remains a challenge, with extended efforts on theoretical and simulated predictions for its stiffness and strengh at the nanoscale [61] using MD, DFT, and other complicated methods.

Recent works from our collaborators in the Wagner group at the Weizmann Institute of Science reveal extra unidirectional layers that are unique to the moving fingers of two species of scorpions [154] and helicoid patterns that add an out-of-plane twist to the purely-rotational Bouligand structure [155]. While there is nanoindentation data that show anisotropy in the mechanical response of these materials, a few questions remain unanswered. 1) With a 3-dimensional microstructure inferred from fractured surfaces and the material naturally designed for guided crack paths, there is limited visual observation of hidden features in the Bouligand structures and little quantifiable information on the fiber organization. 2) While nanoindentation probes the homogenized reduced stiffness of specific regions, the deformation mechanism, strength, and inhomogeneity within the individual layers remain unknown. 3) Known for its improved fracture toughness, the Bouligand layers and their competition with the unidirectional layers can only be deciphered through controlled microscopic fracture experiments such as 3pt bending or tensile tests.

We use Synchrotron X-ray scattering to resolve the fiber orientation, distribution, and network structure in intact samples of dehydrated scorpion cuticles in different orientations. Microscale compression and tension experiments were used to characterize the microstructure-mechanics relationship, quantifying properties such as directional stiffness, large-strain deformation, strength, and fractography, in an

attempt to resolve the individual constituent behavior and how they each contribute to the overall functionality of the organism.

4.2 Microstructural Analysis

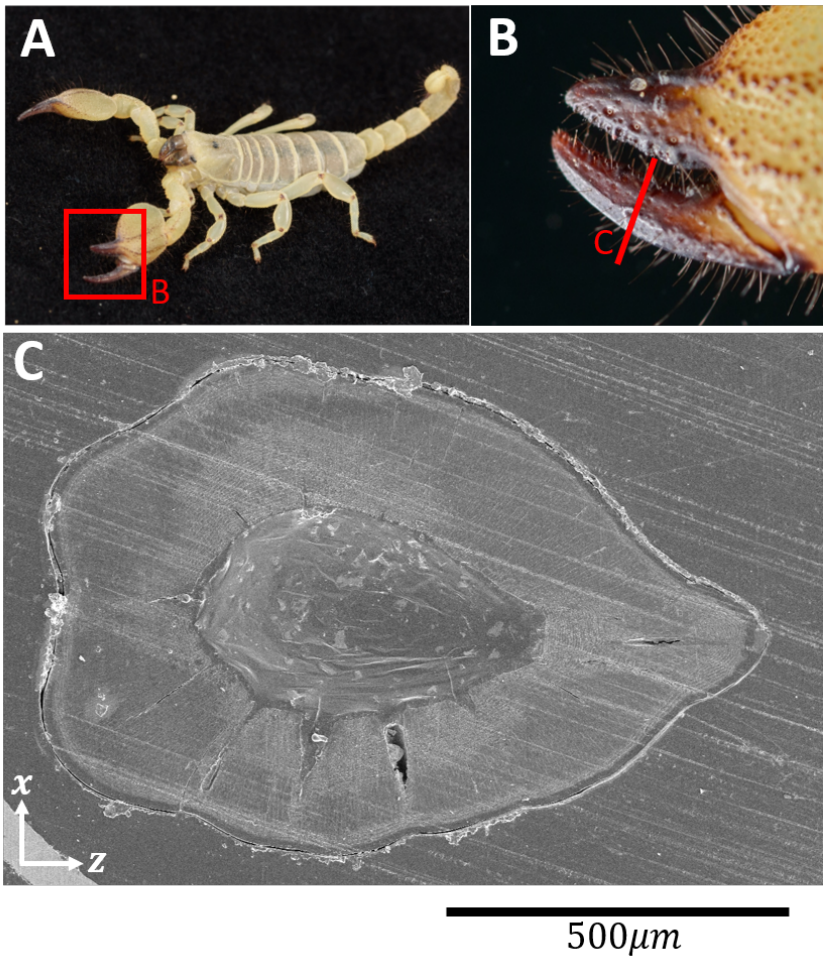

Figure 4.1: Hierarchical overview of the *Scorpio Maurus Palmatus tarsus* cuticle.

Dehydrated *tarsuses* (moving fingers) of *Scorpio Maurus Palmatus* (SP) were prepared by our collaborators from the Wagner goup at the Weizmann Institute of Science following steps in [154]. Each *tarsus* was dehydrated again using ethanol with graded concentrations up to 100%, vacuum embedded in epoxy, then polished using a Buehler Ecomet3 with graded sandpapers (240 grits up to 1200 grits, then finishing with $1\mu m$ and $0.1\mu m$ diamond suspension solutions). Overview of an SP is shown in Fig. 4.1(A), with a close up of its *tarsus* shown in Fig. 4.1(B). Fig. 4.1(C) presents a SEM transversal cross-sectional view of the tarsus, with clear sublayers

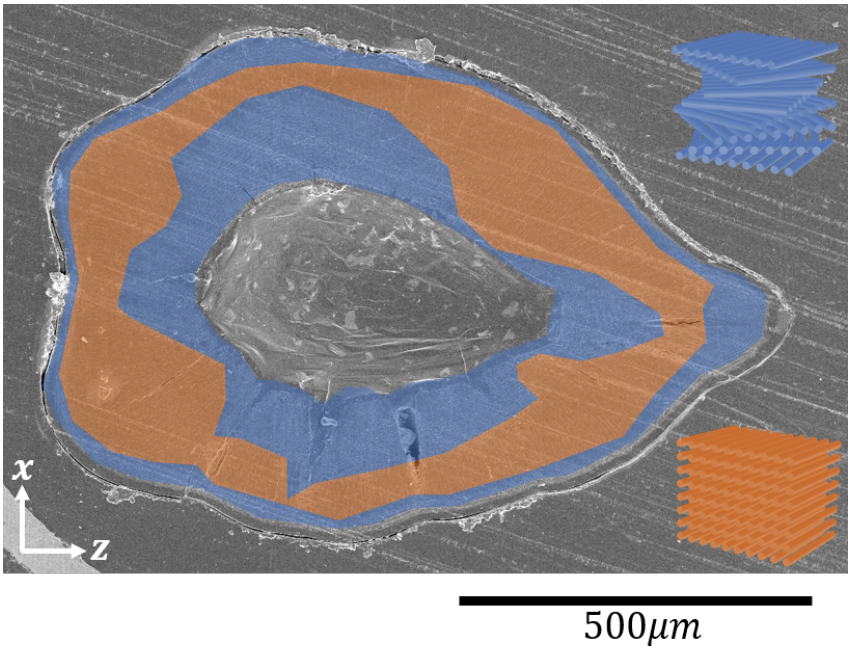

Figure 4.2: Distint microtructural regions in the *tarsus* with (orange) unidirectional fibers and (blue) Bouligand fibers.

within the shell of the cuticle. The slight contrast in the layers come from the different microsctructures, which polishes to slightly different roughness. More detailed description of the layers can be found in Ref [154]. Fig. 4.2 shows the cross-section with the Bouligand regions marked in blue and the unidirectional regions marked in orange. It is evident that the thickness of the endocuticles varies in different locations, with the thickest parts in the innermost, outermost, left, and right regions, where stress is highest when the cuticle is bent inwards or side-ways, suggesting that the competition between the Bouligand structure and the Unidirectional structure is due to their different load-bearing capabilities.

Prior studies have shown that the Bouligand structure in the SP manifests as stacked helicoid (added twist on the ordinary Bouligand structure, which is rotational in-plane) lamellae that form a thick laminate which then stacks in the orthogonal direction; the Unidirectional layers, on the other hand, consist of lamellae made of short textured fibers aligned across the lamellae, which stack in the longitudinal direction along the cuticle. Representative SEM images are shown in Fig. 4.3 [155], where textured lamellae in the two regions can be seen.

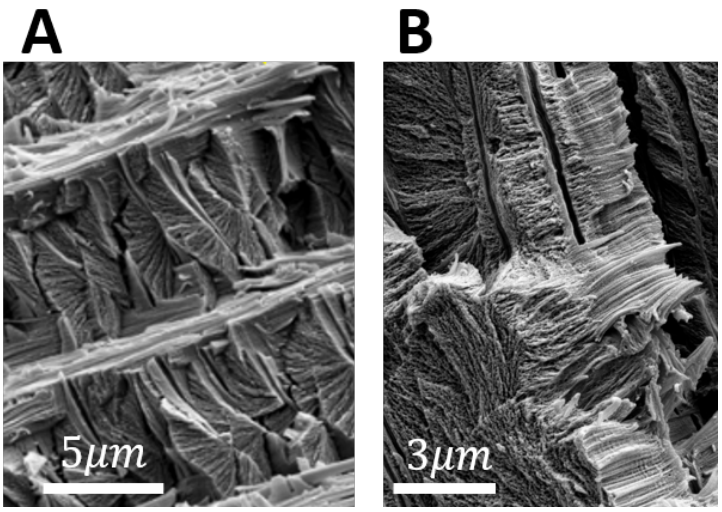

Figure 4.3: SEM images showing the microstructure in the (A) Bouligand layers and (B) Unidirectional layers.

4.2.1 Microbeam SAXS/WAXS/Fluorescence via Synchrotron X-ray Diffraction

To observe the twist angle and rotation axis of the helicoid geometry in these unique biocomposites, samples were fractured by force to create textured surfaces from which the 3-dimensional geometry of the fiber structure were interpreted [154, 155]. Due to the porosity of the material, the weak fiber-protein interface, and the ordered pore cannals, the material fractures at biased faces, revealing the same fracture surface in all reported SEM images. The structure of the fiber behind these surfaces in 3-dimensions remains mysterious. We use transmission Synchrotron X-ray Diffraction to visualize the fiber structure within the volume of these composites without physically damaging the samples. Due to the highly heterogeneous nature of the material, we used a μ-beam Small Angle X-ray Scattering (SAXS) and simultaneous Wide Angle X-ray Scattering (WAXS) at the Brookhaven National Synchrotron Light Source (NSLS-II), beamline 12-ID.

Scanning set-up

Samples of $5\mu m$ thickness were prepared by microtome and deposited onto Si_3N_4 membranes, then secured on the instrument using Kapton tape. Samples from two species, SP and *Buthus Occitanus Israelis* (BO), each of two orientations (transverse and longitudinal cross-sections) were used. Optical images of the SP samples are shown in Fig. 4.4.

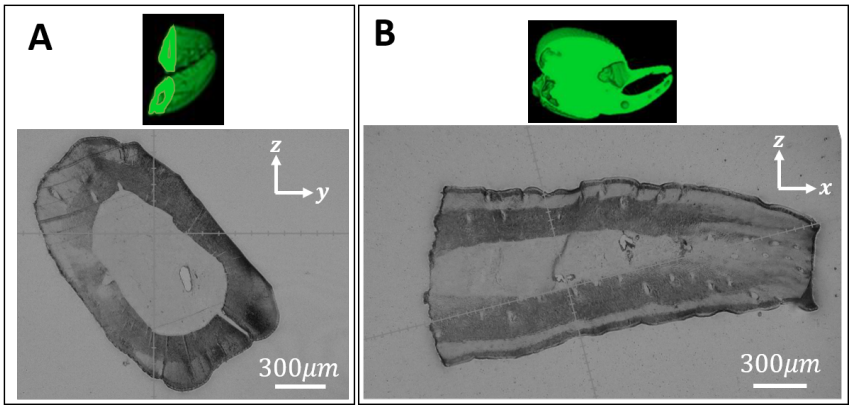

Figure 4.4: SP cuticle samples used for Synchrotron X-ray diffraction with (A) transversal cross section and (B) longitudinal cross section.

The scanning set-up is shown in Fig. 4.5, where a $2\mu m$ (vertical) by $20\mu m$ (horizontal) 16.1 keV beam is scanned across a region of the sample containing all layers of interest and the diffraction pattern as well as fluorescence signal from each pixel was recorded, with the scanning configurations shown in Fig. 4.5. Each sample was scanned at two rotations that were 90° apart to eliminate effect from the beam shape.

Fiber structure reconstructed via SAXS

The diffraction data of the Endocuticle (Bouligand) region of the SP cuticles from the two orientations are shown in Fig. 4.6. In the transverse orientation as seen in Fig. 4.6(A), the diffraction pattern varies as the beam travels across the sample: in the interlayers, which are unidirectional transitions between each Bouligand laminate, the diffraction is anisotropic since the beam only detects stacking from fibers in the one textured orientation along the hoop direction. In the middle of a laminate, the fiber stacking is averaged over the $2\mu m$ by $20\mu m$ beam to show a diffraction pattern from all stackings as a result of the rotation and twist in the helicoid geometry. The change in fiber orientation interpreted from the diffraction patterns are shown in the fiber diagrams, which match that observed from the fracture surfaces in [154, 155]. In the longitudinal direction, the stacking of the interlayers are along the beam direction, which does not diffract intensely, resulting in the same DP as seen in Fig. 4.6 throughout the Endocuticle. The interpreted fiber structure is again consistent with that seen in SEM images.

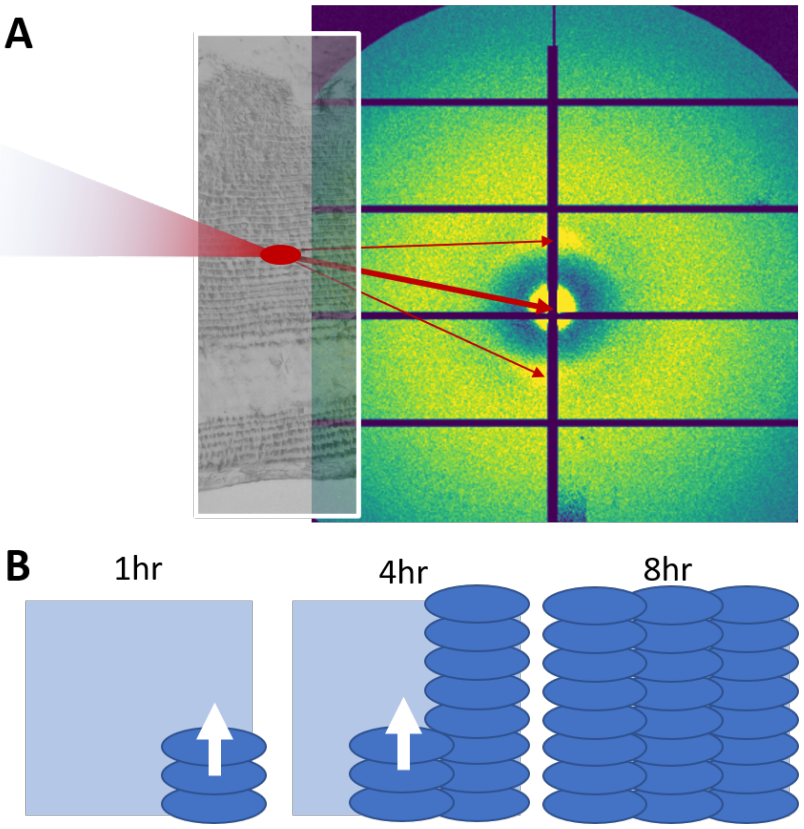

Figure 4.5: Synchrotron μ-beam X-ray SAXS/WAXS set-up.

Similarly, the diffraction data and interpreted fiber structure are shown in Fig. 4.7. The diffraction peak from the 4.69nm fiber packing (typical of α-chitin [142]) in addition to the diffuse background in the transversal orientation (Fig. 4.7(A)) suggest packing of layers of randomly spaced fibers pointing towards the beam direction, while the shape 4.69nm peaks in the longitudinal direction (Fig. 4.7(B)) confirm the evenly packed fibers along the longitudinal direction as seen in the broken samples through SEM [154, 155].

Anisotropy analysis

Further analysis on the anisotropy in the diffraction patterns was performed to visualize the inhomogeneity of fiber organization throughout the distinct layers in the samples. The Azimuthal integration (integrated intensity along the radial direction from the incident beam), an example of which is shown in Fig. 4.8(left), obtained using provided scripts from the beamline at NSLS-II, is used for the analysis. The background intensity is first subtracted from the data, then a Gaussian/normal

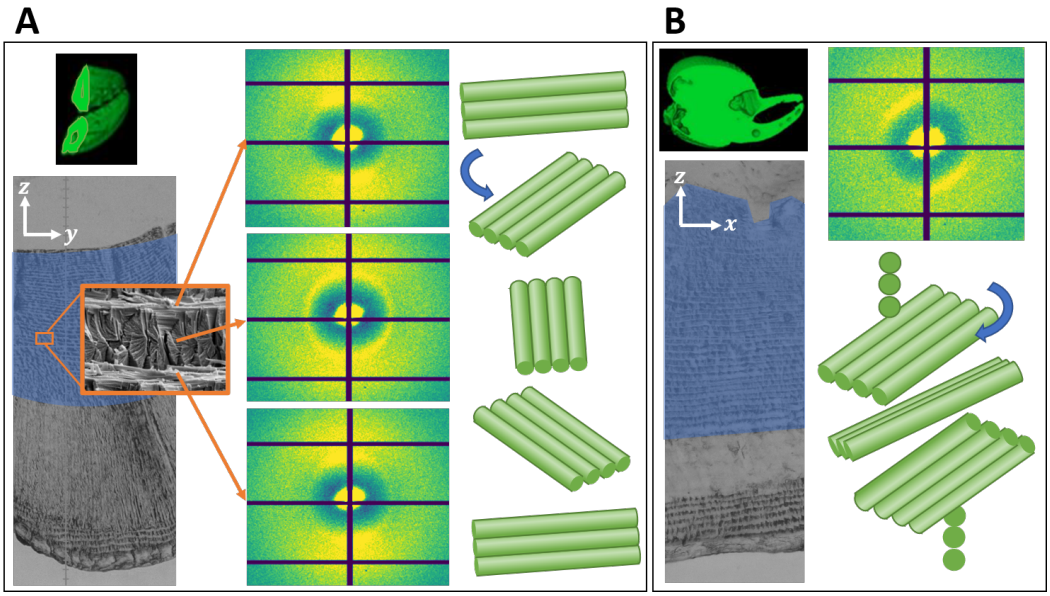

Figure 4.6: SAXS for Bouligand structure with (A) transversal orientation and (B) longitudinal orientation.

distribution is fitted to find the peak mean (which corresponds to the main diffracting fiber orientation) and peak broadness (which is inversely related to the sharpness). An example of the fit process is shown in Fig. 4.8(right). From the fitted results for each mapped pixel, the intensity of the anisotropy is then defined as the peak height devided by the standard deviation, since a faint sharp peak (diffracting in one direction) is more anisotropic than an intense broad peak (diffraction everywhere). The intensity is then normalized by the same value (arbitrary units) such that the results from different orientations are comparable.

The results are plotted in Fig. 4.9 for both orientations. The direction of the lines represents the direction of the fibers that are diffracting and the length of the line represents the degree of anisotropy (longer line is equivalent to more aligned fibers). In the Unidirectional regions (mid orange sections), the fiber organization seen from both directions are both fairly uniform and textured. The transition from each region to the next is coherent with no sudden change in fiber organization. In the Endocuticle / Bouligand regions (upper blue sections), there is more alignment seen in the transversal direction than in the longitudinal direction, as a result of the highly textured interlayers as seen in Fig. 4.6(A). The waviness in the outerprofile of the patterns in the blue regions represent the periodicity of the Bouligand laminates, which are on the order of $10\mu m$ in thickness, consistent with that seen through SEM

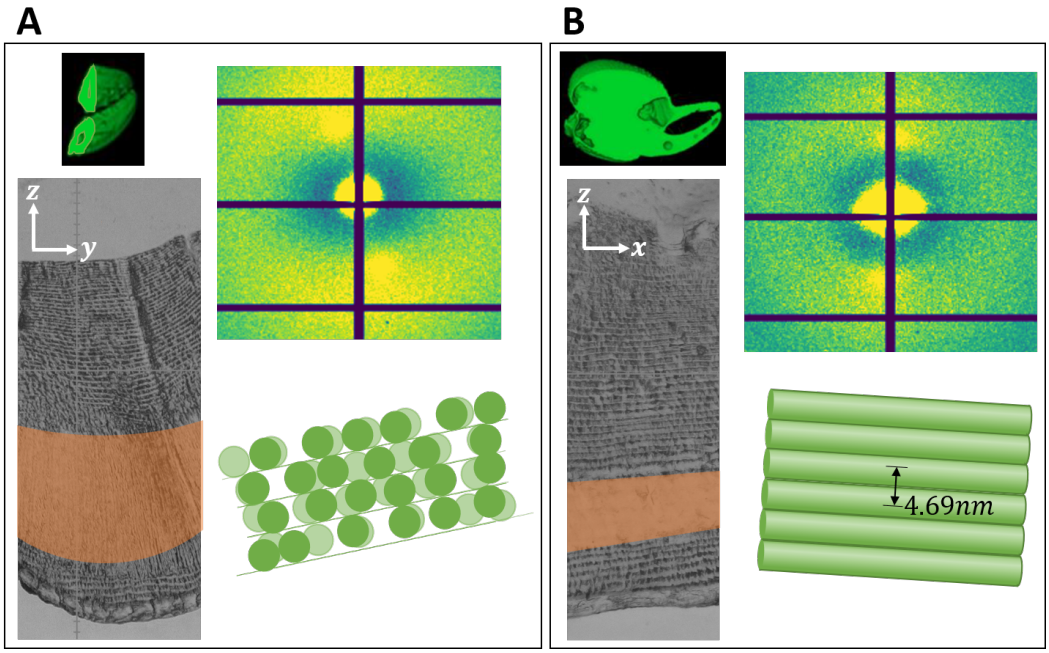

Figure 4.7: SAXS for Unidirectional structure with (A) transversal orientation and (B) longitudinal orientation.

(Fig. 4.3). In the hypothesized helicoid structures in Ref [155], there is an additional twist to the pure rotations in the Bouligand structure; the lack of heterogeous fiber texture (no periodic change in direction) suggest that the twist axis is always along the fiber direction in each layer of fibers, such that the fibers remain tangential to the hoop direction of the cuticle.

4.2.2 Elemental distribution of metals in protein matrix

Metals are hypothesized to exist in the protein matrix of biological exoskeletons in two ways: (1) minerals or (2) coordination bonds. In their mineral form, metals are theorized to provide higher hardness and toughness for the proteins, especially in marine bodies due to hydration-induced softening [130, 138, 139, 141, 145, 156]. Common minerals found in biological shells include crystalline or amorphous Calcium Carbonate [148, 157], Calcium Phosphate [147, 158], and iron oxides [159], and can exist as nanoparticles in different shapes and distributions. In marine Arthropods, relatives of our scorpions, amorphous Calcium Carbonate (ACC) and Calcium Phosphate (ACP) has been found, [148]. ACC and ACP are metastable phases that requires the organism's active stablization to exist in the biological system, and has been found to crystalize immediately [160]. Metal-coordination

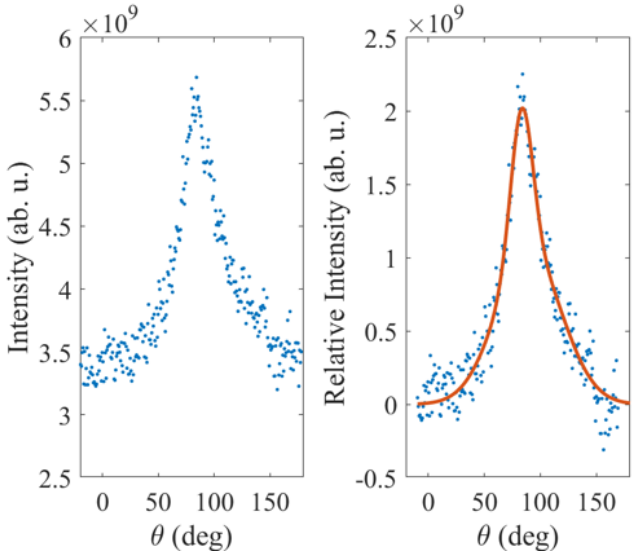

Figure 4.8: Fitting process for anisotropy analysis.

bonds, on the other hands, describe the chemical interaction between bio-molecules such as proteins and metal ions (Ca^{2+}, Fe^{3+}, Zn^{2+}, etc.) between covalent and non-covalent bonding, and have been observed to increase toughness and hardness of bio-materials in more recent years, in addition to their multifunctional roles such as catalysis or signal transmission [142, 161]. Specifically, Phosposerine-Ca (containing Ca and P) is found in sandcastle worm glue [161] and Zn^{2+} metal-ligands were found in spider fangs [142].

X-ray fluorescence shows distribution of four different elements in the *tarsus* cuticle. No significant orientation dependence was found. P, Ca, and Fe are inhomogeneously distributed with aggregations in every region. The aggregation sites for Ca and P are closely correlated, suggesting that they are linked in either mineral (likely ACC or ACP) or ionic form (Phosposerine-Ca). Zn is distributed more evenly, with the highest concentration in the exocuticle and lowest in the endocuticle, while its concentration in the unidirectional region is in the middle. This is consistent with the distribution of Zn in spider fangs, which is used to inject venom into their preys and thus require high hardness and resistance to failure. A typical radially integrated WAXS spectrum of the SP cuticles is shown in Fig. 4.11, with broad background diffraction and no sharp peaks corresponding to crystal diffraction, suggesting that there are no minerals in the materials and therefore likely only metal-coordination bonds.

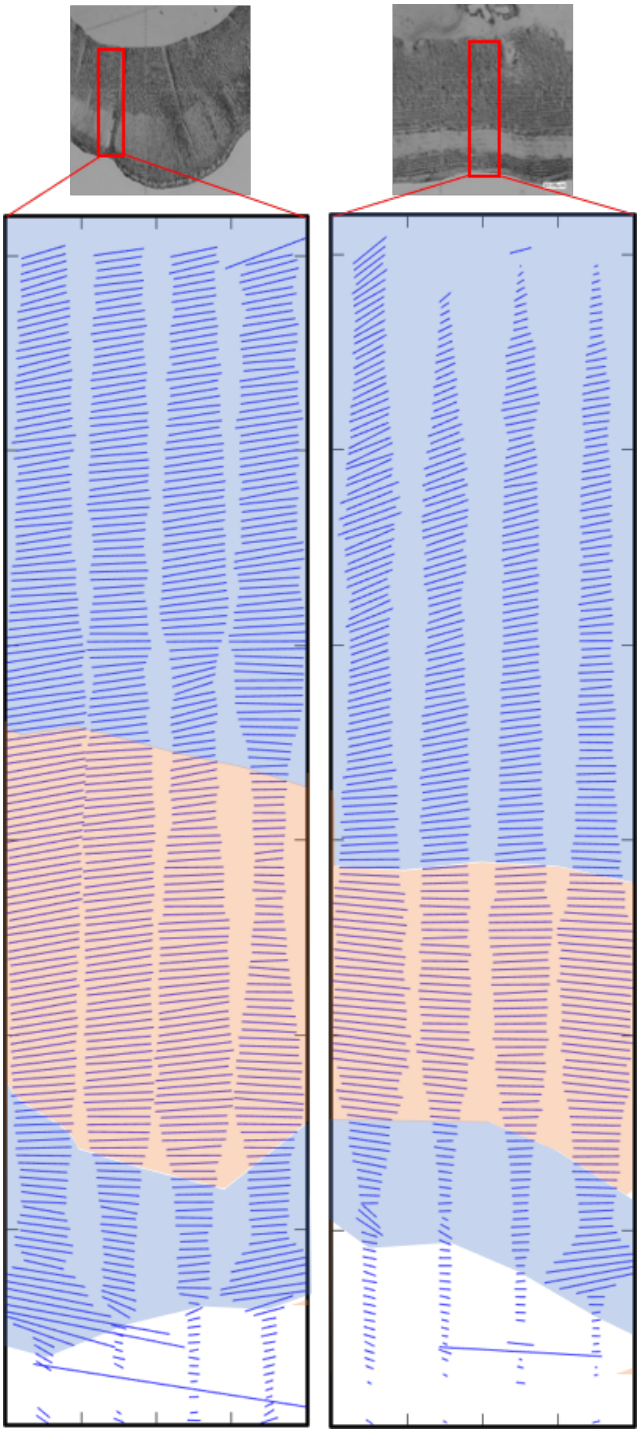

Figure 4.9: Fiber organization from SAXS diffraction for the SP cuticles in the (left) transversal and (right) longitudinal orientations.

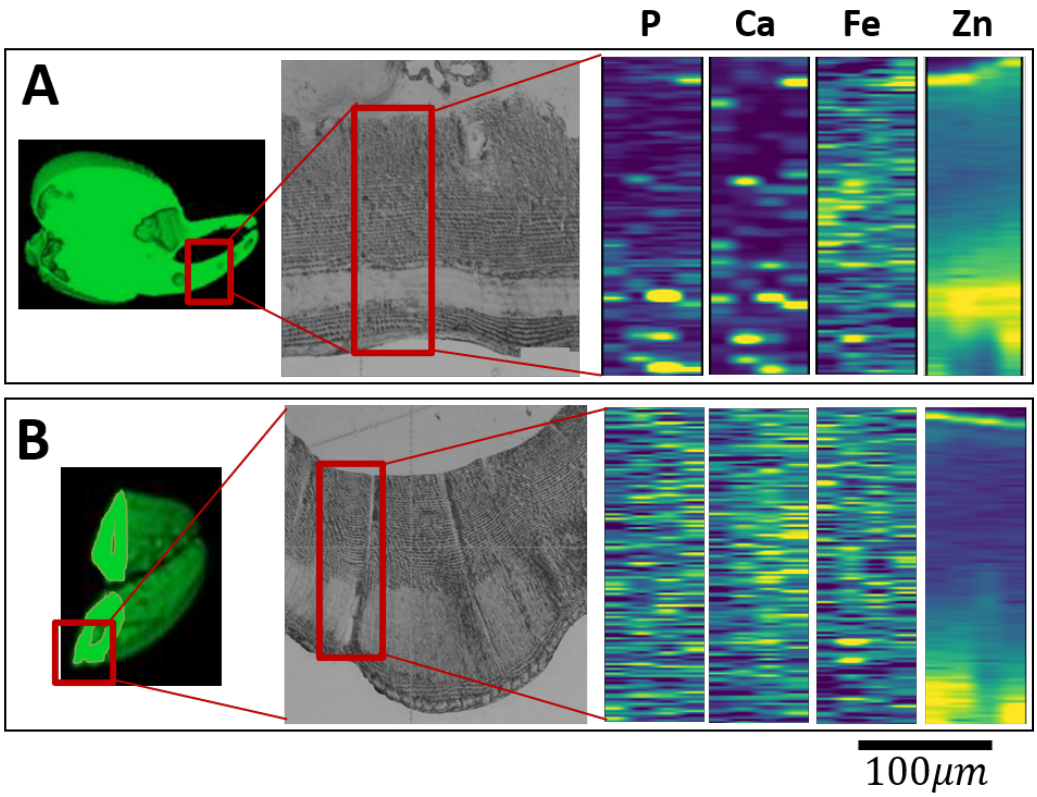

Figure 4.10: Elemental map from X-ray fluorescence.

4.3 Mechanical Set-up

With further understanding of the intact material microstructure, mechanical experiments were designed to investigate the site-specific stiffness, strength, and toughness at the microscale through pillar compression experiments, 3pt bending experiments as outlined in [21], and tensile experiments. Details of the pillar experiments can be found in Section 2.3; pillars were contained within individual laminates to eliminate effects from interfaces.

4.3.1 Attempts at 3pt bending

Measuring fracture toughness at the microscale proved to be difficult, with the sample sizes inconsistent with standard testing procedures [162]. Recently our group has developed a technique that measures the crack opening and R-curve of μm-scale bone samples through 3pt bending experiments [21]. We attempted to perform the same set of experiments, extracting rectangular pieces of the sample from the cuticles using the FIB. The sample is highly porous both naturally and as

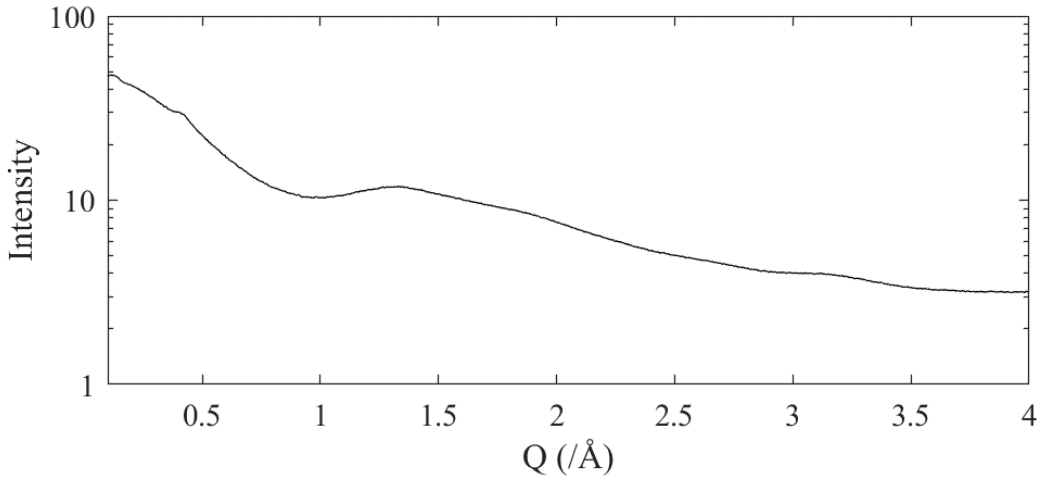

Figure 4.11: WAXS spectrum from the SP cuticles showing no crystallographic phases.

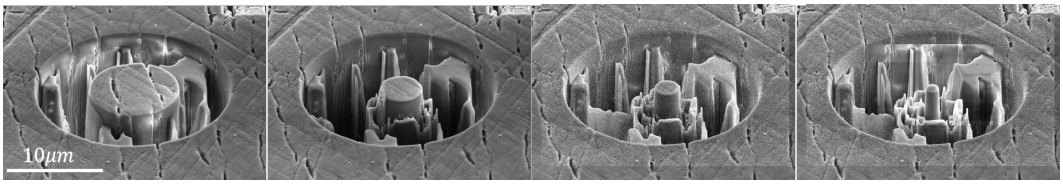

Figure 4.12: High porosity in SP cuticles as seen in FIBbing.

a result of the FIB etching away the protein faster than the chitin fibers, resulting in large free volumes as seen in the pillar making process in Fig. 4.12. This becomes an issue with sample deposition onto Si wafers later in the testing process.

A sample polished to reveal its longitudinal cross-section is shown in Fig. 4.13(A). Trenches were etched in the Bouligand region to produce a rectangular piece that can be etched from the side and taken out of the bulk of the material, as is shown in Fig. 4.13(B). Upon etching away the left and lower parts of the rectangle, the piece bends without physical manipulation, revealing small residual stresses in the material that curls the material inwards slightly (Fig. 4.13(C)). To glue the sample onto a substrate, Pt was deposited onto parts of the sample using evaporated Pt. Slight bounce off of Pt from the deposition landing on the sample resulted in severe distortion of the piece, as is shown in Fig. 4.13(D), as a result of the porosity and the residual stress. Plans to measure toughness through 3pt-bending was thus suspended and switched to micro-tension experiments, as is used in mechanical characterization of other materials [6, 67].

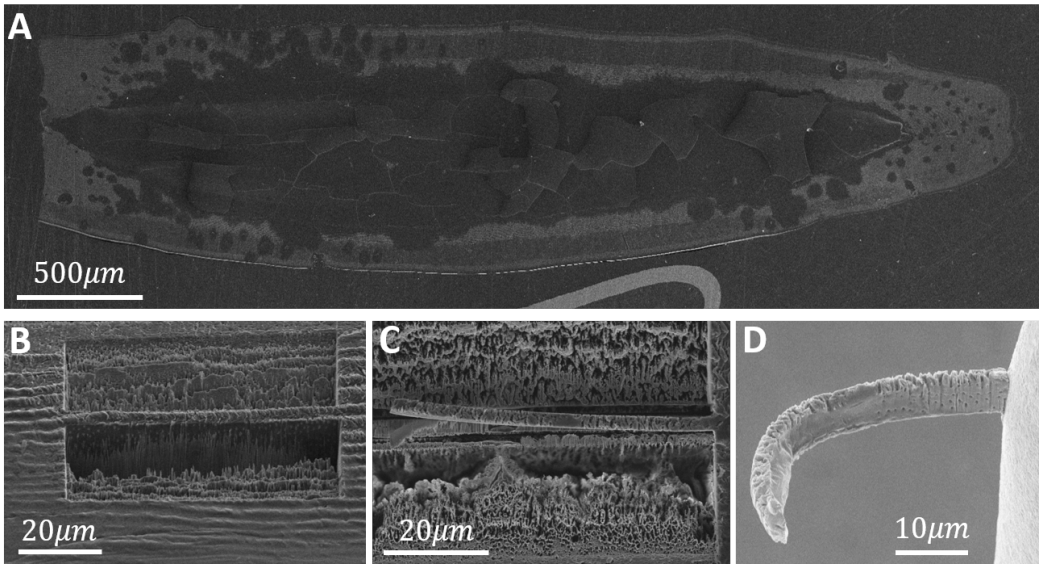

Figure 4.13: Porous 3pt-bending sample deforming.

4.3.2 Micro-tension experiments

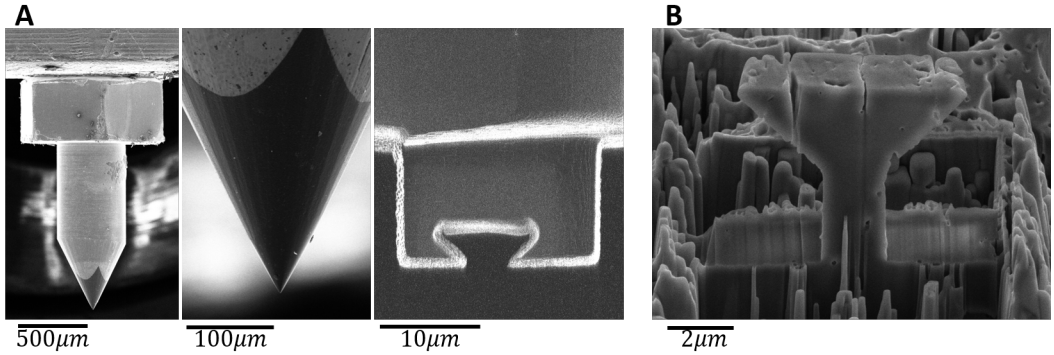

Figure 4.14: Micro-tension experimental set-up with (A) custom grip and (B) half dogbone samples.

Tensile experiments were performed on the Agilent InSEM in the FEI Quanta. The experimental setup is similar to that in Section 2.3 and more details can be found in [32, 67]. A few iterations were made to fabricate the suitable tensile grip, with failed attempts on tungsten needles epoxied/super-glued/crystalbonded to a InSEM tip base. The final grip was fabricated out of a Diamond cone tip from Synton-MDP AG, with its overview and shape in Fig. 4.14(A). The grip clearance is 4.2μm with 20μm thickness. Example of a half dogbone fabricated out of the samples using FIB is shown in Fig. 4.14(A). Each dogbone is restricted to one lanimate either in

the Bouligand region or in the Unidirectional region to eliminate influence from the interfaces.

4.3.3 Finite Element Analysis (FEA)

FEA was performed to visualize and interpret stress concentrations and localized behavior of the natural composite. We used Abaqus CAE 2018. Pillar compression experiments were mimicked with a 1.3μm diameter pillar with 1:3 aspect ratio. Identical fibers with 70μm spacing, tiled in a square pattern, populated the pillar. Due to the lack of reported experimental results for the material properties, size, and hierarchy of either the chitin fibers or the protein matrix, multiple tests were done for fibers of 20μm or 70μm diameter, with fixed fiber stiffness as E_f =70GPa [61, 155]. 4 different protein modulus values E_p were used for a total of 8 tests: 10MPa, 35MPa, 100MPa, 1GPa, which fall in the ballpark of what had been simulated or predicted [61, 155]. Meshes with 20μm roughly in size were used, and an embedded constraint was set between the fibers and the bulk of the pillar. Poisson's ratio for both the fibers and the bulk were set to 0.4. A rigid punch with a 2μm diameter was set on top of the pillar to control compression force for buckling analysis. The BC at the top and bottom of the pillar were set to Encastre for no-slip conditions.

The simulations were done in two steps:

1. A Linear perturbation step (Buckling) with Load=1 was run to find the first 24 eigenvalues (largest allowed for the amount of computing power available). The Model Keywords were editted to output the eigenmodes, and reran.

2. A Static, Riks step (replacing the buckling step) with the first buckling eigenvalue as load was run for post buckling analysis. The buckling eigenmode output were input into the new model's Keywords as to initiate the buckling modes. The results from this step were taken to further analysis and compared with experimental data.

This turns out to be a standard process and can be found on many tutorial websites.

4.4 Localized Buckling Under Compression Geometry

800nm diameter pillars in the two fiber organization regions on a transversal cross-section were compressed for their mechanical response. For pillars in the Bouligand

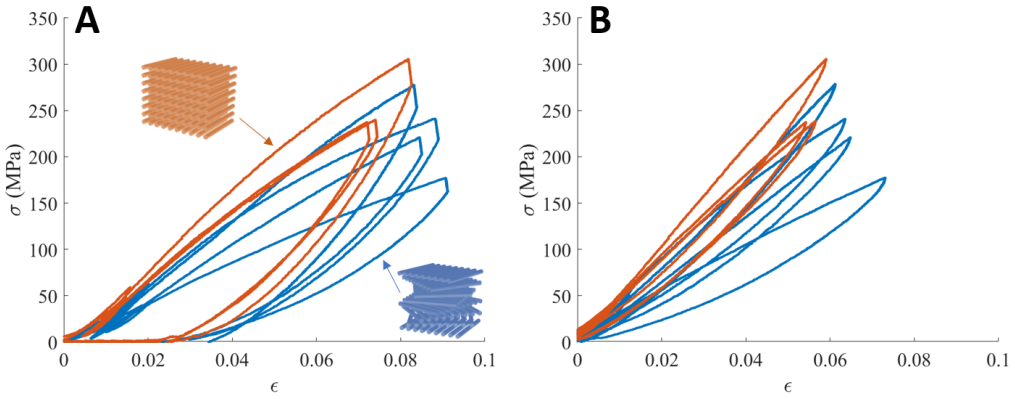

Figure 4.15: Engineering stress-strain response of pillars in both regions before and after creep isolation.

region, the fibers had a random chance of being aligned with the loading direction or misaligned due to fiber structure; for pillars in the Unidirectional region, the fibers were aligned with the loading direction. Four pillars in the Bouligand region and three pillars in the Unidirectional region were recorded, and their engineering stress-strain data (corrected for Sneddon effect [96]) are shown in Fig. 4.15(A). The significant load drop during the 10s hold at the end of loading and before unloading suggests creep in the material, likely as a result of reabsorption of water from the atmosphere, since the samples had been stored for a month since they were embedded. Since it was impractical to quantify the water content, we used a linear approximation for the creep (fitted to the hold segment) and subtracted it from the original data to obtain the "instantaneous" mechanical response, as is shown in Fig. 4.15(B). While we successfully eliminated creep, there still was significant hysteresis in the response, partially due to the nonlinearity in the creep and mostly from microplasticity. We focused on the "instantaneous" response so as not to focus on the water effect too much, more details of which are shown below.

Mechanical response of the Unidirectional fibers (aligned with the loading direction) are repeatable due to the determined fiber direction while the response from the Bouligand fibers are scattered as the fibers are randomly oriented. When the pillar is in the direct center of the Bouligand laminates with fibers pointing mostly towards the loading direction, the response is close to that from the Unidirectional pillars; when the pillar is off-center of the Bouligand laminates, the fibers are rotated away from the axis, resulting in lower stiffness. The effect on stiffness from fiber direction (angle between fiber and loading direction) are shown as dashed lines on

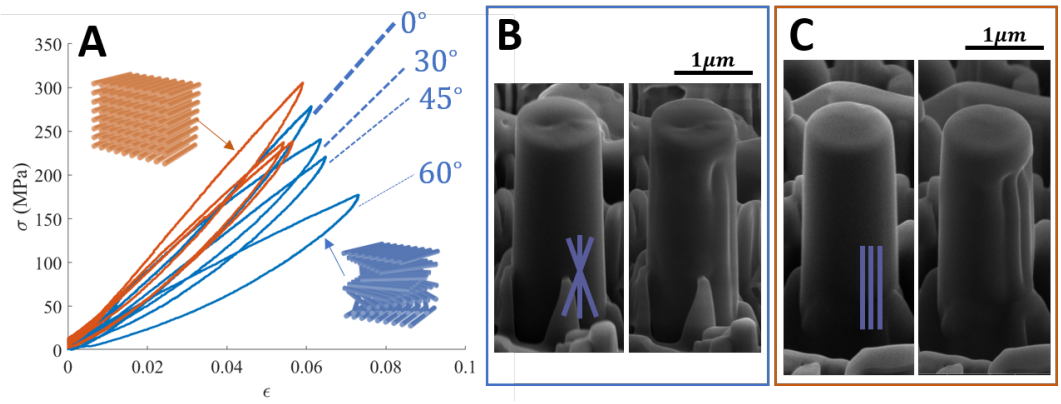

Figure 4.16: Pillar compression response in scorpion shells. (A) Instantaneous stress-strain response for the deformation in the (B) Bouligand and (C) Unidirectional structures.

the plot, where the slope decreases with increasing misalignment. The fitted moduli from the initial unloading segment is 5.4±0.3GPa for the Unidirectional pillars and 4.5±0.5GPa for the Bouligand pillars, which are both lower than that measured from nanoindentation [154], although the trend stays the same. This could be from the inaccurately assumed Poisson's ratio used to calculate modulus in the indentation tests or from softening effects due to hydration. The post-compression pillar SEM images are shown in Fig. 4.16 for both fiber structures. Clear signs of fiber collapse can be observed on both pillars after compression, with the unidirectional pillar suffering from more severe distortion from the fiber collapse, despite being compressed to lower strain. The preferred collapse direction (on the right half of the pillars) is a result from the inevitable slight misaglignment in the instrumental set-up.

FEA of pillars with Unidirectional pillars reveal localized buckling of embedded fibers during compression (Fig. 4.17(A)), which is consistent with the collapsing behavior seen in Fig. 4.16(C). Color in the stress distribution represents Mises stress. Since post-buckling produces nonlinear stress-strain response, we expect the simulated post-buckling data to divert from the simple linear rule of mixture calculations. Hypothetically, by comparing the scaled stress-strain data for different combinations of fiber size / protein stiffness to that experimentally measured, we should be able to identify the best combination that describes the individual constituent properties, which remain inaccessible to this day. Closer evaluation reveals that for all the combinations, buckling happens at strains way larger than 0.1 (with the smallest of 0.1423 for 20nm thick fibers and $E_p = 10MPa$), before which the

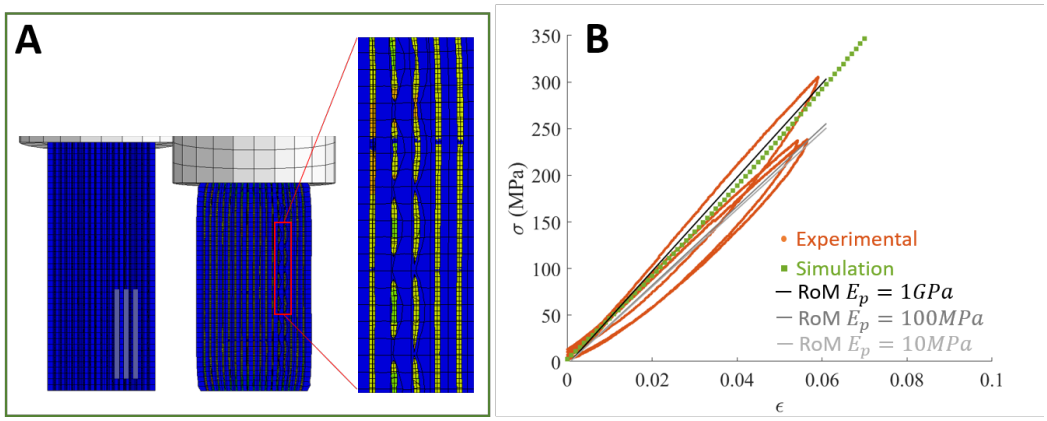

Figure 4.17: Stress distribution visualized through FEA and compared to experimental and theoretical data.

response was purely linear elastic. Among all the combinations, the simulated elastic response of $E_f = 70GPa$, $E_p = 35MPa$, 20nm thick fibers matched the experimental results best, which is shown in Fig. 4.17(B) along with theoretical rule-of-mixture stress response and the measured experimental response. From the pre-buckling elastic response alone, protein stiffness does not provide significant distinction. The experimentally observed buckling, despite not reaching buckling strain, suggest that the fibers are either discontinuous in the pillars or other defects are lowering the destablization stress (such as Ga implantation caused stiffening at the pillar top).

4.5 Failure Analysis through Micro-Tension Experiments

Contrary to compression, tensile tests reveal higher stiffness in the Bouligand region (same orientations as in Section 4.4) than in the Unidirectional region, as is shown in Fig. 4.18, despite the Bouligand pillar with visibly higher porosity as perceived in the SEM images. Both pillars deformed up to a 16.5% strain without failure, suggesting significant plasticity from the protein and slip between fibers and their surrounding protein.

The tensile response of pillars are not repeatable, and more data is needed for statistically conclusive results. As is shown in Fig. 4.19, two pillars of the same size from the same Unidirectional region on the same sample (transversal orientation) deform to different strains. While the two pillars follow the identical initial linear elastic response with 35MPa modulus, one fails at the 3% strain while the other deforms up to 17% without failure. The repeatable elastic segment suggests that

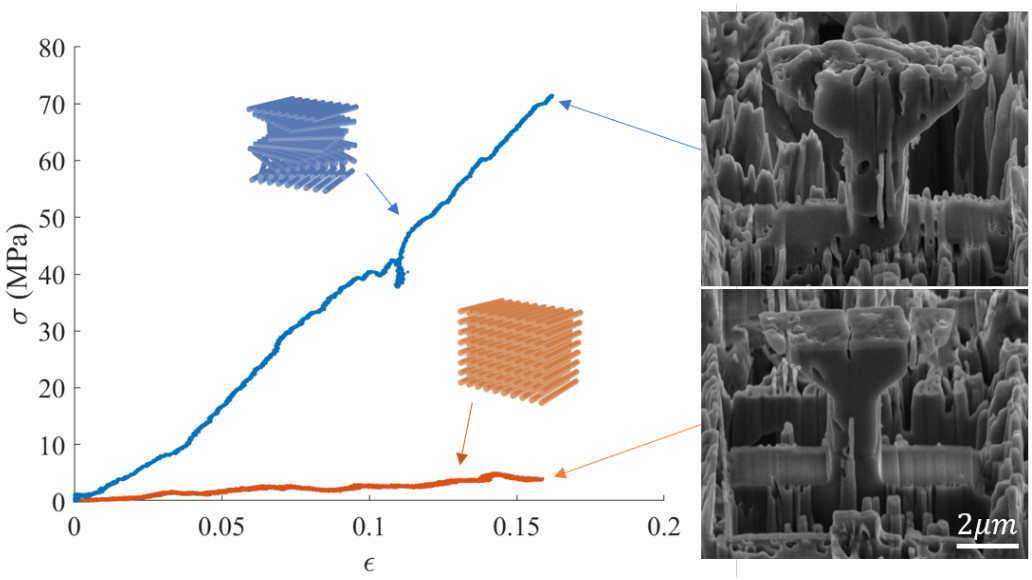

Figure 4.18: Bouligand microstructure stiffer than Unidirectional in the tensile configuration.

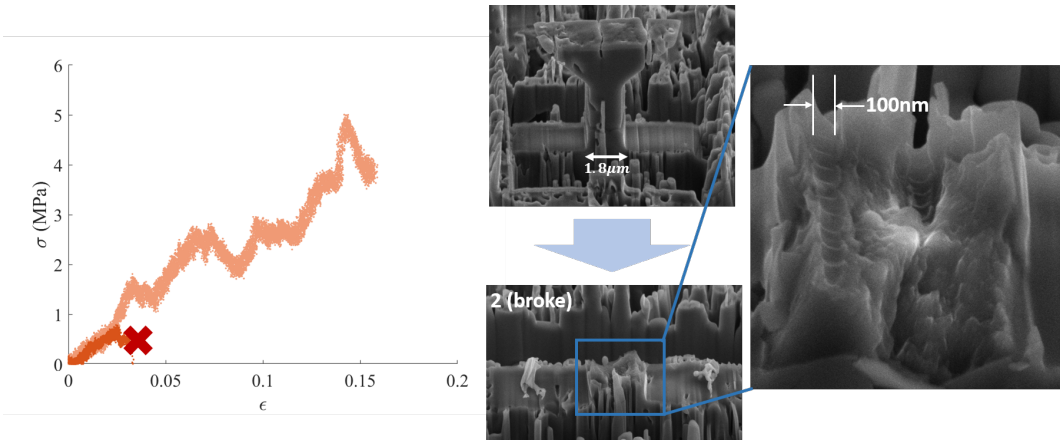

Figure 4.19: Unidirectional fibers pulled off from the protein matrix in tension experiments with stochastic failure strength.

the drastic different response are both authentic data measured from the material itself, in contrary to experimental errors. The stochastic nature in the failure stress between the two pillars suggests that despite deforming the weakest link in both pillars, the interface between the fibers ends and the protein can have different strength, similarly to how initial micro-crack distribution changes the failure strength of brittle materials. A closer evaluation of the fracture surface as seen in Fig. 4.19 suggests a clean cut fiber break off from where it embeds in the protein: the periodic grooves remaining on the fracture surface match the measurement for the fiber

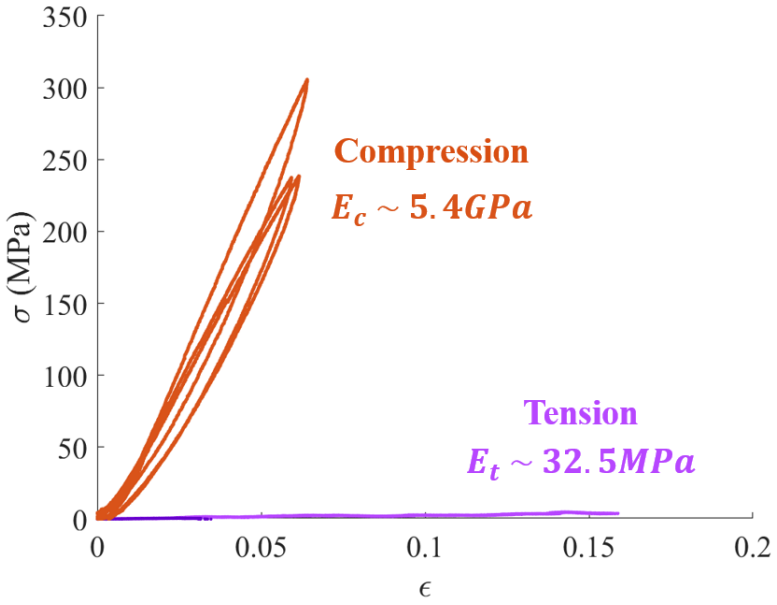

Figure 4.20: Compression-tension asymmetry in the Unidirectional region.

stacking from SEM images in Ref [154, 155]; no fiber pull-out (holes or fibers sticking out) is observed. Comparing the compression and tension response in the Unidirectional region (Fig. 4.20), the tensile modulus is orders of magnitude lower than in the compression geometry (5.4GPa), suggesting that it is the weakest link that dominates stiffness in the tensile configuration — the protein between discontinuous fibers. This confirms the use of 35MPa as E_p in the FEA in Section 4.4.

4.6 Summary

Chitin fiber structures are hypothesized to dominate mechanical behavior of arthropod shells, which are know for their high strength and toughness. Synchrotron X-ray SAXS and WAXS are used to reveal the intact fiber organization in Scorpion cuticles that match fractography observations, while fluorescence uncovers transition metals in the form of metal-coordination bonds, which have been shown to stiffen and toughen exoskeleton proteins in arthropods and insects. Combined site-specific microscopic compression and tension experiments reveal tension-compression asymmetry in both the Bouligand and Unidirectional microstructural regions, shedding light on the complex mechanical behavior and how the two microstructures are optimized for the two stress configurations. In the Unidirectional layers, which is unique to the SP tarsus cuticles, compression manifests as localized buckling of

the fibers while tension passes onto the weakest link in the material, which is the protein matrix between discontinuous fibers. These observations shed light on how these complex fiber-reinforced bio-materials are optimized for their functionality and ambient conditions.

Chapter 5

VISCOELASTICITY OF JELLYFISH VIA IN-SOLUTION INDENTATION

Soft biological tissues lend their complex self healing properties to bioinspired materials with a multitude of applications. Previous studies reveal that jellyfish can exhibit mechanically driven shape recovery, yet there lack quantitative characterization of its viscoelasticity to accurately model and replicate this behavior in simulations or aritificial systems. Conventional mechanical experiments designed for engineering materials are not suitable for jellyfish due to its complex structure and necessary ambient conditions (moisture). We use in-solution flat punch indentation to conduct stress-relaxation, DMA, and quasi-static loading to identify and cross-examine viscoelastic models that accurately depict jellyfish Mesoglea.

5.1 Introduction: Mechanically-Driven Self-Healing of jellyfish

The viscoelastic nature of soft biological tissue enables a wide range of organ functions, such as self-healing and shape recovery. For example, sea anemones change shape with water currents [163]. Owing to their complex gel network structure, the both solid- and fluid-like properties of these animals give rise to their self-healable multifunctionality, inspiring novel material avenues with application in soft robotics [164], tissue engineering [165], bio-implants [166], etc. The success of designing artificial soft materials with optimal properties relies on a full understanding of how microstructural constituents facilitate the mechanical response of natural hydrogels, such as that in jellyfish.

It was revealed that the shape of grafted jellyfish can retain its symmetrical configuration via mechanically driven processes without cellular regeneration [167]. As one of the simplest animals, jellyfish consists of mainly its Mesoglea, which is a natural hydrogel containing a small number of cells; it is thus hypothesized that the mechanical properties of Mesoglea is the origin of jellyfish's self-healing behavior. A natural proof to this hypothesis would be a full-scale FEM run that captures the shape recovery under simulated muscle contractions. To do this, accurate depictions of the material parameters are needed. Unlike artificial materials, which can be cast into standard shapes for tensile or compressive testing [168–171], mechanical ex-

periments on biological tissue has been challenging, since it often requires specific ambient conditions (physiological temperatures [172], hydration [173], etc.) and custom instrumental set-up (unconventional stress conditions [174], sample damage [175], etc.). Currently, there is still a lack of a universal testing standard for the characterization of soft biomaterials, which gives rise to large discrepancies among different reports of the same subject [176]. The viscoelasticity of Mesoglea has been studied since the 1960s [173, 175, 177], yet there is still a lack of a constitutive model that describes the shape retaining process observed by Ref [167] due to the large differences among the various reports. In addition to viscoelasticity, hydrogels' unique poroelastic behavior serves as another source of time-dependent response, rendering the analysis of many mechanical experiments infeasible.

To overcome this problem, we have established mechanical experiments to characterize both static and dynamical response of the jellyfish Mesoglea in sea water using nanoindentation, which has been adopted in the characterization of viscoelasticity [178, 179] and poroelasticity [180, 181] in artifical hydrogels, validating the stress output of indentation by comparing to macroscopic experimental results. Unlike tension or compression, indentation does not require complicated material handling before or during the tests, therefore allowing for fast and repeatable data acquisition without interfering with material behavior.

5.2 Experimental Setup

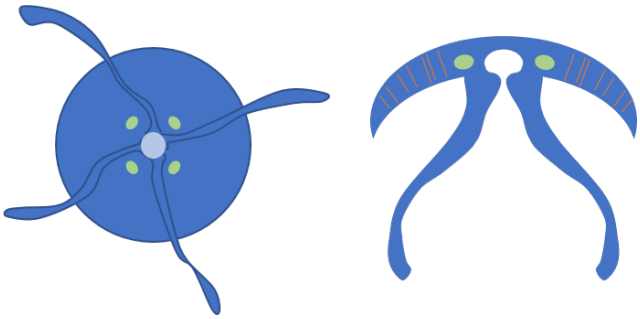

Figure 5.1: Diagrams of the *Aurelia aurita*: (left) bottom-up view; (right) vertical cross-section.

Fig. 5.1 provides the bottom-up and cross-sectional diagram of the *Aurelia aurita* jellyfish. The fish is mainly composed of its body (round flat bell) and its four legs. The bell diameter ranges from a few millimeters to a few centimeters (depending on its age) and is thickest at the center while thinnest on the edge. There is a ring

of muscles on the lower side of the edge that controls the movement of its body (propelling water, which enables swimming [182]). The thickness of the fish also varies, with a 3cm wide fish usually ~5mm at its thickest part. At the center of the fish is its stomach — a small cavity that holds and digests food particles. Around the stomach lie four gonads, which are its reproductive organs. Collagen fibers are randomly dispersed throughout the gel, oriented across the bell thickness, shown as the orange lines in Fig. 5.1(right).

5.2.1 In-solution flat punch indentation

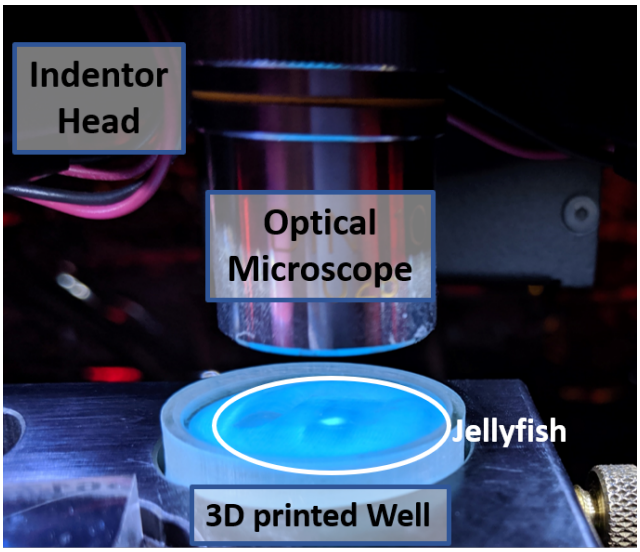

Figure 5.2: Indentation test setup for jellyfish in solution.

Indentations were carried out in the KLA G200 XP system. To conduct accurate indentation tests, the jellyfish were sumberged in seawater with 8% menthol (anesthetic) such that they were fully hydrated but immobile. A custom 3D printed sample holder with 2.5mm diameter was used to hold the solution and the jellyfish (Fig. 5.2). Initial efforts to glue the jelly to the substrate failed with both regular glue and suture glue, thus the fish were tested with anesthetic instead of adhesion. The top of the solution just covered the top of the jellyfish so that the indenter had enough displacement allowance to reach the fish. We used jellyfish ~2cm in width to control their age and thickness. Indents were all smaller than 200μm (<10% of its thickness), therefore the curvature and substrate effect were neglected. Indent locations were chosen around the stomach, between the gonads, so that they do not interfere with the results. Stress-relaxation, DMA, and ramp loading ("quasi-static"

indentation) were carried out for depths up to 150μm; for stress-relaxation, the displacement was ramped to target within 1s, then held for 300s after the initial "step." Cylindrical flat punchs with 120μm and 400μm diameter were used for constant area function and stable contact. Since salt water has a highly rusting agent, the tips were ultrasonically cleaned in IPA for 30min, then rinsed with IPA and air-dried after every experiment session.

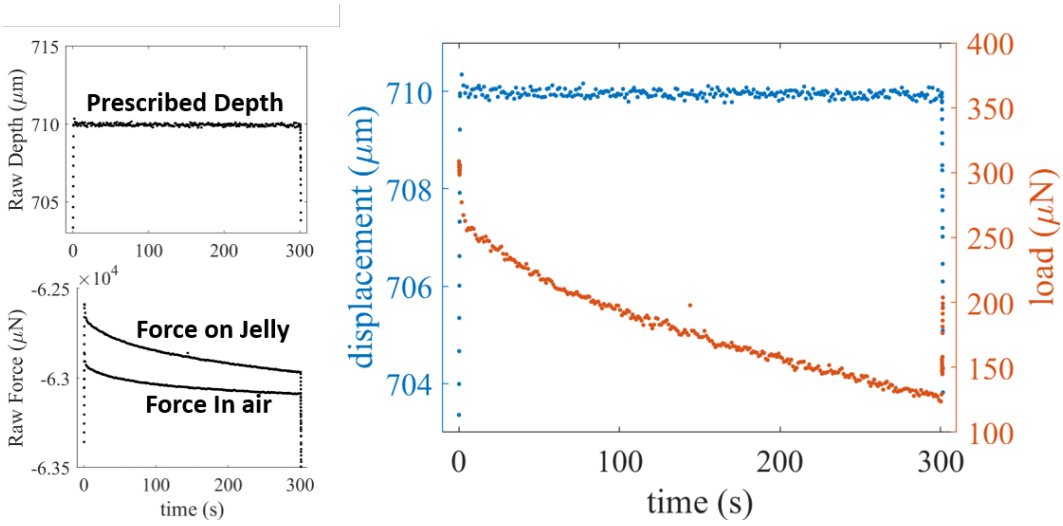

Figure 5.3: Correcting for machine stiffness by subtracting force in air at constant prescribed raw depth.

For the G200 XP and most common nanoindentors, machine detectable stiffness is usually above 50N/m, which translates to 100kPa. Since jellyfish is orders of magnitude softer than what the machine is able to detect (~1kPa), the tests were carried out to nominal depths in both jellyfish and air, then calibrated to find the exact load on the sample. The displacement of ramp tests were determined by examining the difference between tests in air and on the sample; for stress-relaxation and DMA tests, since the initial ramping happens in a short amount of time (1s), the corrected displacement is determined as the nominal depth minus the microscope focus length on the jellyfish's surface (which is calibrated to be at 0 depth), which can give errors up to $\sim 20\mu m$. Example of a stress-relaxation test being corrected is shown in Fig. 5.3. It can be seen that the load coming from the jellyfish starts at 300μN while the machine stiffness contributes up to 6.3mN, a clear evidence that automatic detection in the machine would treat jellyfish as air.

Validation for the method was done using artificial gel with 2.5% Agarose (in water). Examples of ramp-hold tests are shown in Fig. 5.4, where repeatable load-

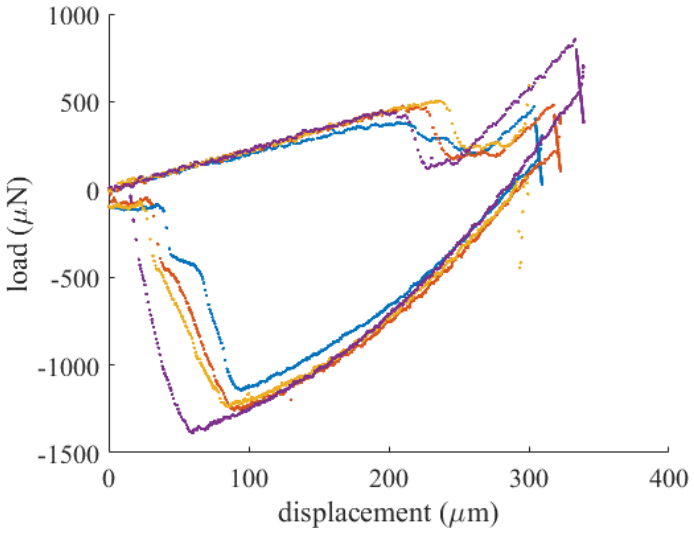

Figure 5.4: Repeatable measured load-displacement data for artificial gel.

displacement curves were measured for four separate tests using a $400\mu m$ punch. At $220\mu m$ depth, the sample touches the sides of the tip, resulting in the "sink-in" dip in the load data and subsequent stiffening. The measured reduced modulus is $21 \pm 1 kPa$, which falls between that measured for macroscopic Agarose with 1% and 5% concentration [183], validating that the method produces reliable and repeatable results.

5.2.2 Dynamic Mechanical Analysis (DMA)

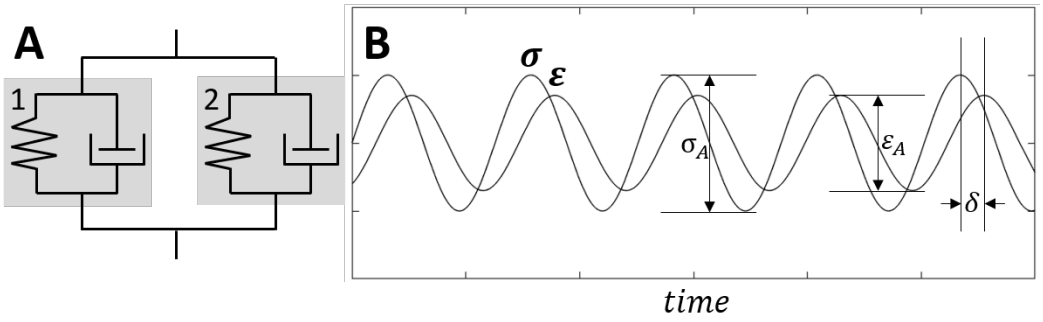

Figure 5.5: Representation of DMA. (A) DMA system diagram with 1-machine response and 2-material response. (B) Representation of measured response.

Frequency sweeps between 1Hz and 10Hz were carried out since the jellyfish pulses at ~0.8s in the wild, with $150\mu m$ pre-depth and $1\mu m$ oscillatory displacement. Forward and backward sweeps with the $400\mu m$ punch were conducted and averaged

to minimize effect from loss of hydration. A representative machine diagram is shown in Fig. 5.5(A), where the (1) machine viscoelastic response and the (2) material viscoelastic response are in parallel due to the indentor's capacitor set-up. Representative stable response for a DMA test is shown in Fig. 5.5(B), where in addition to a pre-indentation stress σ_p and strain ε_p, the stress $\sigma(t)$ and strain $\varepsilon(t)$ signals follow sinusoidal waves with the same frequency ω at a finite phase lag δ, with the stress amplitude as σ_A and strain amplitude as ε_A. Mathematically this is written as

$$\varepsilon(t) = \varepsilon_p + \varepsilon_A \sin(\omega t)$$

$$\sigma(t) = \sigma_p + \sigma_A \sin(\omega t + \delta).$$

The complex modulus E, storage modulus E', and loss modulus E'', which are standard DMA outputs [184], can then be calculated as

$$E = \frac{\sigma_A}{\varepsilon_A}$$

$$E' = E\cos(\delta)$$

$$E'' = E\sin(\delta).$$

Since the measured response is an addition of the two, therefore correction for the machine response is necessary, especially for soft / viscous materials [178, 179].

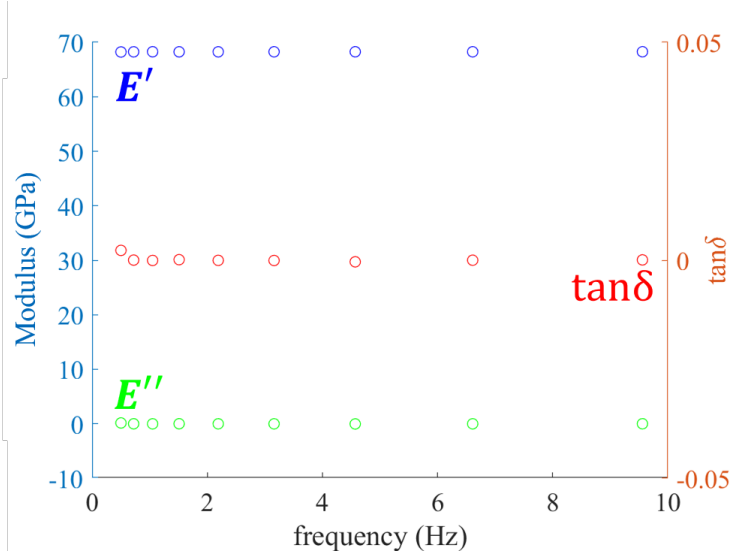

Figure 5.6: Air corrected DMA results.

Ideally, the method would be validated on a viscoelastic material with known viscoelastic properties; due to practical limitations and time constraint, we conduct

validation on Quartz, which is expected to be purely elastic ($E = E'$, $E'' = 0$). The same parameters (ε_p, ε_0, ω) were used for the frequency sweep on Quartz and in air, where the air data was subtracted from the measured data on Quarts to obtain the material parameters. The corrected data for the target frequencies on Quartz are shown in Fig. 5.6, where E' stays constant at 69GPa (consistent with regular nanoindentation [1]), while E'' and $\tan(\delta)$ stay constant at 0 as expected. For further validation, correction on standard PDMS should be used.

5.3 Viscoelastic Analysis of jellyfish Mesoglea using Indentation

The following analysis is used for the interpretation of measured data from indenting into jellyfish in seawater, adapted from more general forms of viscoelastic analysis [178, 184].

For a unit step strain input $\varepsilon(t) = \varepsilon_0 H(t)$, where $H(t)$ is the step function, define the stress relaxation function as

$$\sigma(t) = M(t)\varepsilon_0.$$

Then for an arbitrary input strain function $\varepsilon(t)$, the resulting stress is

$$\sigma(t) = M(t) * \varepsilon(t) = \int_{-\infty}^{t} M(t-\tau)\frac{\partial \varepsilon(\tau)}{\partial \tau} d\tau \tag{5.1}$$

with $*$ denoting convolution. Similarly, for a unit step stress input $\sigma(t) = \sigma_0 H(t)$, the creep function is written as

$$\varepsilon(t) = J(t)\sigma_0.$$

Then for an arbitrary input stress function $\sigma(t)$, the resulting strain is

$$\varepsilon(t) = J(t) * \sigma(t) = \int_{-\infty}^{t} J(t-\tau)\frac{\partial \sigma(\tau)}{\partial \tau} d\tau.$$

It is then possible to write $J(t)$ as a function of $M(t)$, since for a given material there should only be one constitutive relation. This gives

$$H(t) = J(t) * M(t).$$

Some additional definitions include: ω, which is the harmonic frequency in radians, E' as the storage modulus, and E'' as the loss modulus. Both E' and E'' can be functions of t and ε. It is also worth noting that although we are not writing ε as

independent variables in the previously defined functions, they can all be dependent on ε. The math so far should not be affected by this.

The following assumptions apply:

1. The time constants τ_i are fixed material parameters and not dependent on the strain.

2. For a DMA test with constant pre-strain and small oscillatory amplitude, we assume that $M(t, \varepsilon)$ and $J(t, \varepsilon)$ stay constant around their values at the pre-strain. This makes the math simpler since we can now take them outside of integrals.

There seem to be two ways of describing the material. First, there is the isostrain model, which is equivalent to a spring in parallel to N Maxwell elements. For this, we are going to work with the stress relaxation (stiffness) function, since it is easier in this case to start with a strain input. The relaxation function is written as

$$M(t, \varepsilon) = M_0(\varepsilon) + \sum_{i=1}^{N} M_i(\varepsilon) e^{-t/\tau_i}. \tag{5.2}$$

When N is large, the discreet time constants become a weighted relaxation spectrum, and the sum becomes a integral in the form

$$M(t) = M_0 + \int_0^\infty \frac{1}{\tau} H(\tau) e^{-t/\tau} d\tau.$$

where $H(\tau)$ is effectively the spring constant at the time constant τ. So far, we have not found any literature regarding using this relaxation spectrum with experimental data, since we can not simply fit an integral to data. It may be possible to guess functional forms with iterative methods to find a relaxation spectrum for a material, but we do not think that it is realistic for a mostly unknown material such as the Mesoglea. It might be worth pursuing for a standard material like PDMS. Moving forward, we will just work with the discrete model (sums).

The other model is the isostress model, with a spring connected to N Voigt elements in series. In this case, the creep (compliance) function, usually referred to as the Prony series [178], is

$$J(t, \varepsilon) = J_0(\varepsilon) + \sum_{i=1}^{N} J_i(\varepsilon) \Big(1 - e^{-t/\tau} \Big).$$

Note that there is a conversion from force-displacement to stress-strain in the indentation geometry. For a circular flat punch with diameter D, ideally we can write

$$\frac{E'}{1-\nu^2} = \frac{P_A}{u_A}\frac{\cos(\delta)}{D}$$
$$\frac{E''}{1-\nu^2} = \frac{P_A}{u_A}\frac{\sin(\delta)}{D}$$
$$M(t) = \frac{P(t)(1-\nu^2)}{Du_0}$$
$$J(t) = \frac{Du(t)}{P_0(1-\nu^2)}$$

where P is load, u is displacement; $(\cdot)_0$ denotes step input and $(\cdot)_A$ denotes harmonic amplitude.

5.3.1 Measured stress-relaxation function

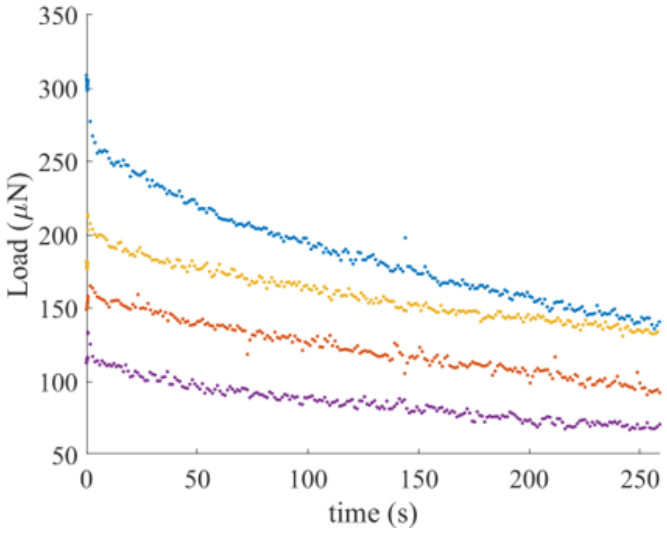

Figure 5.7: Stress-relaxation measurements at different locations on the same jellyfish.

Four sets of measured stress-relaxation data at $u_0 = 150 \pm 20\mu m$ on the same jellyfish is presented in Fig. 5.7, where the load decays smoothly with time. While the general shape of the curves follow similar trends, it is worth noting that the long term load (indicator of material elasticity at equilibrium after all energy dissipation has finished) vary significantly among the tests. Since the tests were done at the same distance from the center of the jellyfish at similar geometrical locations between

the gonads, this variation is not due to material heterogeneity. Loss of hydration over time (since the hydration state is not precisely-controlled) and the errors in indentation depth contribute to the varied long-term stiffness. Since hydration affects the decaying timescale, which remains stable among the different tests, the main reason for the variability is hypothesized to be due to variation in the exact indentation depth u_0.

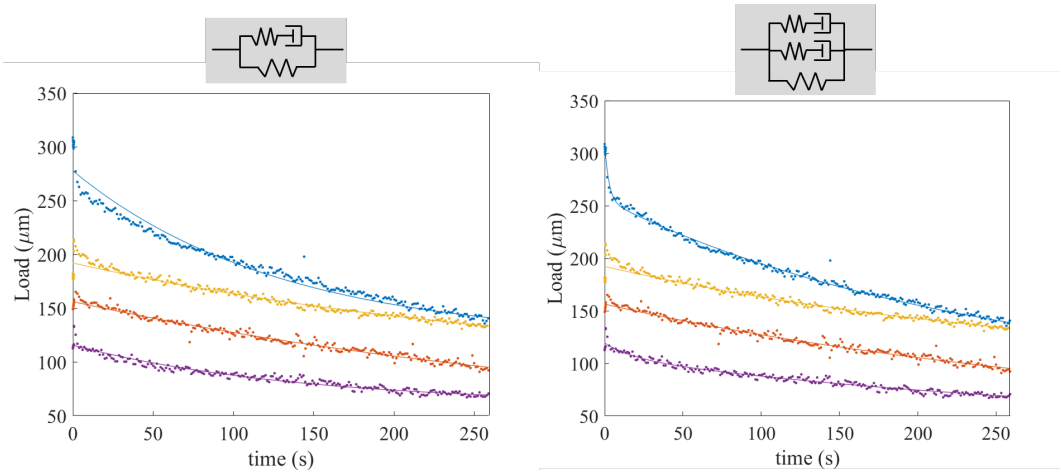

Figure 5.8: Standard viscoelastic models fitted to experimentally measured data.

Model	S3EM	S5EM
M_0	$3.2 \pm 1.5kPa$	$2.2 \pm 1.8kPa$
M_1	$4.5 \pm 1.8kPa$	$4.0 \pm 2.7kPa$
τ_1	$236 \pm 121s$	$404 \pm 253s$
M_2		$1.9 \pm 1.9kPa$
τ_2		$130 \pm 142s$

Table 5.1: Fitted parameters for isostrain viscoelastic models.

We fit the measured stress-relaxation data to multiple isostrain (standard linear viscoelastic) models as described in Eqn. 5.2 (which is mathematically simple with displacement-controlled experiments) using the $fit()$ function in Matlab with nonlinear least squares. All of M_0, M_i, and τ_i are released as free parameters to fit for. The result for models with 1 Maxwell element and with 2 Maxwell elements are shown in Fig. 5.8. It is clear that while both models capture the instantaneous load, long-term load, and overall decay, the isostrain model with 2 Maxwell elements (hereafter referred to as the standard 5-element model or S5EM) captures the initial faster decay and the later slower decay with higher precision. The resulting fitted parameters are shown in Table 5.1. The large standard errors in the fitted parameters,

especially that for E_2 in the S5EM, which is a result of a large variability in the data and the large number of free parameters, renders the results from these fits impractical.

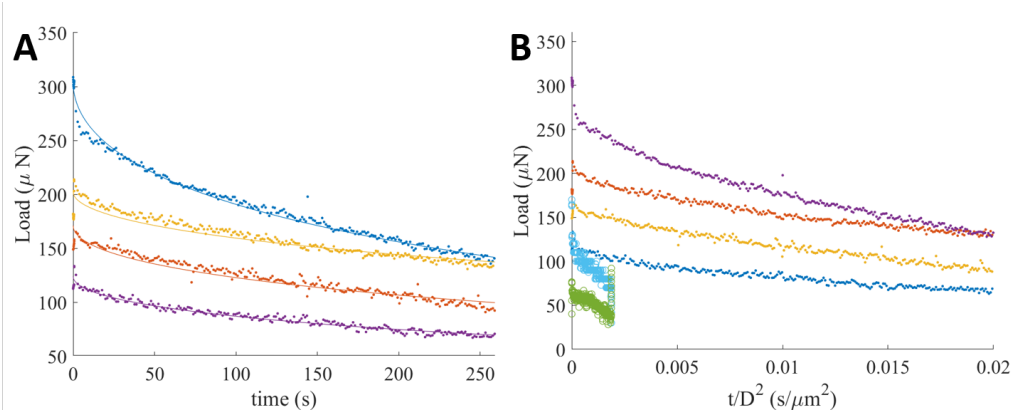

Figure 5.9: Poroelastic model [180] fitted to experimentally measured data.

In addition to the linear standard models, we also fitted the data to a generalized poroelastic model from Ref [180]; for a cylindrical flat punch, it can be written in the form

$$M(t) = M_{poro}\left(1.304e^{-\sqrt{\frac{vt}{D^2}}} - 0.304e^{-0.254\frac{vt}{D^2}}\right) + M_\infty$$

where D is the punch diameter and v is a scaled diffusivity constant. Using the same Matlab script, we fit for M_{poro}, v, and M_∞, resulting in the fit shown in Fig. 5.9(A) with $M_{poro} = 8.4 \pm 3.2kPa$ and $M_\infty = 0.0 \pm 0.0kPa$ (practically no long-term stiffness). For the model to be accurate, it is necessary that the rescaled relaxation function $M(t/D^2)$ is independent of punch diameter [180]; we therefore plot the rescaled relaxation data for both $120\mu m$ punch (as in Fig. 5.7) and for $400\mu m$ punch (open circles) in Fig. 5.9(B). While there is some overlap between the rescaled data, the result is unconvincing, thus for the remainder of this chapter, the standard linear viscoelastic models will be used.

Model	S3EM	S5EM
M_0	$84.6 \pm 1.3kPa$	$43.5 \pm 9.8kPa$
M_1	$99.6 \pm 1.2kPa$	$128.7 \pm 8.2kPa$
τ_1	$186.6 \pm 4.9s$	$382 \pm 48s$
M_2		$15.6 \pm 1.6kPa$
τ_2		$24.4 \pm 3.3s$

Table 5.2: Fitted parameters for isostrain viscoelastic models using average data.

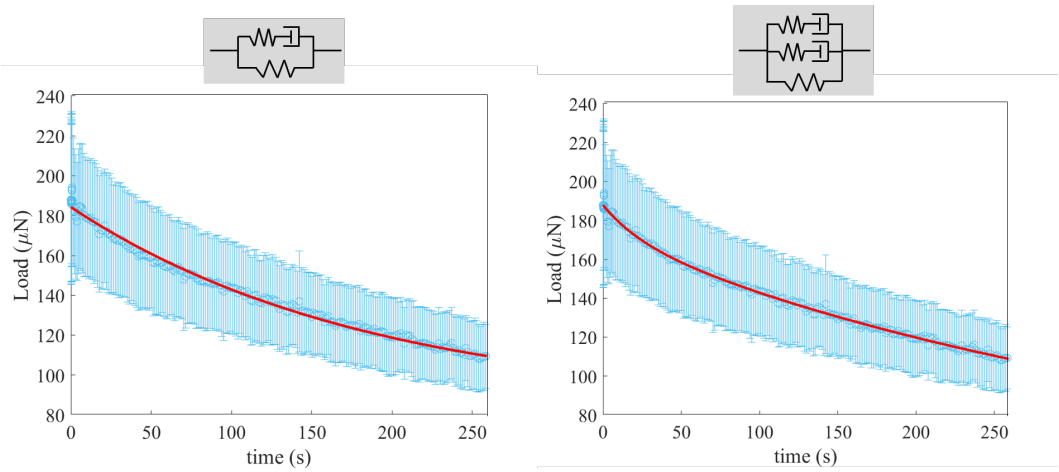

Figure 5.10: Standard viscoelastic models fitted to average experimentally measured data.

As mentioned earlier, the experimental variability is largely due to the error in the nominal indentation depth. We therefore fit the S3EM and S5EM to the average experimental relaxation data, as is shown in Fig. 5.10. The resulting parameters are shown in Table 5.2, where the errors are statistically determined from the fit to the average data. The resulting parameters are much more practical to interprete, with an instantaneous modulus of $184.2 \pm 1.8 kPa$ for the S3EM and 187.8 ± 12.9 for the S5EM, which are the comparable within experimental error. While qualitatively the two models seem similar, the two time constants in the S5EM are an order of magnitude away, which necessitates the additional Maxwell element.

5.3.2 DMA and 'quasi-static' loading: Measured v.s. predicted

Assuming isostrain, converting from relaxation to DMA, take a harmonic strain input

$$\varepsilon(t) = \varepsilon_0 e^{i\omega t}$$

and the resulting stress output should also be harmonic

$$\sigma(t) = \sigma_0 e^{i\omega t}$$

with σ_0 and ε_0 being complex and containing the damping information. This gives the storage and loss modulus:

$$E' = Re\{\frac{\sigma_0}{\varepsilon_0}\}$$

$$E'' = Im\{\frac{\sigma_0}{\varepsilon_0}\}.$$

We need to write σ_0 as a function of ϵ_0 and $M(t)$.

$$\sigma(t) = \int_{-\infty}^{t} M(t-\tau)\varepsilon_0 \frac{\partial\left(e^{i\omega\tau}\right)}{\partial\tau} d\tau$$

$$= \int_{-\infty}^{t} M(t-\tau)\varepsilon_0 i\omega e^{i\omega\tau} d\tau$$

$$= \int_{-\infty}^{t} \left[M_0 + \sum_{i=1}^{N} M_i e^{(t-\tau)/\tau_i}\right]\varepsilon_0 i\omega e^{i\omega\tau} d\tau$$

assuming it converges (it would not be realistic if it did not) and that we can take the sum out of the integral,

$$= \varepsilon_0\left[M_0 e^{i\omega t} + \sum_{i=1}^{N}\left(M_i e^{t/\tau_i} i\omega \int_{-\infty}^{t} e^{\tau(i\omega - 1/\tau_i)} d\tau\right)\right]$$

$$= \varepsilon_0\left[M_0 e^{i\omega t} + \sum_{i=1}^{N}\left(M_i e^{t/\tau_i} \frac{i\omega}{i\omega - 1/\tau_i} e^{t(i\omega - 1/\tau_i)}\right)\right]$$

$$= \varepsilon_0 e^{i\omega t}\left[M_0 + \sum_{i=1}^{N}\left(M_i \frac{i\omega}{i\omega - 1/\tau_i}\right)\right]$$

$$\implies \sigma_0 = \varepsilon_0\left[M_0 + \sum_{i=1}^{N}\left(M_i \frac{i\omega}{i\omega - 1/\tau_i}\right)\right].$$

This then gives

$$E'(\omega) = M_0 + \sum_{i=1}^{N} M_i \frac{\omega^2\tau_i^2}{1+\omega^2\tau_i^2} \tag{5.3}$$

$$E''(\omega) = \sum_{i=1}^{N} M_i \frac{\omega\tau_i}{1+\omega^2\tau_i^2}. \tag{5.4}$$

From here, it is now possible to choose N and fit a relaxation function to experimental data, then try to predict frequency response, or vice versa.

Similarly, we can construct DMA from creep for the isostress model (Prony series), which gives

$$\frac{E'}{E'^2 + E''^2} = J_0 + \sum_{i=1}^{N} \frac{J_i}{1+\omega^2\tau_i^2}$$

$$\frac{E''}{E'^2 + E''^2} = \sum_{i=1}^{N} \frac{J_i\omega\tau_i}{1+\omega^2\tau_i^2}.$$

This then matches the model used in literature [178].

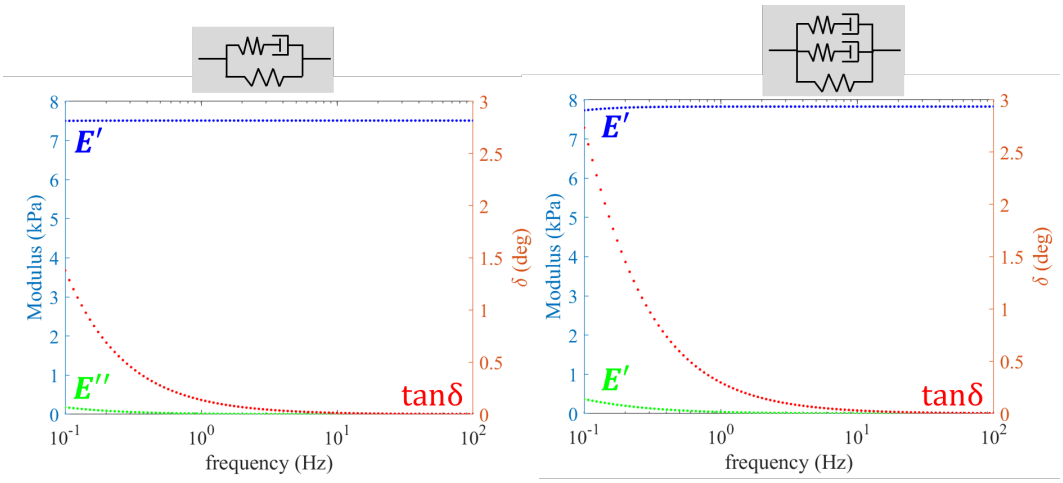

Figure 5.11: Theoretically predicted DMA results using stress-relaxation data.

The predicted E', E'', and $\tan\delta$ for the S3EM and S5EM from the mean values in Fig. 5.8 are plotted in Fig. 5.11. Depite small numerical differences, the two sets of results have similar trends, while the difference becomes nonnegligible at frequencies smaller than 1Hz, which is consistent with the 0.8s pulsing time. The difference coming from the two models largely lies in the second time constant in the S5EM, which captures material behavior at around 0.1Hz. The large similarities suggest that instead of using a theoretical model, it is possible to numerically integrate for predicted DMA results directly using the experimental data, without going through the fitting step. In tissue engineering, it is common to set the necessary number of elements by trial and error since biomaterials are often too complicated to pinpoint the exact nature of energy dissipation [185]. Models with more Maxwell elements were also evaluated, at which point no difference can be detected between the time constants within experimental error.

Preliminary DMA results for the jellyfish at 6 frequencies between 0.1Hz and 10Hz are plotted in Fig. 5.12 in comparison to that predicted from relaxation data with the same indentation depth and punch size. While the predicted results at the lower and higher ends match those experimentally collected within experimental error, there are large discrepancies at frequencies between 1Hz and 10Hz, which are the frequencies directly related to the pulsing time scale 0.8s. Unfortunately, the precision of the stress-relaxation tests are not high enough to resolve the 0.8s time scale, so to cross-validate the DMA data with relaxation results, it is necessary to increase data acquisition in relaxation in the initial 1s and to acquire DMA data at below 1Hz.

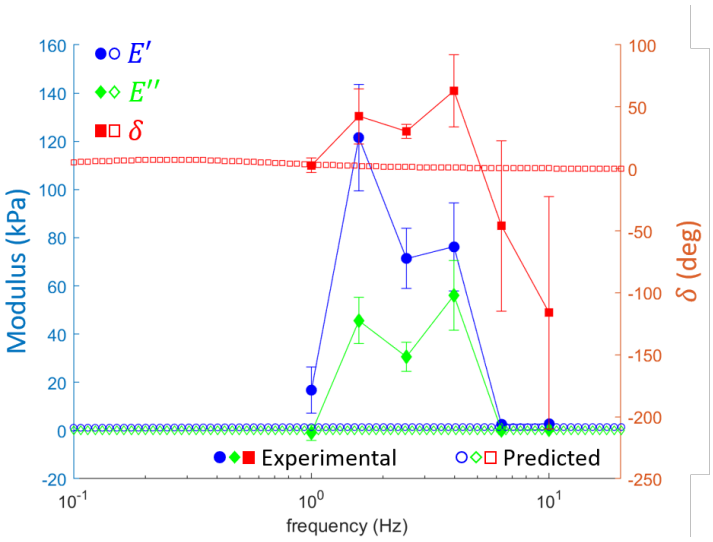

Figure 5.12: Comparison between experimentally measured DMA data and data theoretically predicted from stress-relaxation.

For "quasi-static" conventional indentation, we use a numerical integration using the measured displacement data to predict the theoretical load. Going from Eq. 5.1, substituting for the standard 5 element model (1 spring and 2 Maxwells), the predicted stress $\hat{\sigma}_j$ at a given measured strain data point ε_j is

$$\hat{\sigma}(t) = \int_{-\infty}^{t} \left(E_0 + E_1 e^{(t-\tau)/\tau_1} + E_2 e^{(t-\tau)/\tau_2}\right) \frac{\partial \varepsilon(\tau)}{\partial \tau} d\tau$$

$$\implies \hat{\sigma}_j = E_0 \varepsilon_j + \sum_{i=0}^{2} \sum_{k=2}^{j} \left(E_i e^{(t_j - \tau_k)/\tau_i} (\varepsilon_k - \varepsilon_{k-1})\right).$$

The resulting load-displacement "data" are compared to experimentally measured data (Fig. 5.13), where the overall shape and timescale of the load-hold-unload response can be captured. When examined closely, the numerically integrated data is concave during loading, while the experimental data hardens with increasing depth; while the holding and unloading segments of the red set of data match nicely, there are large discrepancies between the blue set of predicted and measured data. Implications on these discrepancies are discussed further in Section 5.4.

5.4 Discussion

Biological tissues in their hydrated form, such as cartilage, tendons, or Mesoglea, are a gellatinous matrix with pores filled with water, much like a dual-phase material. As the medium is deformed, the liquid diffuses throughout the material, often getting

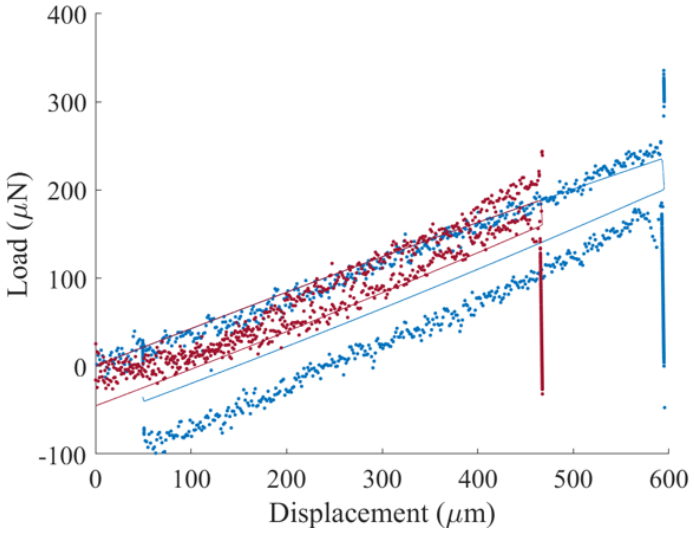

Figure 5.13: Comparison between experimental and theoretical "quasi-static" indentation response.

pushed out or pulled in as a result of the pressure change; this contributes to the mechanical response and adds another mechanism for energy dissipation, often evaluated through poroelastic models [186–188]. While we attempted at fitting to such a model, there was not sufficient evidence that it is suitable for our material; in addition, the viscoelastic nature of the gel matrix itself renders the material response complicated and hard to interpret [187–189]. Existing studies have shown that when the probed frequency is on par with the liquid equilibrium time (related to diffusivity), poroelastic models are significantly more accurate than viscoelastic models [190]. Linear viscoelasticity is mathematically simple and can substitute for the more complicated poroelastic models at other frequencies, and it was shown that the two can be separated when their time scales are different [191]. This could serve to explain the discrepancies in Fig. 5.12 at 1-10Hz, suggesting that the pulsing time is correlated with the water diffusivity time scale in the Mesoglea.

It is also necessary to discuss the implications of model accuracy, which could be an alternative reason for the discrepancies between experimental DMA data and data theoretically predicted in Fig. 5.12 and Fig. 5.13. Reasons contributing to model accuracy could entail diverse types of energy dissipation mechanisms with vairous time constants, nonlinearity, or a combination of the two. For the models to be accurate, fitting Eq. 5.3 to the storage data and Eq. 5.4 to the loss data from a single experiment should produce similar results for M_i and τ_i. However, as is shown in

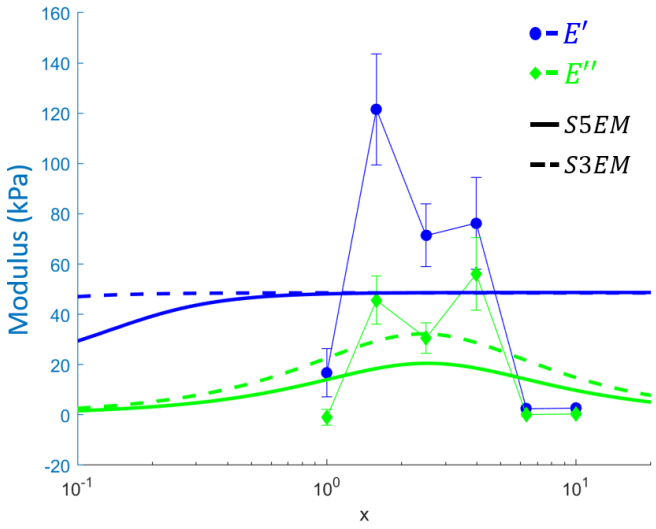

Figure 5.14: Fitting the S3EM and S5EM models to experimental DMA data.

Fig. 5.14, neither the S3EM or the S5EM can fully capture the peaks in both E' and E'', suggesting that there is large nonlinearity in the material that can not be fully captured using these standard linear models.

Throughout this chapter, we have treated Mesoglea as a homogeneous, isotropic material, which is not necessarity true or accurate given what we know of its microstructure. Collagen fibers are dispersed randomly throughout the gel, roughly $100\mu m$ apart; within the bulk of the gel, the fibers are oriented vertically, connecting the outer and inner surfaces of the bell; close to the surface, there are more densely packed collagen fibers forming a random network, giving stucture to the material [174, 175]. The mechanical properties of hydrated isolated collagen fibers has been under investigation for decades, with a plethora of disagreeing results [60, 62, 192–196], with the most recent studies concluding on Young's modulus of 300MPa [194], 123MPa [192], and 1.1MPa [60]. These large discrepancies highlight the difficulty of performing and analyzing high-precision in-solution mechanical experiments. Nevertheless, there is sufficient evidence to show that collagen fibers are orders of magnitude stiffer than its surrounding gel. In a compression-like geometry such as nanoindentation, collagen fibers likely buckle instead of stretch, which greatly softens their response to external load, likely constituting why we see no sign of stiffer signals from the indentation results shown in the previous sections. In the pulsing conditions that lead to shape recovery, collagen fiber networks undergo complex stress conditions that are not necessarily compression or tension, therefore

in an FEM model (which is what we are ultimately interested in), it is necessary to model the material with included collagen behavior, such as using embedded wire elements or a transversely anisotropic material input.

5.5 Summary

Viscoelasticity is hypothesized to consitute shape recovery in jellyfish. Using in-solution indentation, we capture stress-relaxation that descibes time-dependent material response of jellyfish Mesoglea under external loads in its natural ambient conditions. A 2 Maxwell element standard linear isostrain viscoelastic model (S5EM) was found to best fit the relaxation data, while predicted quasistatic indentation matches the data experimentally measured. Discrepancies between predicted DMA data and experiments suggest water diffusivity time-scales within the frequency range of interest as well as potential nonlinearity of the viscoelasticity in the material, which needs to be further evaluated to separate their effects. Lengthscales in this work approach that of collagen fibers, a major constituent of Mesoglea, which renders the material anisotropic, necessitating the incorporation of collagen behavior in FEM models in the future.

Chapter 6

CONCLUSIONS AND OUTLOOK

In-situ nanomechanical experiments open new doors to both understanding fundamental deformation mechanisms at the relevant lengthscales of material microstructures and providing guidance of designing artificial materials with superior properties. While recent development in both the instrumental techniques and the diversity of materials have significantly strengthened the microstructure-mechanics relationship, there remain unanswered questions at each important lengthscale pertaining to the crystal structure, defect-dominated plasticity, composite constituents, and features in cellular solids. Using *in-situ* experiments as a tool and tapping into the pool of existing knowledge, we tackled these specific challenges and shed light on some long-lasting mysteries.

In Chapter 2, we explored the improved shape memory effect in a ceramic using theories initially developed for metals. The microstructure characterization and mechanical analysis combined demonstrated that the shape memory performance can be tuned through minimizing thermal hysteresis, enabling a new SMC with pseudoplastic strains comparable to that in metallic SMAs. Since the functionality is limited to single crystals/grains, the scalability of this material heavily depends on the grain boundary effects. Preliminary results have shown that its grain boundaries are rigid and do not allow transfer of deformation like in ductile metals, therefore preventing successful fabrication of polycrystalline SMC using the current material system at the current stage. While efforts are being made to fabricate large, scalable single crystals, an alternative route would be to consider grain boundary engineering, allowing for ductile grain boundaries rather than brittle amorphous regions between grains.

Chapter 3 further investigates the size-effect of twinning yield stress for the ceramic, revealing a universal scaling law that captures both twinning and slip behavior. This serves as supporting evidence for the Matthew's CTT, which can be argued (to some level of controversy) to be the all-encompassing model that describes size-dependence in dislocation-governed plasticity. Since the CTT can only be probed in the absence of strain hardening, deformation twinning, with its restricted glide planes, serves as a clean alternative to exploring the physical origins of the size-

effect. This conclusion can be further strengthened by more studies on a diverse set of crystal structures and bond types that deform via twinning, much like what was done for dislocation slip in the 2005-2010 period.

Chapter 4 continues to climb the lengthscale ladder to a fiber-infused bio-composite: Scorpion pincer cuticles. With the help of Synchrotron radiation, the stiffness and deformation mechanism of two regions were related to their corresponding fiber structure. More data are underway for statistical robustness, while the exact role of the two types of structures are still under question. Quantitative fracture analysis is necessary to identify the direct competition between the two microstructures in the load-bearing functions of the overall organ as a whole, while more in-depth FEA could shed some light on the logic behind the observed tension-compression asymmetry. The newly deciphered principles pave the way to designing bio-inspired additively manufactured 3D materials with tuned toughness/strength profiles.

In Chapter 5, we return to indentation, adapted to accommodate in-solution testing, for the characterization of jellyfish, revealing two time scales in its viscoelastic behavior and frequency dependence that can only be described via combined poroelastic/viscoelastic behavior. While further theoretical analysis could either prove or debunk the accuracy of a generalized poroelastic model, high quality systematic data using different size tips are necessary for repeatability. Since the collagen fibers are nonnegligible, they can be incorporated and examined first through an inverse problem FEA to recreate indentation results, then used to simulate observed jellyfish recovery through muscle contractions.

This work explores the lengthscales bridging the gap between an atomic level phenomenon and macroscopic material behavior, deciphering different ways nature has adopted to mitigate stress and damage at each level along the way. While the scope of this work ends here, the efforts of exploring deeper into each of these lengthscales or of filling the gaps in between does not need to. A natural extension on this work that ties back to the Martensitic Transformation in Chapter 2 is to study phase transformation in lattices. This can open an opportunity of achieving shape memory using any otherwise monolithic material with thermal expansion properties. While there are some published shape memory 2D metamaterials works [68] and similar concepts using functional materials [8], recreating Martensitic transformation in 3D through thermal treatment alone proves to be difficult, since it relies on the design of a clever lattice structure that can be deformed into a mirrored orientation without changing the energy landscape. One potential solution

is using carefully designed local heat-induced buckling that can generate a global deformation. By combining optimized atomic phenomenon and newly developed engineering capabilities, we hope to pave the road to the design of optimized structural materials.

BIBLIOGRAPHY

1. Oliver, W C and G M Pharr (1992). *An improved technique for determining hardness and elastic modulus using load and displacement sensing indentation experiments*. DOI: 10.1557/JMR.1992.1564. URL: http://www.journals.cambridge.org/abstract%7B%5C%%7D7B%7B%5C_%7D%7B%5C%%7D7DS0884291400017039.

2. Pharr, G. M. and W. C. Oliver (1992). "Measurement of Thin Film Mechanical Properties Using Nanoindentation". In: *MRS Bulletin* 17.7, pp. 28–33. ISSN: 19381425. DOI: 10.1557/S0883769400041634.

3. Greer, Julia R., Warren C. Oliver, and William D. Nix (2005). "Size dependence of mechanical properties of gold at the micron scale in the absence of strain gradients". In: *Acta Materialia* 53.6, pp. 1821–1830. ISSN: 13596454. DOI: 10.1016/j.actamat.2004.12.031.

4. Jennings, Andrew T. and Julia R. Greer (2011). "Tensile deformation of electroplated copper nanopillars". In: *Philosophical Magazine* 91.7-9, pp. 1108–1120. ISSN: 14786435. DOI: 10.1080/14786435.2010.505180.

5. Ni, Xiaoyue et al. (2019). "Yield Precursor Dislocation Avalanches in Small Crystals: The Irreversibility Transition". In: *Physical Review Letters* 123.3, pp. 1–11. ISSN: 10797114. DOI: 10.1103/PhysRevLett.123.035501.

6. Gu, X. Wendy et al. (2013). "Microstructure versus flaw: Mechanisms of failure and strength in nanostructures". In: *Nano Letters* 13.11, pp. 5703–5709. ISSN: 15306984. DOI: 10.1021/nl403453h.

7. Cui, Fiona Yuwei and Richard P. Vinci (2017). "A chevron-notched bowtie micro-beam bend test for fracture toughness measurement of brittle materials". In: *Scripta Materialia*. ISSN: 13596462. DOI: 10.1016/j.scriptamat.2017.01.031.

8. Xia, Xiaoxing et al. (2019). "Electrochemically reconfigurable architected materials". In: *Nature*. ISSN: 14764687. DOI: 10.1038/s41586-019-1538-z.

9. Jin, Hai Jun et al. (2009). "Deforming nanoporous metal: Role of lattice coherency". In: *Acta Materialia* 57.9, pp. 2665–2672. ISSN: 13596454. DOI: 10.1016/j.actamat.2009.02.017.

10. Lee, Subin et al. (2014). "Reversible cyclic deformation mechanism of gold nanowires by twinning-detwinning transition evidenced from in situ TEM". In: *Nature Communications* 5, pp. 1–10. ISSN: 20411723. DOI: 10.1038/ncomms4033.

11. Wendy Gu, X. and Julia R. Greer (2015). “Ultra-strong architected Cu meso-lattices”. In: *Extreme Mechanics Letters*. ISSN: 23524316. DOI: 10.1016/j.eml.2015.01.006.

12. Kim, Ju Young, Dongchan Jang, and Julia R. Greer (2011). “Nanolaminates utilizing size-dependent homogeneous plasticity of metallic glasses”. In: *Advanced Functional Materials* 21.23, pp. 4550–4554. ISSN: 1616301X. DOI: 10.1002/adfm.201101164.

13. Tertuliano, Ottman A. and Julia R. Greer (2016). “The nanocomposite nature of bone drives its strength and damage resistance”. In: *Nature Materials*. ISSN: 14764660. DOI: 10.1038/nmat4719.

14. Meza, Lucas R. et al. (2017). “Reexamining the mechanical property space of three-dimensional lattice architectures”. In: *Acta Materialia* 140, pp. 424–432. ISSN: 13596454. DOI: 10.1016/j.actamat.2017.08.052. URL: https://doi.org/10.1016/j.actamat.2017.08.052.

15. Xu, Chen et al. (2017). “Enhanced strength and temperature dependence of mechanical properties of Li at small scales and its implications for Li metal anodes”. In: *Proceedings of the National Academy of Sciences of the United States of America*. ISSN: 10916490. DOI: 10.1073/pnas.1615733114.

16. Liontas, Rachel et al. (2016). “Substantial tensile ductility in sputtered Zr-Ni-Al nano-sized metallic glass”. In: *Acta Materialia*. ISSN: 13596454. DOI: 10.1016/j.actamat.2016.07.050.

17. Aitken, Zachary H. et al. (2016). “Microstructure provides insights into evolutionary design and resilience of Coscinodiscus sp. frustule”. In: *Proceedings of the National Academy of Sciences of the United States of America* 113.8, pp. 2017–2022. ISSN: 10916490. DOI: 10.1073/pnas.1519790113.

18. Giwa, Adenike M. et al. (2020). “Effect of temperature on small-scale deformation of individual face-centered-cubic and body-centered-cubic phases of an Al0.7CoCrFeNi high-entropy alloy”. In: *Materials and Design*. ISSN: 18734197. DOI: 10.1016/j.matdes.2020.108611.

19. Meza, Lucas R. and Julia R. Greer (2014). “Mechanical characterization of hollow ceramic nanolattices”. In: *Journal of Materials Science*. ISSN: 00222461. DOI: 10.1007/s10853-013-7945-x.

20. Ni, Xiaoyue et al. (2016). “Exceptional Resilience of Small-Scale Au30Cu25Zn45 under Cyclic Stress-Induced Phase Transformation”. In: *Nano Letters* 16.12, pp. 7621–7625. ISSN: 15306992. DOI: 10.1021/acs.nanolett.6b03555.

21. Tertuliano, Ottman A (2019). “Small-scale Deformation and Fracture of Hard Biomaterials”. In: p. 90.

22. Zhang, Haolu, Justin Jetter, Hanlin Gu, Richard D. James, Eckhard Quandt, and Julia R. Greer (2021). "Size-dependence of zirconia-based ceramics via deformaton twinning." In: *Extreme Mechanics Letters* 42, p. 101124. DOI: 10.1016/j.eml.2020.101124.

23. Zhang, Haolu, Israel Kellersztein, Rebecca A. Gallivan, H. Daniel Wagner, and Julia R. Greer (n.d.). "Microstructure enabled fracture resistance in Scorpio Maurus Palmatus cuticles." In: *In Preparation* ().

24. Östlund, Fredrik et al. (2011). "Ductile-brittle transition in micropillar compression of GaAs at room temperature". In: *Philosophical Magazine* 91.7-9, pp. 1190–1199. ISSN: 14786435. DOI: 10.1080/14786435.2010.509286.

25. Luo, Junhang et al. (2016). "Size-Dependent Brittle-to-Ductile Transition in Silica Glass Nanofibers". In: *Nano Letters* 16.1, pp. 105–113. ISSN: 15306992. DOI: 10.1021/acs.nanolett.5b03070.

26. Li, Rong and K. Sieradzki (1992). "Ductile-brittle transition in random porous Au". In: *Physical Review Letters* 68.8, pp. 1168–1171. ISSN: 00319007. DOI: 10.1103/PhysRevLett.68.1168.

27. Greer, Julia R. and Jeff Th M. De Hosson (2011). "Plasticity in small-sized metallic systems: Intrinsic versus extrinsic size effect". In: *Progress in Materials Science* 56.6, pp. 654–724. ISSN: 00796425. DOI: 10.1016/j.pmatsci.2011.01.005. URL: http://dx.doi.org/10.1016/j.pmatsci.2011.01.005.

28. Portela, Carlos M., Julia R. Greer, and Dennis M. Kochmann (2018). "Impact of node geometry on the effective stiffness of non-slender three-dimensional truss lattice architectures". In: *Extreme Mechanics Letters*. ISSN: 23524316. DOI: 10.1016/j.eml.2018.06.004.

29. Portela, Carlos M. et al. (2020). "Extreme mechanical resilience of self-assembled nanolabyrinthine materials". In: *Proceedings of the National Academy of Sciences of the United States of America*. ISSN: 10916490. DOI: 10.1073/pnas.1916817117.

30. Lin, Albert Yu Min and Marc André Meyers (2009). "Interfacial shear strength in abalone nacre". In: *Journal of the Mechanical Behavior of Biomedical Materials* 2.6, pp. 607–612. ISSN: 17516161. DOI: 10.1016/j.jmbbm.2009.04.003. URL: http://dx.doi.org/10.1016/j.jmbbm.2009.04.003.

31. Maaß, R. and P. M. Derlet (2018). "Micro-plasticity and recent insights from intermittent and small-scale plasticity". In: *Acta Materialia* 143, pp. 338–363. ISSN: 13596454. DOI: 10.1016/j.actamat.2017.06.023. URL: https://doi.org/10.1016/j.actamat.2017.06.023.

32. Moestopo, Widianto P. et al. (2020). “Pushing and Pulling on Ropes: Hierarchical Woven Materials”. In: *Advanced Science*. ISSN: 21983844. DOI: 10.1002/advs.202001271.

33. Bhattacharya, Kaushik et al. (2004). “Crystal symmetry and the reversibility of martensitic transformations”. In: *Nature*. ISSN: 00280836. DOI: 10.1038/nature02378.

34. San Juan, J. and M. L. Nó (2013). “Superelasticity and shape memory at nanoscale: Size effects on the martensitic transformation”. In: *Journal of Alloys and Compounds* 577.SUPPL. 1, pp. 25–29. ISSN: 09258388. DOI: 10.1016/j.jallcom.2011.10.110.

35. Chen, Xian et al. (2013). “Study of the cofactor conditions: Conditions of supercompatibility between phases”. In: *Journal of the Mechanics and Physics of Solids* 61.12, pp. 2566–2587. ISSN: 00225096. DOI: 10.1016/j.jmps.2013.08.004. arXiv: 1307.5930. URL: http://dx.doi.org/10.1016/j.jmps.2013.08.004.

36. Song, Yintao et al. (2013). “Enhanced reversibility and unusual microstructure of a phase-transforming material”. In: *Nature* 502.7469, pp. 85–88. ISSN: 00280836. DOI: 10.1038/nature12532. URL: http://dx.doi.org/10.1038/nature12532.

37. Zeng, Xiaomei et al. (2017a). “Enhanced shape memory and superelasticity in small-volume ceramics: A perspective on the controlling factors”. In: *MRS Communications* 7.4, pp. 747–754. ISSN: 21596867. DOI: 10.1557/mrc.2017.99.

38. Du, Zehui et al. (2017). “Superelasticity in micro-scale shape memory ceramic particles”. In: *Acta Materialia* 123, pp. 255–263. ISSN: 13596454. DOI: 10.1016/j.actamat.2016.10.047.

39. Zeng, Xiao Mei et al. (2016). “Crystal orientation dependence of the stress-induced martensitic transformation in zirconia-based shape memory ceramics”. In: *Acta Materialia* 116, pp. 124–135. ISSN: 13596454. DOI: 10.1016/j.actamat.2016.06.030. URL: http://dx.doi.org/10.1016/j.actamat.2016.06.030.

40. Pang, Edward L., Caitlin A. McCandler, and Cristopher A. Schuh (n.d.). “Reduced cracking in polycrystalline ZrO 2 -CeO 2 shape- memory ceramics by meeting the cofactor conditions”. In: *Acta Materialia* ().

41. Uchic, Michael D. et al. (2004). “Sample dimensions influence strength and crystal plasticity”. In: *Science* 305.5686, pp. 986–989. ISSN: 00368075. DOI: 10.1126/science.1098993.

42. Kim, Ju Young, Dongchan Jang, and Julia R. Greer (2010). "Tensile and compressive behavior of tungsten, molybdenum, tantalum and niobium at the nanoscale". In: *Acta Materialia* 58.7, pp. 2355–2363. ISSN: 13596454. DOI: 10.1016/j.actamat.2009.12.022. URL: http://dx.doi.org/10.1016/j.actamat.2009.12.022.

43. Korte, S. and W. J. Clegg (2011). "Discussion of the dependence of the effect of size on the yield stress in hard materials studied by microcompression of MgO". In: *Philosophical Magazine* 91.7-9, pp. 1150–1162. ISSN: 14786435. DOI: 10.1080/14786435.2010.505179.

44. Östlund, Fredrik et al. (2009). "Brittle-to-ductile transition in uniaxial compression of silicon pillars at room temperature". In: *Advanced Functional Materials* 19.15, pp. 2439–2444. ISSN: 1616301X. DOI: 10.1002/adfm.200900418.

45. Rao, S. I. et al. (2008). "Athermal mechanisms of size-dependent crystal flow gleaned from three-dimensional discrete dislocation simulations". In: *Acta Materialia* 56.13, pp. 3245–3259. ISSN: 13596454. DOI: 10.1016/j.actamat.2008.03.011.

46. Dimiduk, Dennis M et al. (2006). "Scale-free intermittent flow in Crystal Plasticity". In: *Science* 312, pp. 1188–1190. DOI: 10.1126/science.1123889.

47. Maaß, R. et al. (2015). "Slip statistics of dislocation avalanches under different loading modes". In: *Physical Review E - Statistical, Nonlinear, and Soft Matter Physics* 91.4, pp. 1–8. ISSN: 15502376. DOI: 10.1103/PhysRevE.91.042403.

48. Csikor, Ferenc F. et al. (2012). "Dislocation Avalanches, Strain Bursts, and the Problem of Plastic Forming at the Micrometer Scale". In: *Science* 318.October, pp. 251–254.

49. Fisher, Daniel S. (1998). "Collective transport in random media: From superconductors to earthquakes". In: *Physics Report* 301.1-3, pp. 113–150. ISSN: 03701573. DOI: 10.1016/S0370-1573(98)00008-8. arXiv: 9711179 [cond-mat].

50. Dahmen, Karin A., Yehuda Ben-Zion, and Jonathan T. Uhl (2011). "A simple analytic theory for the statistics of avalanches in sheared granular materials". In: *Nature Physics*. ISSN: 17452481. DOI: 10.1038/nphys1957.

51. Corté, Laurent et al. (2008). "Random organization in periodically driven systems". In: *Nature Physics* 4.5, pp. 420–424. ISSN: 17452481. DOI: 10.1038/nphys891.

52. Ni, Xiaoyue et al. (2017). "Probing Microplasticity in Small-Scale FCC Crystals via Dynamic Mechanical Analysis". In: *Physical Review Letters*. ISSN: 10797114. DOI: 10.1103/PhysRevLett.118.155501. arXiv: 1612.09011.

53. Sethna, James P., Karin A. Dahmen, and Christopher R. Myers (2001). *Crackling noise*. DOI: 10.1038/35065675.

54. Fleck, N. A. et al. (1994). "Strain gradient plasticity: Theory and experiment". In: *Acta Metallurgica Et Materialia*. ISSN: 09567151. DOI: 10.1016/0956-7151(94)90502-9.

55. Fleck, N. A., M. F. Ashby, and J. W. Hutchinson (2003). "The role of geometrically necessary dislocations in giving material strengthening". In: *Scripta Materialia*. ISSN: 13596462. DOI: 10.1016/S1359-6462(02)00338-X.

56. Dunstan, D. J. and A. J. Bushby (2013). "The scaling exponent in the size effect of small scale plastic deformation". In: *International Journal of Plasticity* 40, pp. 152–162. ISSN: 07496419. DOI: 10.1016/j.ijplas.2012.08.002. URL: http://dx.doi.org/10.1016/j.ijplas.2012.08.002.

57. Dunstan, David J. (2017). "The size effect in the mechanical strength of semiconductors and metals: Strain relaxation by dislocation-mediated plastic deformation". In: *Journal of Materials Research* 32.21, pp. 4041–4053. ISSN: 20445326. DOI: 10.1557/jmr.2017.300.

58. Politi, Yael, Benny Bar-On, and Helge Otto Fabritius (2019). *Mechanics of arthropod cuticle-versatility by structural and compositional variation*. Vol. 282, pp. 287–327. ISBN: 9783030119423. DOI: 10.1007/978-3-030-11942-3_10.

59. Meyers, Marc André et al. (2008). *Biological materials: Structure and mechanical properties*. DOI: 10.1016/j.pmatsci.2007.05.002.

60. Jansen, Karin A et al. (2018). "The Role of Network Architecture in Collagen Mechanics". In: *Biophysical Journal* 114.11, pp. 2665–2678. ISSN: 0006-3495. DOI: 10.1016/j.bpj.2018.04.043. URL: https://doi.org/10.1016/j.bpj.2018.04.043.

61. Nikolov, Svetoslav et al. (2010). "Revealing the design principles of high-performance biological composites using Ab initio and multiscale simulations: The example of lobster cuticle". In: *Advanced Materials* 22.4, pp. 519–526. ISSN: 09359648. DOI: 10.1002/adma.200902019.

62. P., Fratzl et al. (1997). "Fibrillar Structure and Mechanical Properties of Collagen". In: *Journal of Structural Biology* 122, pp. 119–122.

63. Meyers, Marc Andre, Joanna McKittrick, and Po-Yu Chen (2013). "Structural Biological Materials: Critical Mechanics-Materials Connections". In: *Science* 339.February, pp. 773–780.

64. Cao, Keqin et al. (2013). "Reactive aramid nanostructures as high-performance polymeric building blocks for advanced composites". In: *Advanced Functional Materials*. ISSN: 1616301X. DOI: 10.1002/adfm.201202466.

65. Grunenfelder, L. K. et al. (2014). “Bio-inspired impact-resistant composites”. In: *Acta Biomaterialia* 10.9, pp. 3997–4008. ISSN: 18787568. DOI: 10.1016/j.actbio.2014.03.022. URL: http://dx.doi.org/10.1016/j.actbio.2014.03.022.

66. Montemayor, Lauren C., Lucas R. Meza, and Julia R. Greer (2014). “Design and fabrication of hollow rigid nanolattices via two-photon lithography”. In: *Advanced Engineering Materials*. ISSN: 14381656. DOI: 10.1002/adem.201300254.

67. Mateos, Arturo J. et al. (2019). “Discrete-Continuum Duality of Architected Materials: Failure, Flaws, and Fracture”. In: *Advanced Functional Materials* 29.5, pp. 1–7. ISSN: 16163028. DOI: 10.1002/adfm.201806772.

68. Yang, Dian et al. (2015). “Phase-transforming and switchable metamaterials”. In: *Extreme Mechanics Letters* 6.1, pp. 1–9. DOI: 10.1016/j.eml.2015.11.004. URL: http://dx.doi.org/10.1016/j.eml.2015.11.004.

69. Oliver, W. C., R. Hutchings, and J. B. Pethica (1985). “MEASUREMENT OF HARDNESS AT INDENTATION DEPTHS AS LOW AS 20 NANOMETRES.” In: *ASTM Special Technical Publication*. ISBN: 0803104413. DOI: 10.1520/stp32953s.

70. Nix, William D. and Huajian Gao (1998). “Indentation size effects in crystalline materials: A law for strain gradient plasticity”. In: *Journal of the Mechanics and Physics of Solids*. ISSN: 00225096. DOI: 10.1016/S0022-5096(97)00086-0.

71. El-Awady, Jaafar A. et al. (2009). “Effects of focused ion beam induced damage on the plasticity of micropillars”. In: *Physical Review B - Condensed Matter and Materials Physics* 80.10, pp. 1–5. ISSN: 10980121. DOI: 10.1103/PhysRevB.80.104104.

72. Weissmüller, Jörg et al. (2009). “Nanoporous metals by alloy corrosion: Formation and mechanical properties”. In: *MRS Bulletin* 34.8, pp. 577–586. ISSN: 08837694. DOI: 10.1557/mrs2009.157.

73. Phani, P. Sudharshan and W. C. Oliver (2016). “A direct comparison of high temperature nanoindentation creep and uniaxial creep measurements for commercial purity aluminum”. In: *Acta Materialia*. ISSN: 13596454. DOI: 10.1016/j.actamat.2016.03.032.

74. Grosso, Robson L. et al. (2020). “In Situ Transmission Electron Microscopy for Ultrahigh Temperature Mechanical Testing of ZrO2”. In: *Nano Letters*. ISSN: 15306992. DOI: 10.1021/acs.nanolett.9b04205.

75. Wang, Q. Z. et al. (2018). “Scrutinized and revised stress intensity factor formulas for double cleavage drilled compression specimens”. In: *Theoretical and Applied Fracture Mechanics* 96.September, pp. 803–810. ISSN: 01678442. DOI: 10.1016/j.tafmec.2017.11.008.

76. Chen, Z. et al. (2018). “High-Resolution Deformation Mapping Across Large Fields of View Using Scanning Electron Microscopy and Digital Image Correlation”. In: *Experimental Mechanics* 58.9, pp. 1407–1421. ISSN: 17412765. DOI: 10.1007/s11340-018-0419-y.

77. James, R. D. and K. F. Hane (2000). “Martensitic transformations and shape-memory materials”. In: *Acta Materialia*. ISSN: 13596454. DOI: 10.1016/S1359-6454(99)00295-5.

78. Lai, Alan et al. (2013). “Shape memory and superelastic ceramics at small scales”. In: *Science* 341.6153, pp. 1505–1508. ISSN: 10959203. DOI: 10.1126/science.1239745.

79. Behl, Marc, Muhammad Yasar Razzaq, and Andreas Lendlein (2010). *Multifunctional shape-memory polymers*. DOI: 10.1002/adma.200904447.

80. Chimowitz, Marc I. et al. (2011). “Stenting versus Aggressive Medical Therapy for Intracranial Arterial Stenosis”. In: *New England Journal of Medicine*. ISSN: 0028-4793. DOI: 10.1056/nejmoa1105335.

81. Duerig, T., A. Pelton, and D. Stöckel (1999). “An overview of nitinol medical applications”. In: *Materials Science and Engineering A*. ISSN: 09215093. DOI: 10.1016/s0921-5093(99)00294-4.

82. Hornbogen, E. (2004). *Review Thermo-mechanical fatigue of shape memory alloys*. DOI: 10.1023/B:JMSC.0000011492.88523.d3.

83. Norfleet, D. M. et al. (2009). “Transformation-induced plasticity during pseudoelastic deformation in Ni-Ti microcrystals”. In: *Acta Materialia* 57.12, pp. 3549–3561. ISSN: 13596454. DOI: 10.1016/j.actamat.2009.04.009. URL: http://dx.doi.org/10.1016/j.actamat.2009.04.009.

84. Cui, Jun et al. (2006). “Combinatorial search of thermoelastic shape-memory alloys with extremely small hysteresis width”. In: *Nature Materials*. ISSN: 14764660. DOI: 10.1038/nmat1593.

85. Gu, Hanlin et al. (2018). *Phase engineering and supercompatibility of shape memory alloys*. DOI: 10.1016/j.mattod.2017.10.002.

86. Swain, M. V. (1986). “Shape memory behaviour in partially stabilized zirconia ceramics”. In: *Nature*. ISSN: 00280836. DOI: 10.1038/322234a0.

87. Shian, Samuel et al. (2014). “The tetragonal-monoclinic, ferroelastic transformation in yttrium tantalate and effect of zirconia alloying”. In: *Acta Materialia*. ISSN: 13596454. DOI: 10.1016/j.actamat.2014.01.054.

88. Yashima, Masatomo et al. (1995). “Tetragonal—Monoclinic Phase Transition Enthalpy and Temperature of ZrO2-CeO2 Solid Solutions”. In: *Journal of the American Ceramic Society*. ISSN: 15512916. DOI: 10.1111/j.1151-2916.1995.tb08642.x.

89. Li, Ping, I-Wei -W Chen, and James E. Penner-Hahn (1994). “Effect of Dopants on Zirconia Stabilization—An X-ray Absorption Study: I, Trivalent Dopants”. In: *Journal of the American Ceramic Society*. ISSN: 15512916. DOI: 10.1111/j.1151-2916.1994.tb06964.x.

90. Jetter, J. et al. (2019). “Tuning crystallographic compatibility to enhance shape memory in ceramics”. In: *Physical Review Materials* 3.9, p. 093603. ISSN: 24759953. DOI: 10.1103/PhysRevMaterials.3.093603.

91. Chevalier, Jérôme et al. (2009). “The tetragonal-monoclinic transformation in zirconia: Lessons learned and future trends”. In: *Journal of the American Ceramic Society* 92.9, pp. 1901–1920. ISSN: 00027820. DOI: 10.1111/j.1551-2916.2009.03278.x.

92. Bischoff, Ewald and Manfred Ruhle (1982). “Twin Boundaries in Monoclinic ZrO2 Particles Confined in a Mullite Matrix”. In: *Journal of the American Ceramic Society* 66.2, pp. 123–127. ISSN: 1359-0286. DOI: 10.1016/j.cossms.2010.07.001. URL: http://dx.doi.org/10.1016/j.cossms.2010.07.001.

93. Igawa, Naoki and Yoshinobu Ishii (2001). “Crystal Structure of Metastable Tetragonal Zirconia up to 1473 K”. In: *Journal of the American Ceramic Society* 84.5, pp. 1169–1171. ISSN: 00027820. DOI: 10.1111/j.1151-2916.2001.tb00808.x.

94. Ocelík, V. et al. (2017). “On the bulk degradation of yttria-stabilized nanocrystalline zirconia dental implant abutments: an electron backscatter diffraction study”. In: *Journal of Materials Science: Materials in Medicine* 28.8, pp. 1–10. ISSN: 15734838. DOI: 10.1007/s10856-017-5927-2. URL: http://dx.doi.org/10.1007/s10856-017-5927-2.

95. Ruhle, M et al. (1988). “TEM Studies on Phases and Phase Stabilities of Zirconia Ceramics”. In: *Physica B* 150, pp. 86–98.

96. Sneddon, Ian N. (n.d.). “The relation between load and penetration in the axisymmetric boussinesq problem for a punch of arbitrary profile”. In: *International Journal of Engineering Sciences* 3.1 (), pp. 47–57.

97. Miyazaki, S. et al. (1984). “The habit plane and transformation strains associated with the martensitic transformation in Ti-Ni single crystals”. In: *Scripta Metallurgica* 18.9, pp. 883–888. ISSN: 00369748. DOI: 10.1016/0036-9748(84)90254-0.

98. Tan, Geraldine and Yinong Liu (2004). "Comparative study of deformation-induced martensite stabilisation via martensite reorientation and stress-induced martensitic transformation in NiTi". In: *Intermetallics* 12.4, pp. 373–381. ISSN: 09669795. DOI: 10.1016/j.intermet.2003.11.008.

99. Kang, Guozheng et al. (2009). "Ratchetting deformation of super-elastic and shape-memory NiTi alloys". In: *Mechanics of Materials* 41.2, pp. 139–153. ISSN: 01676636. DOI: 10.1016/j.mechmat.2008.09.001. URL: http://dx.doi.org/10.1016/j.mechmat.2008.09.001.

100. Csikor, Ferenc F. et al. (2007). "Dislocation avalanches, strain bursts, and the problem of plastic forming at the micrometer scale". In: *Science* 318.5848, pp. 251–254. ISSN: 00368075. DOI: 10.1126/science.1143719.

101. Zeng, Xiao Mei et al. (2017b). "In-situ studies on martensitic transformation and high-temperature shape memory in small volume zirconia". In: *Acta Materialia* 134, pp. 257–266. ISSN: 13596454. DOI: 10.1016/j.actamat.2017.06.006. URL: http://dx.doi.org/10.1016/j.actamat.2017.06.006.

102. Beake, Ben D. and James F. Smith (2002). "High-temperature nanoindentation testing of fused silica and other materials". In: *Philosophical Magazine A: Physics of Condensed Matter, Structure, Defects and Mechanical Properties*. ISSN: 01418610. DOI: 10.1080/01418610208235727.

103. Koch, Susanne et al. (2015). "A high temperature nanoindentation study of Al-Cu wrought alloy". In: *Materials Science and Engineering A* 644, pp. 218–224. ISSN: 09215093. DOI: 10.1016/j.msea.2015.07.066. URL: http://dx.doi.org/10.1016/j.msea.2015.07.066.

104. Beake, Ben D. and Adrian J. Harris (2019). "Nanomechanics to 1000°C for high temperature mechanical properties of bulk materials and hard coatings". In: *Vacuum* 159.October 2018, pp. 17–28. ISSN: 0042207X. DOI: 10.1016/j.vacuum.2018.10.011. URL: https://doi.org/10.1016/j.vacuum.2018.10.011.

105. Huang, J. Y. et al. (2006). "Kink formation and motion in carbon nanotubes at high temperatures". In: *Physical Review Letters* 97.7, pp. 18–21. ISSN: 00319007. DOI: 10.1103/PhysRevLett.97.075501.

106. Fu, Y. Q. et al. (2008). "In-situ observation of transition between surface relief and wrinkling in thin film shape memory alloys". In: *Journal of Nanoscience and Nanotechnology*. DOI: 10.1166/jnn.2008.630.

107. Falk, Wayne and Richard D. James (2006). "Elasticity theory for self-assembled protein lattices with application to the martensitic phase transition in bacteriophage T4 tail sheath". In: *Physical Review E - Statistical, Nonlinear, and Soft Matter Physics* 73.1, pp. 1–23. ISSN: 15393755. DOI: 10.1103/PhysRevE.73.011917. arXiv: 0509083 [physics].

108. Jennings, Andrew T., Michael J. Burek, and Julia R. Greer (2010). "Microstructure versus Size: Mechanical properties of electroplated single crystalline Cu nanopillars". In: *Physical Review Letters* 104.13, pp. 1–4. ISSN: 00319007. DOI: 10.1103/PhysRevLett.104.135503.

109. Ye, Jia et al. (2011). "In situ TEM compression testing of Mg and Mg-0.2 wt.% Ce single crystals". In: *Scripta Materialia* 64.3, pp. 292–295. ISSN: 13596462. DOI: 10.1016/j.scriptamat.2010.09.047. URL: http://dx.doi.org/10.1016/j.scriptamat.2010.09.047.

110. Schneider, A. S. et al. (2009). "Correlation between critical temperature and strength of small-scale bcc pillars". In: *Physical Review Letters* 103.10, p. 105501. ISSN: 00319007. DOI: 10.1103/PhysRevLett.103.105501.

111. Dunstan, D. J., S. Young, and R. H. Dixon (1991). "Geometrical theory of critical thickness and relaxation in strained-layer growth". In: *Journal of Applied Physics* 70.6, pp. 3038–3045. ISSN: 00218979. DOI: 10.1063/1.349335.

112. Matthews, J. W. and A. E. Blakeslee (1974). "Defects in epitaxial multilayers: I. Misfit dislocations". In: *Journal of Crystal Growth* 27, pp. 118–125. ISSN: 00220248. DOI: 10.1016/S0022-0248(74)80055-2.

113. Yu, Qian et al. (2010). "Strong crystal size effect on deformation twinning". In: *Nature* 463.7279, pp. 335–338. ISSN: 00280836. DOI: 10.1038/nature08692.

114. Wang, Jiangwei et al. (2015). "In situ atomic-scale observation of twinning-dominated deformation in nanoscale body-centred cubic tungsten". In: *Nature Materials* 14.6, pp. 594–600. ISSN: 14764660. DOI: 10.1038/nmat4228.

115. Li, Xiaoyan et al. (2010). "Dislocation nucleation governed softening and maximum strength in nano-twinned metals". In: *Nature* 464.7290, pp. 877–880. ISSN: 00280836. DOI: 10.1038/nature08929.

116. Liao, X. Z. et al. (2004). "Deformation twinning in nanocrystalline copper at room temperature and low strain rate". In: *Applied Physics Letters* 84.4, p. 592. ISSN: 00036951. DOI: 10.1063/1.1644051.

117. Lu, K., L. Lu, and S. Suresh (2009). "Strengthening materials by engineering coherent internal boundaries at the nanoscale". In: *Science* 324.5925, pp. 349–352. ISSN: 00368075. DOI: 10.1126/science.1159610.

118. Brown, D. W. et al. (2005). "Internal strain and texture evolution during deformation twinning in magnesium". In: *Materials Science and Engineering A* 399.1-2, pp. 1–12. ISSN: 09215093. DOI: 10.1016/j.msea.2005.02.016.

119. Ezaz, Tawhid and Huseyin Sehitoglu (2011). “Type II detwinning in NiTi”. In: *Applied Physics Letters* 98.14, pp. 3–5. ISSN: 00036951. DOI: 10.1063/1.3574775.

120. Fultz, Brent and James Howe (2013). *Transmission Electron Microscopy and Diffractometry of Materials*. 4th ed. Springer. ISBN: 9783642297601.

121. Jeong, Jiwon et al. (2018). “In-situ TEM observation of {101¯2} twin-dominated deformation of Mg pillars: Twinning mechanism, size effects and rate dependency”. In: *Acta Materialia* 158, pp. 407–421. ISSN: 13596454. DOI: 10.1016/j.actamat.2018.07.027. URL: https://doi.org/10.1016/j.actamat.2018.07.027.

122. Herrmann, Helmut and Herbert Bucksch (2014). “Stress Distribution”. In: *Dictionary Geotechnical Engineering/Wörterbuch GeoTechnik*, pp. 1328–1328. DOI: 10.1007/978-3-642-41714-6_198078.

123. Eichler, Jens, Ulrich Eisele, and Jürgen Rödel (2004). “Mechanical properties of monoclinic zirconia”. In: *Journal of the American Ceramic Society* 87.7, pp. 1401–1403. ISSN: 00027820. DOI: 10.1111/j.1151-2916.2004.tb07748.x.

124. Moser, Benedikt et al. (2007). “Strength and fracture of Si micropillars: A new scanning electron microscopy-based micro-compression test”. In: *Journal of Materials Research* 22.4, pp. 1004–1011. ISSN: 08842914. DOI: 10.1557/jmr.2007.0140.

125. Zhu, T. T., A. J. Bushby, and D. J. Dunstan (2008). “Size effect in the initiation of plasticity for ceramics in nanoindentation”. In: *Journal of the Mechanics and Physics of Solids* 56.4, pp. 1170–1185. ISSN: 00225096. DOI: 10.1016/j.jmps.2007.10.003.

126. Tochigi, E. et al. (2014). “In situ TEM observations of plastic deformation in quartz crystals”. In: *Physics and Chemistry of Minerals* 41.10, pp. 757–765. ISSN: 14322021. DOI: 10.1007/s00269-014-0689-6.

127. Fukuda, Kazutaka et al. (2017). “Activation stress for slip systems of pure magnesium single crystals in pure shear test”. In: *Materials Transactions* 58.4, pp. 587–591. ISSN: 13459678. DOI: 10.2320/matertrans.M2016402.

128. Launey, M.E. et al. (2010). “Mechanistic Aspects of the fracture toughness of elk antler bone”. In: *Acta Biomaterialia* 6.1, pp. 1505–1514.

129. Aizenberg, Joanna et al. (2005). “Materials science: Skeleton of euplectella sp.: Structural hierarchy from the nanoscale to the macroscale”. In: *Science*. ISSN: 00368075. DOI: 10.1126/science.1112255.

130. Raabe, D., C. Sachs, and P. Romano (2005). "The crustacean exoskeleton as an example of a structurally and mechanically graded biological nanocomposite material". In: *Acta Materialia* 53.15, pp. 4281–4292. ISSN: 13596454. DOI: 10.1016/j.actamat.2005.05.027.

131. Gao, Huajian (2006). "Application of fracture mechanics concepts to hierarchical biomechanics of bone and bone-like materials". In: *International Journal of Fracture* 138.1-4, pp. 101–137. ISSN: 03769429. DOI: 10.1007/s10704-006-7156-4.

132. Launey, Maximilien E., Markus J. Buehler, and Robert O. Ritchie (2010). *On the Mechanistic Origins of Toughness in Bone*. Vol. 40. 1, pp. 25–53. ISBN: 0709091044. DOI: 10.1146/annurev-matsci-070909-104427.

133. Luo, Shi and Julia R. Greer (2018). "Bio-Mimicked Silica Architectures Capture Geometry, Microstructure, and Mechanical Properties of Marine Diatoms". In: *Advanced Engineering Materials* 20.9. ISSN: 15272648. DOI: 10.1002/adem.201800301.

134. Zhao, Hewei, Zhao Yang, and Lin Guo (2018). "Nacre-inspired composites with different macroscopic dimensions: Strategies for improved mechanical performance and applications". In: *NPG Asia Materials* 10.4, pp. 1–22. ISSN: 18844057. DOI: 10.1038/s41427-018-0009-6. URL: http://dx.doi.org/10.1038/s41427-018-0009-6.

135. Libonati, Flavia et al. (2019). "Bone-inspired enhanced fracture toughness of de novo fiber reinforced composites". In: *Scientific Reports*. ISSN: 20452322. DOI: 10.1038/s41598-019-39030-7.

136. Gupta, Neal S. (n.d.). *Chitin formation and diagenesis*. ISBN: 9789048196838.

137. Raabe, D. et al. (2006). "Microstructure and crystallographic texture of the chitin-protein network in the biological composite material of the exoskeleton of the lobster Homarus americanus". In: *Materials Science and Engineering A* 421.1-2, pp. 143–153. ISSN: 09215093. DOI: 10.1016/j.msea.2005.09.115.

138. Zhou, Fei et al. (2010). "Structure and mechanical properties of pincers of lobster (Procambarus clarkii) and crab (Eriocheir Sinensis)". In: *Journal of the Mechanical Behavior of Biomedical Materials* 3.6, pp. 454–463. ISSN: 18780180. DOI: 10.1016/j.jmbbm.2010.05.001.

139. Erko, Maxim et al. (2013). "Structural and mechanical properties of the arthropod cuticle: Comparison between the fang of the spider Cupiennius salei and the carapace of American lobster Homarus americanus". In: *Journal of Structural Biology* 183.2, pp. 172–179. ISSN: 10478477. DOI: 10.1016/j.jsb.2013.06.001. URL: http://dx.doi.org/10.1016/j.jsb.2013.06.001.

140. Fabritius, Helge Otto et al. (2009). “Influence of structural principles on the mechanics of a biological fiber-based composite material with hierarchical organization: The exoskeleton of the lobster homarus americanus”. In: *Advanced Materials* 21.4, pp. 391–400. ISSN: 09359648. DOI: 10.1002/adma.200801219.

141. Chen, Po Yu et al. (2008). “Structure and mechanical properties of crab exoskeletons”. In: *Acta Biomaterialia* 4.3, pp. 587–596. ISSN: 17427061. DOI: 10.1016/j.actbio.2007.12.010.

142. Politi, Yael et al. (2012). “A spider’s fang: How to design an injection needle using chitin-based composite material”. In: *Advanced Functional Materials* 22.12, pp. 2519–2528. ISSN: 1616301X. DOI: 10.1002/adfm.201200063.

143. Rajabi, H. et al. (2017). “Stiffness distribution in insect cuticle: A continuous or a discontinuous profile?” In: *Journal of the Royal Society Interface* 14.132. ISSN: 17425662. DOI: 10.1098/rsif.2017.0310.

144. Cribb, B. W. et al. (2010). “Hardness in arthropod exoskeletons in the absence of transition metals”. In: *Acta Biomaterialia* 6.8, pp. 3152–3156. ISSN: 17427061. DOI: 10.1016/j.actbio.2010.02.009. URL: http://dx.doi.org/10.1016/j.actbio.2010.02.009.

145. Vincent, Julian F.V. and Ulrike G.K. Wegst (2004). “Design and mechanical properties of insect cuticle”. In: *Arthropod Structure and Development* 33.3, pp. 187–199. ISSN: 14678039. DOI: 10.1016/j.asd.2004.05.006.

146. “On the Cuticle of the Scorpion Palamneus swammerdami” (1953). In: *Journal of Cell Science* s3-94.25, pp. 11–22. ISSN: 0021-9533.

147. Weaver, James C. et al. (2012). “The stomatopod dactyl club: A formidable damage-tolerant biological hammer”. In: *Science* 336.6086, pp. 1275–1280. ISSN: 10959203. DOI: 10.1126/science.1218764.

148. Sugawara, Ayae et al. (2006). “Self-organization of oriented calcium carbonate/polymer composites: Effects of a matrix peptide isolated from the exoskeleton of a crayfish”. In: *Angewandte Chemie - International Edition* 45.18, pp. 2876–2879. ISSN: 14337851. DOI: 10.1002/anie.200503800.

149. Zhao, Zi Long, Tao Shu, and Xi Qiao Feng (2016). “Study of biomechanical, anatomical, and physiological properties of scorpion stingers for developing biomimetic materials”. In: *Materials Science and Engineering C* 58, pp. 1112–1121. ISSN: 09284931. DOI: 10.1016/j.msec.2015.09.082.

150. Suksangpanya, Nobphadon et al. (2018). “Crack twisting and toughening strategies in Bouigand architectures”. In: *International Journal of Solids and Structures* 150, pp. 83–106. ISSN: 1359-0286. DOI: 10.1016/j.cossms.2010.07.001. URL: http://dx.doi.org/10.1016/j.cossms.2010.07.001.

151. Fischer, F. D. et al. (2017). "Crack driving force in twisted plywood structures". In: *Acta Biomaterialia* 55, pp. 349–359. ISSN: 18787568. DOI: 10.1016/j.actbio.2017.04.007.

152. Shang, J. S., Nigel H.H. Ngern, and Vincent B.C. Tan (2016). "Crustacean-inspired helicoidal laminates". In: *Composites Science and Technology* 128, pp. 222–232. ISSN: 02663538. DOI: 10.1016/j.compscitech.2016.04.007.

153. Cheng, Liang et al. (2011). "Mechanical behavior of bio-inspired laminated composites". In: *Composites Part A: Applied Science and Manufacturing* 42.2, pp. 211–220. ISSN: 1359835X. DOI: 10.1016/j.compositesa.2010.11.009.

154. Kellersztein, Israel et al. (2019). "The exoskeleton of scorpions' pincers: Structure and micro-mechanical properties". In: *Acta Biomaterialia* 94, pp. 565–573. ISSN: 18787568. DOI: 10.1016/j.actbio.2019.06.036.

155. Greenfeld, Israel, Israel Kellersztein, and H. Daniel Wagner (2020). "Nested helicoids in biological microstructures". In: *Nature Communications* 11.1, pp. 1–12. ISSN: 20411723. DOI: 10.1038/s41467-019-13978-6. URL: http://dx.doi.org/10.1038/s41467-019-13978-6.

156. Melnick, C. A., Z. Chen, and J. J. Mecholsky (1996). "Hardness and toughness of exoskeleton material in the stone crab, Menippe mercenaria". In: *Journal of Materials Research* 11.11, pp. 2903–2907. ISSN: 08842914. DOI: 10.1557/JMR.1996.0367.

157. Arias, José L. and María S. Fernández (2008). "Polysaccharides and proteoglycans in calcium carbonate-based Biomineralization". In: *Chemical Reviews* 108.11, pp. 4475–4482. ISSN: 00092665. DOI: 10.1021/cr078269p.

158. Bentov, Shmuel et al. (2016). "Calcium phosphate mineralization is widely applied in crustacean mandibles". In: *Scientific Reports* 6.September 2015, pp. 1–10. ISSN: 20452322. DOI: 10.1038/srep22118. URL: http://dx.doi.org/10.1038/srep22118.

159. Arakaki, Atsushi et al. (2015). "Biomineralization-inspired synthesis of functional organic/inorganic hybrid materials: Organic molecular control of self-organization of hybrids". In: *Organic and Biomolecular Chemistry* 13.4, pp. 974–989. ISSN: 14770520. DOI: 10.1039/c4ob01796j.

160. Rodriguez-Blanco, Juan Diego, Samuel Shaw, and Liane G. Benning (2011). "The kinetics and mechanisms of amorphous calcium carbonate (ACC) crystallization to calcite, via vaterite." In: *Nanoscale* 3.1, pp. 265–271. ISSN: 20403364. DOI: 10.1039/c0nr00589d.

161. Degtyar, Elena et al. (2014). “The Mechanical Role of Metal Ions in Biogenic Protein-Based Materials”. In: *Angewandte Chemie - International Edition* 53.45, pp. 12026–12044. ISSN: 15213773. DOI: 10.1002/anie.201404272.

162. ASTM Standard E1820 (2013). “Standard Test Method for Measurement of Fracture Toughness”. In: *ASTM Book of Standards*. DOI: 10.1520/E1820-13.Copyright.

163. Koehl, B Y M A R (1977). “Effects of Sea Anemones on the Flow Forces They Encounter”. In: *Journal of Experimental Biology* 69.1, pp. 87–105. ISSN: 0022-0949.

164. Coyle, Stephen et al. (2018). “Bio-inspired soft robotics: Material selection, actuation, and design”. In: *Extreme Mechanics Letters* 22, pp. 51–59.

165. Wilson, Samantha L. et al. (2014). “Mechanical characterization of hydrogels and its implications for cellular activities”. In: *RSC Soft Matter* 2, pp. 171–190. DOI: 10.1039/9781782622055-00171.

166. Maggi, Alessandro, Hanqing Li, and Julia R. Greer (2017). “Three-dimensional nano-architected scaffolds with tunable stiffness for efficient bone tissue growth”. In: *Acta Biomaterialia*. ISSN: 18787568. DOI: 10.1016/j.actbio.2017.09.007.

167. Abrams, Michael J. et al. (2015). “Self-repairing symmetry in jellyfish through mechanically driven reorganization”. In: *Proceedings of the National Academy of Sciences of the United States of America* 112.26, E3365–E3373. ISSN: 10916490. DOI: 10.1073/pnas.1502497112.

168. Bai, Ruobing, Jiawei Yang, and Zhigang Suo (2019). “Fatigue of hydrogels”. In: *European Journal of Mechanics, A/Solids* 74.December 2018, pp. 337–370. ISSN: 09977538. DOI: 10.1016/j.euromechsol.2018.12.001. URL: https://doi.org/10.1016/j.euromechsol.2018.12.001.

169. Chen, Chao, Zhengjin Wang, and Zhigang Suo (2017). “Flaw sensitivity of highly stretchable materials”. In: *Extreme Mechanics Letters* 10, pp. 50–57. ISSN: 23524316. DOI: 10.1016/j.eml.2016.10.002. URL: http://dx.doi.org/10.1016/j.eml.2016.10.002.

170. Sun, Jeong-Yun et al. (2012). “Highly stretchable and tough hydrogels”. In: *Nature* 489.1, pp. 133–136. ISSN: 15378276. DOI: 10.1038/jid.2014.371. arXiv: NIHMS150003. URL: https://www.ncbi.nlm.nih.gov/pmc/articles/PMC3624763/pdf/nihms412728.pdf.

171. Buyanov, A. L. et al. (2010). “Anisotropic swelling and mechanical behavior of composite bacterial cellulose-poly(acrylamide or acrylamide-sodium acrylate) hydrogels”. In: *Journal of the Mechanical Behavior of Biomedical Materials* 3.1, pp. 102–111. ISSN: 17516161. DOI: 10.1016/j.jmbbm.2009.06.001. URL: http://dx.doi.org/10.1016/j.jmbbm.2009.06.001.

172. Nardo, L De and S Fare (2017). "Dynamico-mechanical characterization of polymer biomaterials". In: *Characterization of Polymeric Biomaterials*.

173. Zhu, Jintang et al. (2012). "Mechanical properties, anisotropic swelling behaviours and structures of jellyfish mesogloea". In: *Journal of the Mechanical Behavior of Biomedical Materials* 6, pp. 63–73. ISSN: 17516161. DOI: 10.1016/j.jmbbm.2011.10.005. URL: http://dx.doi.org/10.1016/j.jmbbm.2011.10.005.

174. Megill, William M., John M. Gosline, and Robert W. Blake (2005). "The modulus of elasticity of fibrillin-containing elastic fibres in the mesoglea of the hydromedusa Polyorchis penicillatus". In: *Journal of Experimental Biology* 208.20, pp. 3819–3834. ISSN: 00220949. DOI: 10.1242/jeb.01765.

175. Gambini, Camille et al. (2012). "Micro- and macrorheology of jellyfish extracellular matrix". In: *Biophysical Journal* 102.1, pp. 1–9. ISSN: 00063495. DOI: 10.1016/j.bpj.2011.11.4004.

176. Mallett, Kaitlyn F. and Ellen M. Arruda (2017). "Digital image correlation-aided mechanical characterization of the anteromedial and posterolateral bundles of the anterior cruciate ligament". In: *Acta Biomaterialia*. ISSN: 18787568. DOI: 10.1016/j.actbio.2017.03.045.

177. Alexander, B Y R M C N (1964). "Visco-Elastic Properties of the Mesogloea of Jellyfish". In: *Journal of Experimental Biology* 41.2, pp. 363–369. ISSN: 0022-0949.

178. Herbert, Erik G. et al. (2009). "Measuring the constitutive behavior of viscoelastic solids in the time and frequency domain using flat punch nanoindentation". In: *Journal of Materials Research* 24.3, pp. 626–637. ISSN: 08842914. DOI: 10.1557/jmr.2009.0089.

179. Wright, Wendelin J. and W. D. Nix (2009). "Storage and loss stiffnesses and moduli as determined by dynamic nanoindentation". In: *Journal of Materials Research*. ISSN: 08842914. DOI: 10.1557/jmr.2009.0112.

180. Hu, Yuhang et al. (2010). "Using indentation to characterize the poroelasticity of gels". In: *Applied Physics Letters* 96.12. ISSN: 00036951. DOI: 10.1063/1.3370354.

181. Kalcioglu, Z. Ilke et al. (2012). "From macro- to microscale poroelastic characterization of polymeric hydrogels via indentation". In: *Soft Matter* 8.12, pp. 3393–3398. ISSN: 1744683X. DOI: 10.1039/c2sm06825g.

182. Costello, John et al. (2021). "The Hydrodynamics of Jellyfish Swimming". In: *Annual Review of Marine Science*. ISSN: 1941-0611. DOI: 10.1146/annurev-marine-031120-091442.

183. Roberts, Justine J. et al. (2011). “Comparative study of the viscoelastic mechanical behavior of agarose and poly(ethylene glycol) hydrogels”. In: *Journal of Biomedical Materials Research - Part B Applied Biomaterials* 99 B.1, pp. 158–169. ISSN: 15524973. DOI: 10.1002/jbm.b.31883.

184. Bower, Allan F. (2009). *Applied mechanics of solids*. ISBN: 9781439802489. DOI: 10.1201/9781439802489.

185. Pryse, Kenneth M. et al. (2003). “Incremental mechanics of collagen gels: New experiments and a new viscoelastic model”. In: *Annals of Biomedical Engineering* 31.10, pp. 1287–1296. ISSN: 00906964. DOI: 10.1114/1.1615571.

186. Low-Frequency Range, I. and M. A. Biot (1956). “Theory of Propagation of Elastic Waves in a Fluid-Saturated Porous Solid”. In: *Journal of the Acoustical Society of America*. ISSN: NA. DOI: 10.1121/1.1908239.

187. Weizel, A. et al. (2020). “Complex mechanical behavior of human articular cartilage and hydrogels for cartilage repair”. In: *Acta Biomaterialia* xxxx. ISSN: 18787568. DOI: 10.1016/j.actbio.2020.10.025. URL: https://doi.org/10.1016/j.actbio.2020.10.025.

188. Hu, Yuhang and Zhigang Suo (2012). “Viscoelasticity and Poroelasticity in”. In: *Acta Mechanica Solida Sinica* 25.5, pp. 441–458. ISSN: 0894-9166. URL: http://dx.doi.org/10.1016/S0894-9166(12)60039-1.

189. Coussy, Olivier (2005). “Poroviscoelasticity”. In: *Poromechanics*. DOI: 10.1002/0470092718.ch9.

190. McGarry, M. D.J. et al. (2015). “Suitability of poroelastic and viscoelastic mechanical models for high and low frequency MR elastography”. In: *Medical Physics* 42.2, pp. 947–957. ISSN: 00942405. DOI: 10.1118/1.4905048. URL: http://dx.doi.org/10.1118/1.4905048.

191. Wang, Qi Ming et al. (2014). “Separating viscoelasticity and poroelasticity of gels with different length and time scales”. In: *Acta Mechanica Sinica/Lixue Xuebao* 30.1, pp. 20–27. ISSN: 05677718. DOI: 10.1007/s10409-014-0015-z.

192. Shen, Zhilei Liu et al. (2011). “Viscoelastic Properties of Isolated Collagen Fibrils”. In: *Biophysical Journal* 100.12, pp. 3008–3015. ISSN: 0006-3495. DOI: 10.1016/j.bpj.2011.04.052. URL: http://dx.doi.org/10.1016/j.bpj.2011.04.052.

193. Sasaki, Naoki and Shingo Odajima (1996). “Elongation mechanism of collagen fibrils and force-strain relations of tendon at each level of structural hierarchy”. In: *Journal of Biomechanics* 29.9, pp. 1131–1136. ISSN: 00219290. DOI: 10.1016/0021-9290(96)00024-3.

194. Gautieri, Alfonso et al. (2011). “Hierarchical structure and nanomechanics of collagen microfibrils from the atomistic scale up”. In: *Nano Letters* 11.2, pp. 757–766. ISSN: 15306984. DOI: 10.1021/nl103943u.

195. Yang, Lanti (2008). “MECHANICAL PROPERTIES OF COLLAGEN FIBRILS AND ELASTIC FIBERS EXPLORED BY AFM”. PhD thesis. ISBN: 9789036526234.

196. Aifantis, Katerina E., Sanjiv Shrivastava, and Gregory M. Odegard (2011). “Transverse mechanical properties of collagen fibers from nanoindentation”. In: *Journal of Materials Science: Materials in Medicine* 22, pp. 1375–1381. DOI: 10.1007/s10856-011-4320-9.

Appendix A

STUDY OF MICROCRACK GOVERNED FAILURE IN GLASS VIA FINITE ELEMENT MODELING (FEM) AND NANOINDNETATION

Amgen Autoinjector glass syringes are most prone to fracture at the tip during its impact with the front end of the outer plastic casing. It was hypothesized that this fracture mechanism is a combination of (a) the tip area including micro-defects or flaws that lower the failure stress and (b) the impact generating a high stress concentration near the fracture site.

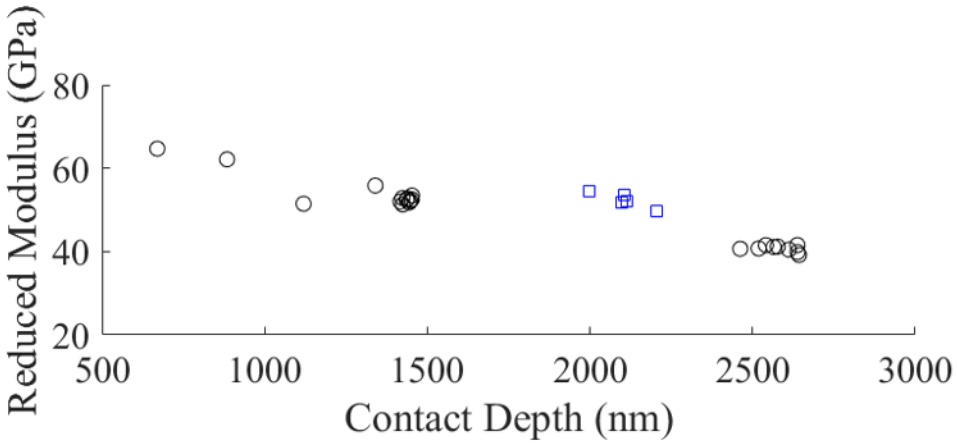

Figure A.1: Modulus showing similar trends for indents on the wall and tip of the syringe.

To first understand the material properties as well as the size and distributions of flaws, we carried out nano-indentation experiments at the tip and at areas on the outer wall of the syringe for comparison; it was found that the material stiffness is consistent among all the tested sites (see Fig. A.1). The indentation load-depth data as well as post-indentation imaging, both shown in Fig. A.2, revealed no visible sign of pre-existing flaws, which usually create large load plateaus in the mechanical data and generate visible cracks around the indentation marks.

Despite the lack of catastrophic failure / crack events during indentation, microcrack events are visible during the deforming process of indentation both on the wall and the tip of the syringes. We identify fast popin events as micrack propagation similar

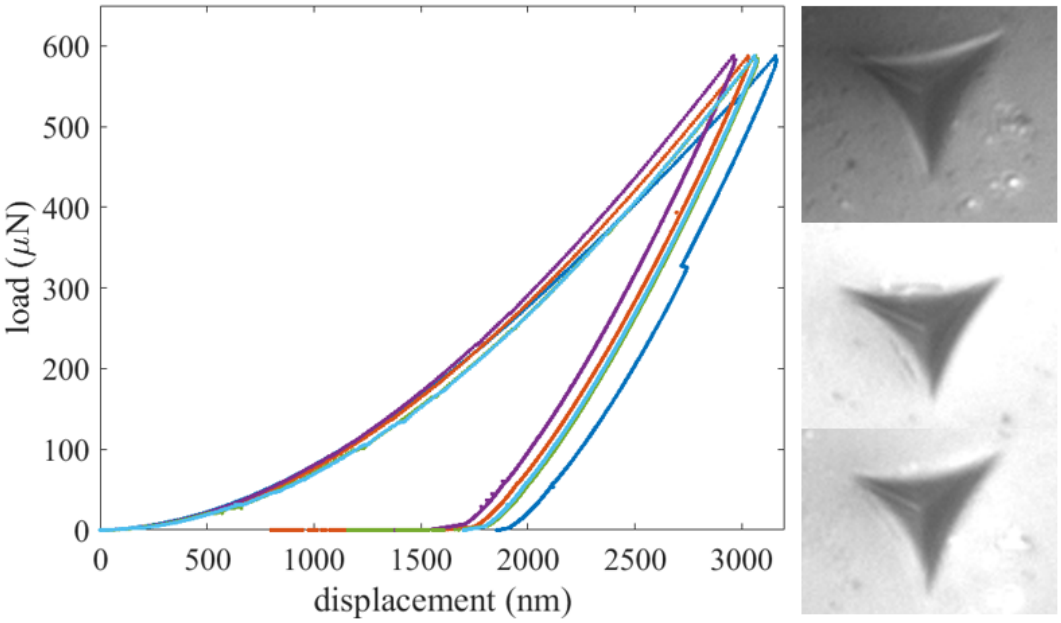

Figure A.2: Corresponding indentation data and plastic deformation.

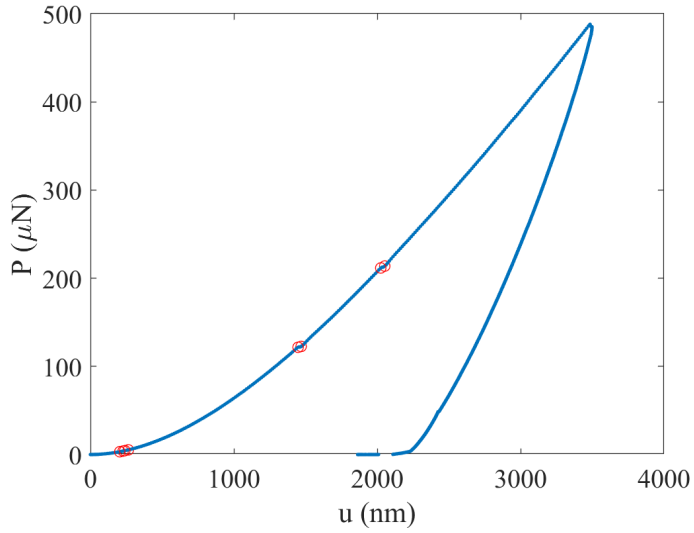

Figure A.3: Example of popin measurements during an indentation test.

to in [1] and Fig. A.3 demonstrates the popins identified for an example indentation test using this method. The PDF (probability distribution function) of size for the popins are shown in Fig. **??**, which show clear distinction between the wall and tip, suggesting that the two regions, despite having similar elastic properties, are prone to different failure probabilities.

In addition, we ran several dynamic Abaqus FEM simulations to find out the stress

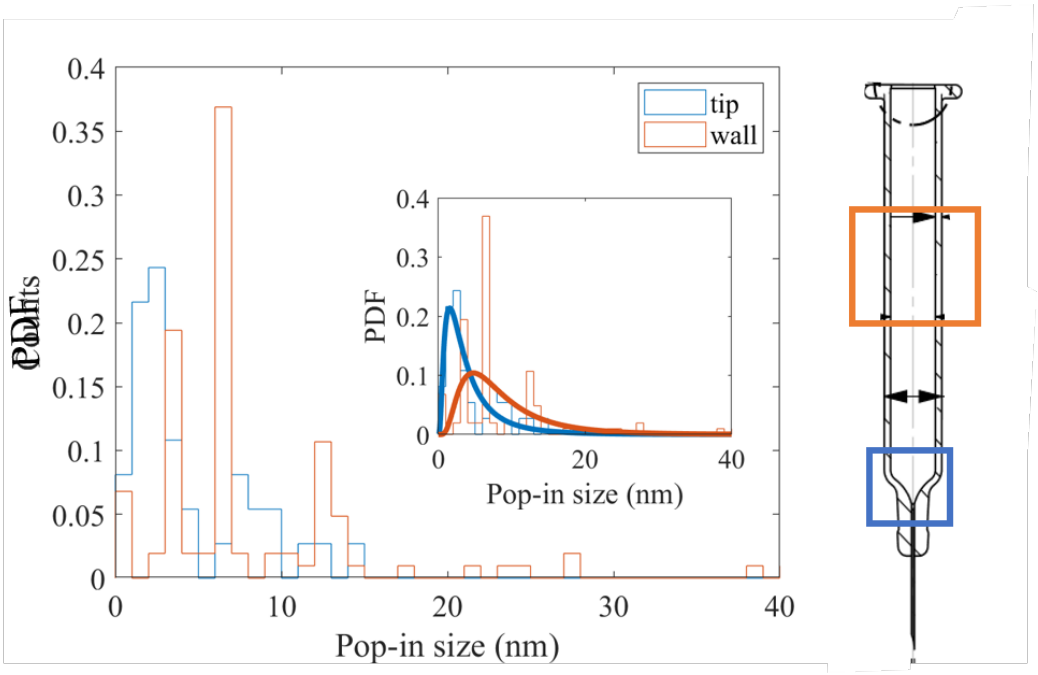

Figure A.4: Different PDF for microcrack events at the wall and at the tip of the syringe.

distribution in the syringe wall before and after the impact, and found a stress concentration of 28MPa at the impact site at the end of the tip (shown in Fig. A.5) at 375μs after the impact, which is higher than the tensile failure strength of glass (7MPa) [2] and enough to generate local cracks.

References

1. Ni, Xiaoyue et al. (2019). "Yield Precursor Dislocation Avalanches in Small Crystals: The Irreversibility Transition". In: *Physical Review Letters* 123.3, pp. 1–11. ISSN: 10797114. DOI: 10.1103/PhysRevLett.123.035501.

2. Kasunic, Keith J. (2015). *Optomechanical Systems Engineering*. ISBN: 9781118809860. DOI: 10.1002/9781118809860.

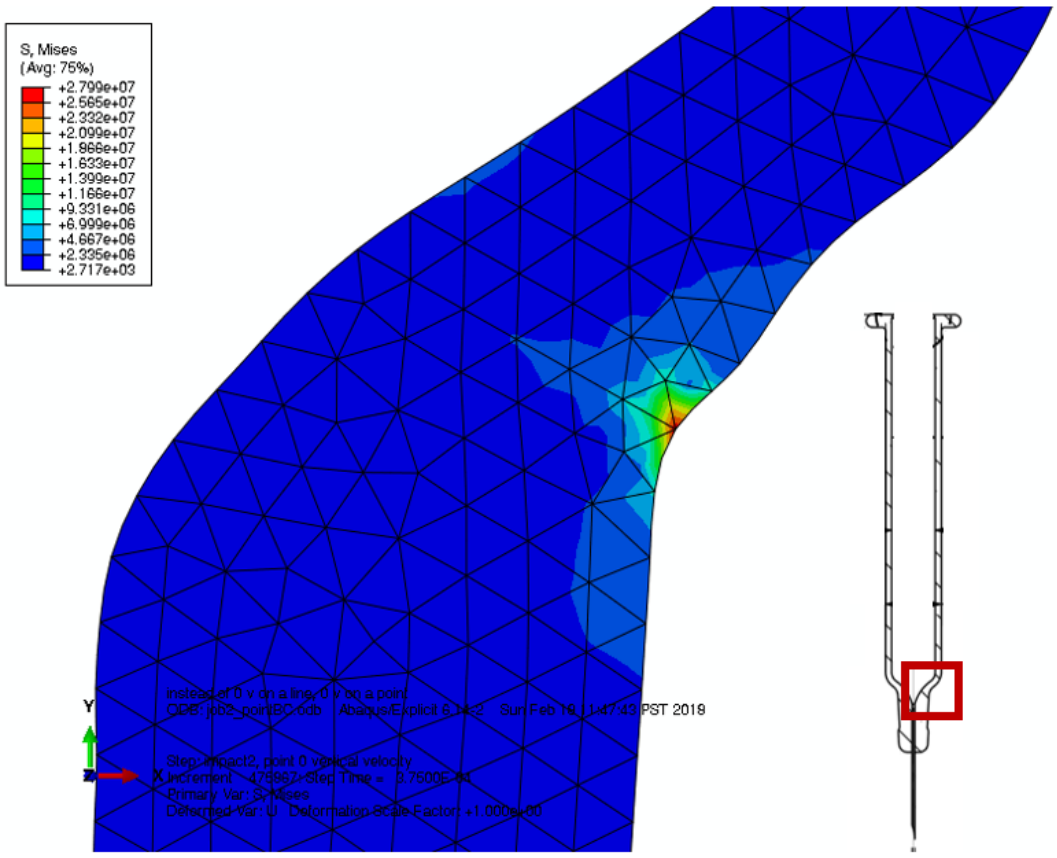

Figure A.5: Stress concentration upon impact at the tip near crack site.

Appendix B

2D TO 3D RECONSTRUCTION

Here we describe the process of 2D image to 3D shape reconstruction and attach the corresponding Matlab code.

Figure B.1: Defining a reference point based on 2D images of the same particle.

As is described in Chapter 2, the 3D coordinate of a point on a particle is uniquely calculated using the 2D coordinates of that point in two images taken of the particle from different angles (Fig. 2.24). For each particle, a reference point was first determined by assigning $(0, 0, 0)$ coordinate to a point, as is demonstrated in Fig. B.1. The direction of the projected viewing line is then uniquely determined as the direction perpendicular to the image planes. For each point in 3D, two projection lines can be determined by taking that viewing line through the point's location on the two images, and its 3D coordinate is simmply the crosspoint of those thwo lines (Fig. B.2). Due to experimental errors, the two projection lines may not perfectly cross, in which case the final coordinate of that point is taken as the midpoint of the shortest line between the two projection lines, which is mathematically unique.

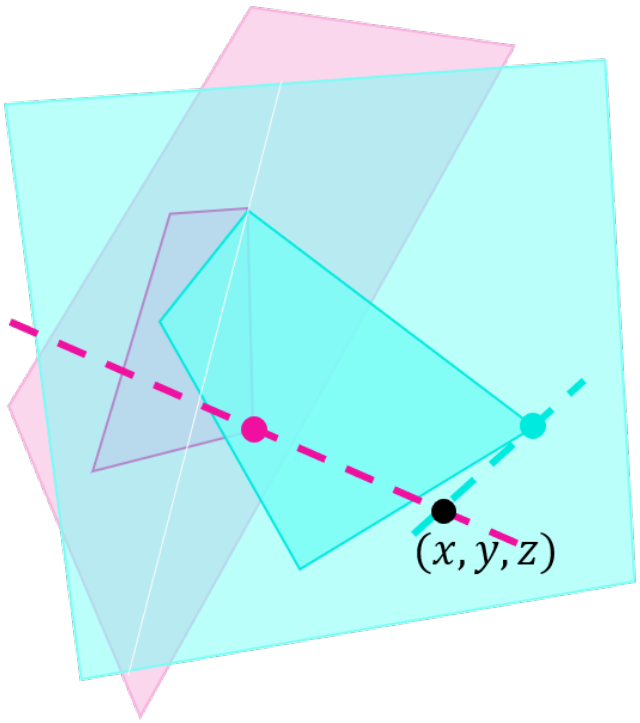

Figure B.2: Calculating the 3D coordinate of a point as the crosspoint of two projection lines.

```
%% takes images of 2 views and output the ginput point
    pairs as points in 3d space
LS0 = [0;sin(deg2rad(52));-cos(deg2rad(52))]; % line
    sense of view
% LS90 = [-sin(deg2rad(52));0;-cos(deg2rad(52))];
% LS180 = [0;-sin(deg2rad(52));-cos(deg2rad(52))];
% LS270 = [sin(deg2rad(52));0;-cos(deg2rad(52))];

%% image names
particle = 'R1_postPI85';
imgnames = {[particle '.tif'],[particle '_90deg.tif'],[
    particle '_180deg.tif'],[particle '_270deg.tif']};
vRs = [0,90,180,270];

%% input 2 views
v1 = 4;
v2 = 1;
```

```
15 v1_imgname = imgnames{v1};
16 v1R = vRs(v1); % rotation degree from original view in
       deg
17 LS1 = LS0;
18 %LS1 = [0;sin(deg2rad(56));-cos(deg2rad(56))];
19 v2_imgname = imgnames{v2};
20 v2R = vRs(v2);
21 LS2 = LS0;
22 %LS2 = [0;sin(deg2rad(56));-cos(deg2rad(56))];
23 figure(1);
24 image1 = imread(v1_imgname);
25 imshow(image1);
26 set(gcf,'Position',[100 200 900 600]);
27 figure(2);
28 image2 = imread(v2_imgname);
29 imshow(image2);
30 set(gcf,'Position',[1050 200 900 600]);
31 v1R = deg2rad(v1R);
32 R1 = [cos(v1R),-sin(v1R),0;sin(v1R),cos(v1R),0;0,0,1];
33 v2R = deg2rad(v2R);
34 R2 = [cos(v2R),-sin(v2R),0;sin(v2R),cos(v2R),0;0,0,1];
35
36 % set scale for both
37 figure(1);
38 fprintf('Select end points of scale bar\n');
39 [x,~] = ginput(2);
40 scale1 = input('Physical length of scale bar (nm): ')/(
       x(2)-x(1));
41 figure(2);
42 fprintf('Select end points of scale bar\n');
43 [x,~] = ginput(2);
44 scale2 = input('Physical length of scale bar (nm): ')/(
       x(2)-x(1));
45 % ginput till quit pair of dots -> average of nearest
       points between two projection
46 % lines
```

```
47 flag = true;
48 count = 1;
49 fprintf(['pick 1st points.'])
50 if count == 1
51     fprintf('This will be the reference point');
52 end
53 fprintf('\n');
54 figure(1);
55 [x1,y1] = ginput(1);
56 text(x1,y1,num2str(count),'Color',[1,1,1]);
57 x2d1 = [x1;y1];
58 figure(2);
59 [x2,y2] = ginput(1);
60 text(x2,y2,num2str(count),'Color',[1,1,1]);
61 x2d2 = [x2;y2];
62 x3d = [0;0;0];
63 A = R1*LS1;
64 B = R2*LS2;
65 while flag
66     count = count+1;
67     fprintf(['pick ' num2str(count) 'th points.'])
68     fprintf('\n');
69     figure(1);
70     [x1,y1] = ginput(1);
71     text(x1,y1,num2str(count),'Color',[1,1,1]);
72     x2d1(:,count) = [x1;y1];
73     figure(2);
74     [x2,y2] = ginput(1);
75     text(x2,y2,num2str(count),'Color',[1,1,1]);
76     x2d2(:,count) = [x2;y2];
77     % process
78     x1 = x1-x2d1(1,1);
79     y1 = x2d1(2,1)-y1; % zero
80     a = R1*[x1;y1*cos(deg2rad(52));y1*sin(deg2rad(52))
           ].*scale1;
81     x2 = x2-x2d2(1,1);
```

```
82      y2 = x2d2(2,1)-y2; % zero
83      b = R2*[x2;y2*cos(deg2rad(52));y2*sin(deg2rad(52))
            ].*scale2;
84      x3d(:,count) = crosspoint_nearest(A,a,B,b);
85      flag = input('want more? (N=0): ');
86  end
87  figure(1);
88  saveas(gca,[v1_imgname(1:end-4) '(w' v2_imgname(1:end
        -4) ')_idx.fig']);
89  saveas(gca,[v1_imgname(1:end-4) '(w' v2_imgname(1:end
        -4) ')_idx.png']);
90  figure(2);
91  saveas(gca,[v2_imgname(1:end-4) '(w' v1_imgname(1:end
        -4) ')_idx.fig']);
92  saveas(gca,[v2_imgname(1:end-4) '(w' v1_imgname(1:end
        -4) ')_idx.png']);
93  dlmwrite([v1_imgname(1:end-4) '+' v2_imgname(1:end-4) '
        _x.txt'],x3d');
94
95  %%
96  figure(3)
97  plot3(x3d(1,:),x3d(2,:),x3d(3,:),'o');
98
99  %%
100 figure(4)
101 patch(x3d(1,:),x3d(2,:),x3d(3,:),[0.5,0.5,0.5]);
```